A Polydispersed Gaussian-Moment Model for Polythermal, Evaporating, and Turbulent Multiphase Flow Applications

by

Benoit Allard

Thesis submitted to the University of Ottawa
in partial fulfillment of the requirements for the degree of
Master of Applied Science
in
Mechanical Engineering

Abstract

A novel higher-order moment-closure method is applied for the Eulerian treatment of gas-particle multiphase flows characterized by a dilute polydisperse and polythermal particle phase. Based upon the polydisperse Gaussian-moment model (PGM) framework, the proposed model is derived by applying an entropy-maximization moment-closure formulation to the transport equation of the particle-number density function, which is equivalent to the Williams-Boltzmann equation for droplet sprays. The resulting set of first-order robustly-hyperbolic balance laws include a direct treatment for local higher-order statistics such as co-variances between particle distinguishable properties (i.e., diameter and temperature) and particle velocity. Leveraging the additional distinguishing variables, classical hydrodynamic droplet evaporation theory is considered to describe unsteady droplet vaporization. Further, studying turbulent multiphase flow theory, a first-order hyperbolicity maintaining approximation to turbulent flow diffusion-inertia effects is proposed. Investigations into the predictive capabilities of the model are evaluated relative to Lagrangian-based solutions for a range of flows, including aerosol dispersion and fuel-sprays. Further, the model is implemented in a massively parallel discontinuous-Galerkin framework. Validation of the proposed turbulence coupling model is subsequently performed against experimental data, and a qualitative analysis of the model is given for a qualitative liquid fuel-spray problem.

Acknowledgements

First, a great many thanks are due to my thesis advisor, Professor James McDonald, for his continued support and guidance throughout the numerous trials and tribulations encountered in completing my Masters thesis. His knowledge and optimism provided both invaluable insight and great inspiration in tackling the many challenges covered as part of this work – for which I am very thankful.

A great deal of appreciation is also directed to Dr. Lucian Ivan from the Canadian Nuclear Laboratories who provided much support and many resources in completing my thesis. Very honorable mentions are also due for both Mathieu Marchildon and Francois Forgues who both shared their relevant knowledge and lessons learned.

I would also much like to extend my gratitude to the Canadian Nuclear Laboratories for providing funding which supported this research during my Masters degree. This recognition also extends to the Ontario Graduate Scholarship (OGS) program which also provided indispensible financial support during the completion of this research.

Lastly, a big thank you to the Digital Research Alliance of Canada (the Alliance) and Argonne Leadership Computing Facility (ALCF) for providing the computational resources leveraged to complete my research.

Table of Contents

List of Tables

List of Figures

Chapter 1

Introduction

1.1 Motivation

Gas-particle multiphase flows appear in myriad industrial, energy conversion, environmental and medical processes. The study of these particle flows has been widely summarized in various monographs [4, 11, 14, 55, 87, 92, 110, 125]. Despite their prevalence in countless applications, these ubiquitous flows remain a computational challenge as the complexity of the physical and thermodynamic processes increases to model phenomena such as polydispersity, evaporation, coalescence, and atomization. Namely, while the thermodynamic and kinetic description of gas-particle flows has been widely studied, few models have been suitable for efficient implementation in large-scale computational frameworks.

Lagrangian models, for instance, remain unable to model particles over the entire domain, as predicting their evolution can become prohibitively expensive and computationally infeasible at large scales. Eulerian models are conversely less taxing, though significant errors arise from mathematical artifacts when treating even monodispersed multiphase flows with traditional models. Most of these models only treat a small number of variables describing the particle phase—typically the density and velocity [86, 94]. As most of these classical models assume that all particles at a location in space share the same velocity, they are inappropriate for situations when a range of particle velocities is expected. The inabilities of these traditional methods motivate the proposal of higher-order moment-closure methods inspired by the kinetic theory of gases [19, 29, 30, 62, 109]. These methods provide

an expanded set of partial differential equations (PDEs) to accurately describe the evolution of particles and gain their attractiveness from their computational Eulerian nature. Likewise, these model allow for the direct treatment of higher-order statistics of particle velocities, such as variances and co-variances.

1.2 Objectives of the Current Work

The well-known ten-moment maximum-entropy closure from the kinetic theory of gases has traditionally provided a first-order hyperbolic set of equations for the treatment of adiabatic viscous compressible gases, and has generally been shown to successfully recover a wide range of equilibrium and non-equilibrium gas flows [7, 9, 10, 57, 66, 69, 101]. However, recent works by Forgues *et al.* [26] have led to a general extension of the ten-moment maximum-entropy model for applications beyond traditional rarefied gas dynamics—providing instead a description for dilute gas-particle multiphase flows [56, 57]. Specifically, the proposed formulation allows for the treatment of an arbitrary number of distinguishable particle properties, such as size or temperature, to differentiate particles of a dilute particle-phase. Furthermore, this formulation provides a direct treatment for local variances and covariances between all particle properties and velocities. This statistical information is not commonly available or utilized in traditional Eulerian methods and holds the promise of improved modelling accuracy at reduced computational cost. Forgues *et al.* have demonstrated the general polydispersed Gaussian-moment model (PGM) formulation for only one distinguishable variable representing the particle size. For this single-scalar case, the proposed model yielded a set of first-order robustly-hyperbolic balance laws which was shown to maintain a physically realizable distribution function for all admissible initial conditions. Importantly however, the model was formulated and studied for the case of laminar particle sedimentation problems. While useful for a limited range of natural and bio-aerosol spray problems, the originally proposed model is incapable of capturing complex physical and thermodynamic processes encountered within gas turbines, rocket engines, and industrial furnaces for instance.

The current work aims to propose a new two-scalar PGM model to account for particles of not only varying size, but also for a range of evolving temperatures. Specifically, an additional distinguishable variable is introduced to describe a polydisperse and polythermal particle phase. For such a case, the underlying kinetic equation governing the evolution of the particle distribution function is equivalent to the Williams-Boltzmann equation [117], commonly used in spray applications. Furthermore, using classical monocomponent droplet evaporation theory, temperature dependant gas-particle heat and mass transfer is considered using appropriate and integrable approximations to the equations for particle size and temperature rates of change. Lastly, turbulent gas-particle theory is studied and a first-order hyperbolicity maintaining approximation to one-way isotropic turbulence coupling, between the background flow and particle phase, is proposed.

The proposed two-scalar PGM for the description of polydisperse and polythermal multiphase flows promises to allow pervasive implementation in engineering application providing improved prediction for practical stochastic spray problems while equally providing improved large-scale computational performance. These modelling efforts have the potential to aide in the engineering and development of lower pollutant emitting combustion engines, agricultural chemical nozzles, and medical inhalers, among many more possible applications.

1.3 Scope of the Current Study

This thesis covers the formulation and implementation of the two-scalar PGM for evaporating and turbulent gas-particle multiphase flows. First, a brief introduction to gas-particle multiphase flows and modelling approaches is provided in Chapter 2. In Chapter 3, a review of the kinetic theory of gases is presented, as well as the concept of moment closures. Next, in Chapter 4, the generalized PGM framework is introduced which provides the foundation for the proposed surface-weighted two-scalar formulation for evaporating sprays of Chapter 5. Likewise, the strict hyperbolicity of the model is discussed, and an Eigenvalue analysis is presented. Thereafter, Chapter 6 presents the various gas-droplet coupling models included within the proposed model — which includes a reviews turbu-

lent particle dispersion and classical droplet evaporation theory. Chapter 7 describes the numerical methods utilized for the numerical analyses conducted as part of Chapter 8. Therein, comparison and analysis of the numerical predictions obtained using the model are presented for a variety of cases, including bio-aerosol dispersion and liquid fuel sprays. Finally, Chapter 9 discusses next steps and future work required for the continued development of the proposed novel approach to gas-particle multiphase flow modelling.

Chapter 2

Gas-Particle Multiphase Flows

The current situation of gas-particle multiphase flows is described by a continuously connected carrier phase in which relatively small immiscible particles are suspended. These types of multiphase flows are encountered in numerous industrial, energy conversion, environmental and medical processes, e.g., medical inhalers, fluidization in nozzles, crop dusting, additive manufacturing, particle separators, etc. [11, 14, 55, 87, 92, 125]. Each example provided exhibits its own particular complex behavior which also brings forward its particular modelling difficulties. Traditionally, these gas-particle flows are characterized by their granularity, i.e., the mass fraction of the particle phase. However, in the present work, particle phases are proposed to also be characterized by observable or measurable distinguishing properties, e.g., size, temperature, shape, colour, etc.

Analogous to traditional flow regime definitions, the granularity of the particle phase greatly influences the modelling approaches to gas-particle multiphase flows. The specific importance of the granularity can be characterized by the non-dimensional quantity known as the Knudsen number. Specifically, the Knudsen number quantifies the relative importance of individual particle interactions against the macroscopic scale of the flow. The Knudsen number is defined as

$$Kn = \frac{\lambda}{\ell}\,, \tag{2.1}$$

and describes the ratio between the mean free path, λ, and the representative integral length scale of the macroscopic flow. In traditional kinetic theory, the mean free path is

simply the average distance traveled during the mean time of free flight, τ, between particle collisions. The Knudsen number therefore provides a relevant dimensionless measure of the applicability of continuum assumptions. In situations where Kn is small, the frequency of particle collisions effectively distributes disturbances between particles such that particles behave as a continuum rather than individual point-like particles. Conversly, when Kn is large, particle collisions contribute little to the macroscopic behaviour, and the problem is instead dominated by boundary interactions, or interactions with the carrier phase. Typically, flow regimes are bounded by ranges of the Knudsen number [99],

- $Kn \lesssim 0.01$: Known as the hydrodynamic regime, this flow regime is treated using a traditional Eulerian-field based continuum mechanics formulation of fluid dynamics.
- $0.01 \lesssim Kn \lesssim 0.1$: Referred to as the slip flow regime. Here, traditional Eulerian-field models based on continuum assumptions remain valid. However, additional boundary conditions to describe velocity slip and temperature discontinuities at gas-particle interfaces are required.
- $0.1 \lesssim Kn \lesssim 10$: The transition, or rarefied, regime, where traditional Eulerian-field models lose their validity despite the near-continuum behaviour of the flow.
- $Kn \gtrsim 10$: Delinates the collisionless flow regime. Here, particle collisions become negligible, favouring a statistical formulation of fluid dynamics.

Within the present work, particle phases are assumed to be dilute and therefore described by a Knudsen number within the collisionless flow regime. Outside of the hydrodynamic regime, particle phases exhibit important non-equilibrium effects expected from related rarefied gas dynamics within this particular regime. Consequently, these effects motivate the exploration of alternative continuum equations to describe the particle phase – as both traditional Lagrangian-particle and Eulerian-field based methods present considerable numerical and modelling challenges. These approaches, along with novel alternatives, are discussed and criticized within the following short sections.

2.1 Lagrangian-Particle Methods

The Lagrangian-particle tracking (LPT) approach to gas-particle multiphase flows seeks to treat the particle phase on a individual particle basis. Here, particle trajectories are traced according to a spacetime-coupled set of ordinary differential equations (ODEs) for the evolution of a discrete particle. Traditionally, this set of equations provides a description for the motion of a discrete particle deduced from Newton's second law of motion [122], however, such as in the case of fuel-spray modelling, this set of ODEs can be expanded to describe the time-evolution of an arbitrary number of additional particle properties, e.g., size and temperature. Generally, this set of ODEs takes the following form,

$$\frac{\mathrm{d}\, x_i}{\mathrm{d}\, t} = v_i \,, \tag{2.2}$$

$$\frac{\mathrm{d}\, v_i}{\mathrm{d}\, t} = \sum a_\alpha \,, \tag{2.3}$$

$$\frac{\mathrm{d}\, \zeta_{\breve{i}}}{\mathrm{d}\, t} = \sum \Upsilon_{\breve{i}} \,. \tag{2.4}$$

Of course, the first two equations are simply related to Newton's second law of motion for a discrete particle subjected to acceleration fields, a_α, while Equation (2.4) describes the time-evolution of an arbitrary particle distinguishing variable, $\zeta_{\breve{i}}$, as a function of some field, $\Upsilon_{\breve{i}}$. The precise choice of the acceleration fields is subject to an evaluation of the relevant importance of the effect. Traditionally, these include inertial drag, lift and gravitational forces [122], but are not limited to those listed [65]. Within the scope of the present work, these fields are however limited to those of the steady Stokes regime for irrotational particles, whereby rotational lift forces are neglected. A detailed description of the specific particle model considered herein follows in Section 6.2.

In the context of low particle mass fraction (i.e. large Knudsen number) cases, the direct numerical simulation of discrete particle paths using a Lagrangian-particle framework can provide both attractive modelling and numerical advantages. In fact, LPTs easily lend themselves to numerical implementations using higher-order basic numerical methodologies such as linear multi-step methods or the Runge-Kutta hierarchy of explicit and implicit temporal discretizations [122]. Furthermore, in the absence of particle collisions,

these methods allow for the trivial prediction of complex phenomena, such as particle stream-crossing, otherwise broadly untreatable using traditional Eulerian-field based formulations [29, 109]. These methods are not without limitations however. While capable of providing accurate predictive simulations over a wide range of mass fractions, the computational expense of Lagrangian-particle methods can become prohibitive and infeasible as the number of particles becomes large. Specifically, related to stochastic modelling and applied probability theory, the convergence of Lagrangian-particle methods becomes increasingly expensive for high particle mass fraction (i.e. small Knudsen number) cases [35], as the required number of particle paths for statistically converged results increases remarkably. Likewise, such methods also introduce considerable complexities related to computational load balancing on parallel machines for flows exhibiting a large number of particles. As a result, these criticisms of Lagrangian-particle methods for gas-particle multiphase flows outside of free molecular flow-like regime motivate the implementation of more computationally affordable Eulerian-field methods.

2.2 Eulerian-Field Methods

Eulerian formulations adopt a field based description of the particle phase. More precisely, as opposed to Lagrangian-particle methods which are defined within the inertial frame of individual discrete particles, Eulerian-field methods are instead defined within a fixed spatial reference frame. The particle phase is thus not treated as discrete point-like entities but as a continuum, or field. Similar to traditional gas-dynamics, Eulerian-field models for gas-particle multiphase flows rest upon the continuum assumption and retain little, or no information, concerning the underlying microscopic structure of the particle phase. Instead, Eulerian-based formulations model continuous fields which describe the macroscopic quantities of the otherwise microscopic secondary particle phase, e.g., densities of mass, momentum, energy, and so forth. Eulerian field-based formulations are therefore locally far less information intensive than their Lagrangian counterparts, and, consequently, allow for the treatment of flows exhibiting a large number of particles (i.e. high particle mass fraction) at a significantly reduced computational cost.

Unfortunately, traditional Eulerian models can suffer from severe modelling artifacts due to the field-based treatment of the microscopic interactions of the particle phase. The simplest such Eulerian models are advection-dispersion models [110]. These models provide simple continuity equations which describe the balance of macroscopic quantities of the particle phase, such as,

$$\frac{\partial \rho}{\partial t} + \frac{\partial}{\partial x_\alpha}(\rho u_\alpha) = D \frac{\partial^2 \rho}{\partial x_\alpha \partial x_\alpha} + S \tag{2.5}$$

Here, the LHS of Equation (2.5) describes the advection of mass density while the RHS treats both mass diffusion and production terms. The application of these traditional Eulerian-field models has seen success in producing accurate predictive simulations for gas-particle flows in which the secondary particle phase is tightly coupled to the continuous carrier phase, or of low Knudsen number ($Kn \lesssim 0.01$) [86,94], i.e., where inter-particle collisions dominate. These successes are however limited. As mentioned, traditional Eulerian-field models produce significant modelling errors in capturing non-equilibrium dynamics expected of lightly coupled secondary particle phases, or of increasing Knudsen number particle flows entering the free particle flow regime. Recent works of both Vié *et al.* and Forgues *et al.* have explored these deficiencies [29, 109].

These modelling deficiencies thus provide strong motivation for the development of novel alternative Eulerian-based formulations for affordable, robust, and accurate prediction of gas-particle multiphase flows extending past the traditional continuum regime. Fortunately, the framework of statistical mechanics, or kinetic theory, provides such an alternative. The application of the method of moment-closures from the kinetic theory of gases has seen extensive success in producing Eulerian-based formulations for the treatment of gases beyond the continuum regime [31, 41, 67, 68, 70, 71, 99]. In the field of multiphase flows, moment-based methods based upon generic kinetic/Fokker-Plank equations have been previously considered to varying degrees of success [13, 63, 84, 85, 111, 125]. More recently, authors have notably demonstrated the applicability of higher-order moment-closures of the Boltzmann equation from the kinetic theory of gases for the Eulerian treatment of dilute monodispersed gas-particle multiphase flows [19, 29, 30, 62, 109]. Further, Forgues *et al.* have proposed a novel moment-based Eulerian framework for the treatment

of distinguishable particle phases, i.e., a particle phase exhibiting an arbitrary number of distinguishable particle properties [26]. Such a framework promises the possibility for the treatment of a variety of gas-particle multiphase flows previously favouring Lagrangian-particle models, e.g., fuel-spray modelling, and thus provides the motivation for the present work. As such, the following chapter provides a comprehensive summary of the fundamental concepts of moment-methods and moment-closures from the kinetic theory of gases on which the present work is formulated.

Chapter 3

Moment Methods and the Kinetic Theory of Gases

The situation of gas-particle multiphase flow shares many similarities with that of an ideal gas. In classical fluid mechanics, microscopic gas-particle structures are rarely of interest. In fact, for flows in which a large number of small particles exist, individual particle evolution is largely ignored. Instead, macroscopic quantities, such as mass density, momentum density, or energy density (so-called fluid variables) are of greater interest. The theory of moments from the kinetic theory of gases provides such a framework for the study of these statistical macroscopic quantities (moments) of the underlying collection of particles. Specifically, gases are described by single-particle phase-space density distribution functions [56], for which the evolution is governed by kinetic equations such as the Boltzmann equation.

The Boltzmann equation provides a microscopic description of the translational and inter-particle collisions which govern the evolution of rarefied gases [99]. The application of the Boltzmann equation for the description of rarefied gases, gases outside of the hydrodynamic regime, has been well established. More recently however, the theory of rarefied gas dynamics was extended to describe dilute particle phases [19, 30]. These recent advances have led to the inspiration of several novel higher-order moment-closures of the Boltzmann equation such to derive macroscopic transport equations for dilute gas-particle

multiphase flows. As such, the following chapter first presents the fundamental elements of the kinetic theory of gases and theory of moments, which has provided the framework for the kinetic description of multiphase flows. Secondly, moment-closure methods, specifically of the maximum-entropy hierarchy, are presented for the construction of macroscopic transport equations for the modelling of dilute gas-particle multiphase flows.

3.1 Introduction to the Kinetic Theory of Gases

The classical gas-kinetic theory provides a fundamentally statistical approach to the description of microscopic particle systems. In gas-kinetic theory, a gas is described as a collection of discrete and indistinguishable point-like particles. These particles are assumed to only interact through forces over distances significantly shorter than the mean-free particle path, and between which only binary collisions may occur. Further, these collisions are assumed to be statistically uncorrelated, i.e., particles have no history. With these seven fundamental gas-kinetic theory assumptions, a mathematical description of the particle ensemble is achieved through the definition of a phase-space density distribution function,

$$\mathcal{F} = (x_i, v_i, t)\,. \tag{3.1}$$

Importantly, phase-space describes a higher-dimensional space combining the physical spatial dimensions, and the abstraction of velocity-space as a spatial-like dimension. The evolution of this distribution function through spacetime is governed by a kinetic equation. For gas-kinetic theory, the Boltzmann equation is the central equation [8, 99],

$$\frac{\partial \mathcal{F}}{\partial t} + v_\alpha \frac{\partial \mathcal{F}}{\partial x_\alpha} + \frac{\partial}{\partial v_\alpha}\left(a_\alpha \mathcal{F}\right) = \frac{\delta \mathcal{F}}{\delta t}\,. \tag{3.2}$$

Note, index tensor notation rules such as the Einstein summation convention will be adopted throughout this work. Above, a_α is the particle acceleration induced by external fields, and the change of the phase-space density distribution through collisions is described by the Boltzmann collision integral on the right-hand-side of Equation (3.2) [38]. Kinetic models such as the BGK and ES-BGK models provide mathematically simple models for

the right-hand side collision operator. However, given the dilute particle-phase assumption of the present work, particle collisions shall remain largely neglected. Discussion of these models, along with a detailed elaboration of the fundamental *Stosszahlansatz* [99], shall therefore be omitted.

The Boltzmann equation is a high-dimensional partial differential equation which governs the evolution of a function providing vast amounts of information describing the state of the gas. Typically however, this enormous quantity of information is largely unnecessary. Instead, macroscopic quantities, or so-called fluid variables, are of usual interest. These traditional macroscopic quantities of the phase-space density distribution are obtained by taking moments of the distribution function, i.e., weighted integrals of the phase-space density distribution $\mathcal{F}$. This method is referred to as the theory of moments.

Moments of the phase-space density function are obtained by pre-multiplying the distribution by some appropriately chosen weight, w, and integrating over all velocity-space,

$$\iiint_{-\infty}^{\infty} w\,\mathcal{F}(x_i, v_i, t)\,\mathrm{d}v_i = \langle\, w\,\mathcal{F}\,\rangle\ . \tag{3.3}$$

In traditional gas-kinetic theory, the weight, w, is a velocity dependant weight and is typically a monomial of order $k \geq 0$, i.e., v_i^k. The shorthand notation, $\langle\mathcal{F}\rangle$, is used to denote integration over all velocity-space. Following the definition of Equation (3.3), the lowest-order, or zeroth-order ($k = 0$), moment of the phase-space density distribution function is,

$$n = \left\langle v_i^0 \mathcal{F} \right\rangle\ . \tag{3.4}$$

Here, n is the particle number density. Given the definition of Equation (3.1), it follows that the total number of particles in the spatial-volume V is given by,

$$N = \iiint_{\mathcal{V}} n\,\mathrm{d}x_i\,. \tag{3.5}$$

As such, $\mathcal{F}\,/n\,dx_i$ should therefore be interpreted as the probability of particles within $[x_i, x_i + \mathrm{d}x_i]$ having a velocity between $[v_i, v_i + \mathrm{d}v_i]$. Of course, the probability phase-space

density function is simply,

$$\left\langle \frac{\mathcal{F}}{n} \right\rangle = \langle f \rangle = 1 \,. \tag{3.6}$$

Increasing one order, the first-order velocity moment, $w = v_i$, of $\mathcal{F}$ results in the mean velocity of the particles, u_i,

$$n\, u_i = \langle v_i\, \mathcal{F} \rangle \ . \tag{3.7}$$

Considering an observer within the rest-frame, we can also define the peculiar, or deviatoric, velocity of the particles as $c_i = v_i - u_i$. Given this definition, we note the first-order deviatoric velocity moment, whereby $w = c_i$, vanishes,

$$\langle c_i\, \mathcal{F} = 0 \rangle \ . \tag{3.8}$$

Such changes in velocity weight definitions does however provide useful peculiar moments. Taking, for instance, the second-order deviatoric velocity moment, $w = c_i\, c_j$,

$$n\, \Theta_{ij} = \langle c_i\, c_j\, \mathcal{F} \rangle \ , \tag{3.9}$$

yields the symmetric second-order variance-covariance tensor containing the variance and covariance between each component of particle velocity. In the case of a monoatomic gas, Θ_{ij} is related to the hydrostatic pressure, $p = \rho\, \Theta_{ii}/3$, and full stress tensor, $\sigma_{ij} = -\rho\, \Theta_{ij}$, from traditional fluid dynamics which describes the internal, or thermal, energy of the macroscopic particle motion.

Notably, the analogous interpretation between the moments from traditional statistics (mean, variance) and the moments of the kinetic theory of gases (momentum, energy) has thus remained reasonably conspicuous. However, the physical interpretation of additional higher-order moments can become increasingly ambiguous as the order increases further, e.g., the third-order heat flux tensor,

$$n\, Q_{ijk} = \langle c_i\, c_j\, c_k\, \mathcal{F} \rangle \ , \tag{3.10}$$

straddles the limit of physical significance. Nonetheless, these higher-order moments can become important when rarefaction effects are notable, and can provide significant information regarding the state of particle distribution for problems of increasing non-equilibrium dynamics.

3.2 The Method of Moments

The Boltzmann equation provides a mathematical description for the advection, acceleration fields, and inter-particle interactions which govern the evolution of the phase-space density distribution function. Due to its high dimensionality, the direct numerical solution of Equation (3.2) is prohibitively costly for practical cases. Fortunately, the method of moments from the kinetic theory of gases provides a technique to produce balance laws for the evolution of the lower-dimensional moments of the phase-space density distribution function.

The application of the method of moments begins by, evidently, taking moments of the Boltzmann equation,

$$\begin{aligned}
\left\langle w\left(\frac{\partial \mathcal{F}}{\partial t}+v_\alpha\frac{\partial \mathcal{F}}{\partial x_\alpha}+\frac{\partial}{\partial v_\alpha}\left(a_\alpha\mathcal{F}\right)\right)\right\rangle &= \left\langle w\frac{\delta F}{\delta t}\right\rangle\,,\\
\left\langle w\frac{\partial \mathcal{F}}{\partial t}\right\rangle+\left\langle wv_\alpha\frac{\partial \mathcal{F}}{\partial x_\alpha}\right\rangle+\left\langle w\frac{\partial}{\partial v_\alpha}\left(a_\alpha\mathcal{F}\right)\right\rangle &= \left\langle w\frac{\delta F}{\delta t}\right\rangle\,,\\
\frac{\partial}{\partial t}\left\langle w\mathcal{F}\right\rangle+\frac{\partial}{\partial x_\alpha}\left\langle v_\alpha w\mathcal{F}\right\rangle+\left\langle w\frac{\partial}{\partial v_\alpha}\left(a_\alpha\mathcal{F}\right)\right\rangle &= \left\langle w\frac{\delta F}{\delta t}\right\rangle\,. \qquad (3.11)
\end{aligned}$$

This equation is referred to as Maxwell's equation of change and describes the equation of transfer for some arbitrary moment $\langle w\,\mathcal{F}\rangle$. The first-term of the left-hand side describes the describes the temporal rate of change of $\langle w\,\mathcal{F}\rangle$, and the second-term describes the flux of $\langle w\,\mathcal{F}\rangle$. The last-term of the left-hand side of Equation (3.11), which describes the effects of external acceleration fields, is often simplified using the product rule,

$$\left\langle\frac{\partial}{\partial v_\alpha}\left(a_\alpha w\mathcal{F}\right)\right\rangle=\left\langle w\frac{\partial}{\partial v_\alpha}\left(a_\alpha\mathcal{F}\right)\right\rangle+\left\langle a_\alpha\mathcal{F}\frac{\partial w}{\partial v_\alpha}\right\rangle\,. \qquad (3.12)$$

By application of the divergence theorem, it follows that the left-hand-side of Equation (3.12) is equal to zero,

$$\iiint_{-\infty}^{\infty}\frac{\partial}{\partial v_\alpha}\left(a_\alpha w\mathcal{F}\right)\mathrm{d}v_i=\oiint_{v_i\to\infty}\left(a_\alpha w\mathcal{F}\right)n_\alpha\mathrm{d}v_i=0\,, \qquad (3.13)$$

as there are no particles with infinite energy, i.e., $\mathcal{F}\left(v_i \to \infty\right) = 0$. Lastly, as previously mentioned in Section 3.1, the right-hand side collision operator of Equation (3.11) shall be omitted during this work. As a result, the transfer equation governing $\langle w\,\mathcal{F}\rangle$ finally becomes,

$$\frac{\partial}{\partial t}\langle w\mathcal{F}\rangle + \frac{\partial}{\partial x_\alpha}\langle v_\alpha w\mathcal{F}\rangle = \left\langle a_\alpha \mathcal{F}\frac{\partial w}{\partial v_\alpha}\right\rangle . \tag{3.14}$$

Generally, a vector of weights, $\boldsymbol{\mathcal{W}}$, is defined containing a collection of generating weights such to obtain a set of transfer equations for more than one moment. Following the process described above, this leads to,

$$\frac{\partial}{\partial t}\langle \boldsymbol{\mathcal{W}}\mathcal{F}\rangle + \frac{\partial}{\partial x_\alpha}\langle v_\alpha \boldsymbol{\mathcal{W}}\mathcal{F}\rangle = \left\langle a_\alpha \mathcal{F}\frac{\partial \boldsymbol{\mathcal{W}}}{\partial v_\alpha}\right\rangle . \tag{3.15}$$

Typically, the moment of the right-hand side of Equation (3.15) is a locally-stiff algebraic expression. Consequently, Equation (3.15) forms a system of first-order balance laws, which when expressed in balance-law form, is,

$$\frac{\partial}{\partial t}\boldsymbol{U} + \frac{\partial}{\partial x_\alpha}\boldsymbol{F_\alpha} = \boldsymbol{S}\,. \tag{3.16}$$

By convention, $\boldsymbol{U} = \langle \boldsymbol{\mathcal{W}}\mathcal{F}\rangle$ is the solution vector containing the moments of interest and $\boldsymbol{F_\alpha} = \langle v_\alpha \boldsymbol{\mathcal{W}}\mathcal{F}\rangle$ is the flux dyad corresponding to the conserved moments in $\boldsymbol{U}$. If the flux Jacobian, $\partial\boldsymbol{F}/\partial\boldsymbol{U}$, of this system is diagonalizable and its Eigenvalue problem has real-valued Eigenvalues, the system is said to be hyperbolic [15]—whereby the hyperbolicity of balance laws is known to bring many mathematical and numerical advantages; such as yielding finite speeds of information propagation and being easily solvable using a wealth of standard methods.

Importantly, the system described by both Equation (3.15) and Equation (3.16) is unclosed. For any order moment from a generating weight of $\boldsymbol{\mathcal{W}}$, information of a higher-order moment is required within the flux term, $\boldsymbol{F}_{\boldsymbol{\alpha}}$, and possibly source term, $\boldsymbol{S}$, which are not a priori related to the moments contained within the solution vector, $\boldsymbol{U}$. While not guaranteed in general, the source term is however typically closed for many practical applications. Nevertheless, a technique is required to produce a closed system of balance laws. Thankfully, the kinetic theory of gases provides such a technique – moment-closure.

3.3 Moment-Closures

Several techniques for treating the moment-closure problem presented in Section 3.2 have been developed. One such technique approaches the closure-problem through restricting the form of the underlying phase-space density distribution function, $\mathcal{F}$. In order to close a system of n moment equations, one proposes a form to $\mathcal{F}$ as a function of n free parameters, or closure coefficients. The values of these closure coefficients are chosen such to satisfy the lower-order moment equations of the desired solution vector, $\boldsymbol{U}$. Having satisfied these equations using the n degrees of freedom, the phase-space density distribution function is fully determined and the higher-order moments present within the flux and production terms can be integrated in terms of the determined closure coefficients. Interestingly, the phase-space distribution function is defined independently from the Boltzmann equation, whereby only a priori knowledge of the moments of $\mathcal{F}$ are required.

The simplest moment-closure within the kinetic theory of gases is the single-velocity closure. The phase-space density distribution function for such a closure describes a particle distribution which presents zero velocity deviation from the local average. As a result, the the phase-space density distribution function takes the form of a Dirac delta,

$$\mathcal{F} = n\,\delta\left(v_i - u_i\right) . \tag{3.17}$$

The implementation of the single-velocity closure is common in Eulerian gas-particle multiphase flow modelling. Evidently, these models are limited in their application and have been shown to produce significant artifacts for cases in which a range of velocities is ex-

pected [29,109]. Trivially, one can consider a sum of Dirac delta functions such to obtain a so-called discrete-velocity model, or multi-velocity model. However the application of such a closure requires *a priori* knowledge of the necessary quantity of velocity discretization points such to properly recover the underlying phase density distribution. Further, these closures can become numerically expensive as the number of necessary moment equations is linearly proportional to the number of discretized velocities.

A generalization to the discrete-velocity closure is known as the quadrature-based moment closures (QBMMs) [30, 31, 62]. These moment-closure methods specifically restrict the phase density to take one of a finite set of velocities – varying spatially and temporally. These methods have seen notable success in the modelling of traditionally erroneous cases, particularly in its ability to represent bimodal phase densities [19, 30, 62]. Unfortunately, the numerical implementation of quadrature-based moment closures can prove challenging, with alternative methods seeking to reduce the numerical burden of these methods leading to significant mathematical compromises such as the loss of rotational invariance [123]. Alternatively to discrete-velocity methods, one may instead consider the restriction of the phase-space density distribution function to a continuous function rather than discrete Dirac deltas. This moment-closure technique was first developed by Grad [40], who first proposed a Hermite polynomial expansion about the local equilibrium phase-space density distribution function, or Maxwellian, $\mathcal{F}_M$. The Grad-closure phase-space density distribution function therefore takes the form,

$$\mathcal{F}_{Grad} = \left(\alpha + \alpha_i \frac{\partial}{\partial c_i} + \alpha_{ij} \frac{\partial^2}{\partial c_i \partial c_j} + \alpha_{ijk} \frac{\partial^3}{\partial c_i \partial c_j \partial c_k} + ... \right) \mathcal{F}_M \,, \tag{3.18}$$

where one considers as many coefficients, $\boldsymbol{\alpha}$, as one has moments in the solution vector, $\boldsymbol{U}$. Unfortunately, it was quickly discovered that the resulting moment systems led to first-order balance laws whose flux Jacobian could develop complex Eigenvalues [99]. Also, the polynomial expansion is not guaranteed to remain positive and, thus, the assumed distribution function can be negative in some regions of phase-space. These facts have limited the wide-spread adoption of the method.

More recently, a hierarchy of moment methods based on the maximization of entropy was proposed [22,56,73]. Specifically, a distribution function is selected such to recover the desired moments within the solution vector, $\boldsymbol{U}$, while also maximizing the informational entropy,

$$\langle \mathcal{F} \ln \mathcal{F} \rangle \ , \tag{3.19}$$

which is the negative of the traditional thermodynamic entropy [40, 56, 57].

Traditionally, the proposed entropy maximization problem is approached using the method of Lagrange multipliers. In brief, the method of Lagrange multipliers seeks to reformulate the constrained maximization problem of Equation (3.19) such that the derivative test of an unconstrained problem may be applied. The problem may then be restated as

$$\boldsymbol{\mathcal{L}} = \boldsymbol{f} + \boldsymbol{\lambda}^T \boldsymbol{g} \, , \tag{3.20}$$

which is known as the Lagrangian function of the optimization problem – a high-dimensional function of the Lagrange multipliers, $\boldsymbol{\lambda}$. Here, $\boldsymbol{f}$ is the target function subject to the equality constraint of $g = 0$. Consequently, wherein f is the system's informational entropy, $\boldsymbol{g}$ describes the recovery of the known moments of $\boldsymbol{U}$. Explicitly, Equation (3.20) is simply

$$\boldsymbol{\mathcal{L}} = \langle \mathcal{F} \ln \mathcal{F} \rangle + \boldsymbol{\lambda}^T \left(\langle \boldsymbol{\mathcal{W}} \mathcal{F} \rangle - \boldsymbol{U} \right) \, . \tag{3.21}$$

The informational entropy is maximized when the Lagrange multipliers are determined such to yield a saddle point of the Lagrangian function,

$$\frac{\partial \boldsymbol{\mathcal{L}}}{\partial \mathcal{F}} = 0 \, . \tag{3.22}$$

Expanding the partial derivative of the LHS,

$$\frac{\partial \boldsymbol{\mathcal{L}}}{\partial \mathcal{F}} = \langle \ln \mathcal{F} - 1 \rangle + \boldsymbol{\lambda}^T \langle \boldsymbol{\mathcal{W}} \rangle \ , \tag{3.23}$$

$$0 = \left\langle \ln \mathcal{F} - 1 + \boldsymbol{\lambda}^T \boldsymbol{\mathcal{W}} \right\rangle \ , \tag{3.24}$$

the equality of Equation (3.24) is shown to be trivially satisfied for

$$\mathcal{F} = \exp\left(1 - \boldsymbol{\lambda}^T \boldsymbol{\mathcal{W}}\right) . \tag{3.25}$$

By convention, the Lagrange multipliers are expressed as the set of finite free parameters, $\boldsymbol{\alpha}$, such to obtain the maximum-entropy moment-closure phase-space density distribution function, [56, 57]

$$\mathcal{F} = \exp\left(\boldsymbol{\alpha}^{\boldsymbol{T}} \boldsymbol{\mathcal{W}}\right) . \tag{3.26}$$

Similar to the Grad-closure, one must consider as many free parameters, $\boldsymbol{\alpha}$, as one desires moments within $\boldsymbol{U}$. Further, while there is no *a priori* restriction on the choice of the moments within $\boldsymbol{U}$, the maximum-entropy hierarchy members are restricted to sets which ensure the strict-realizability of the phase density – more on this topic follows in Section 3.4.

The lowest-order member of the maximum-entropy hierarchy is the five-moment case. Selecting a vector of generating weights $\boldsymbol{\mathcal{W}}_5 = [m, m\,v_i, 1/2\,m\,v_i\,v_i]^{\mathrm{T}}$, the corresponding phase-space density distribution function is simply the Maxwellian,

$$\mathcal{F}_5 = \mathcal{F}_M = n\left(\frac{\rho}{2\pi p}\right)^{\frac{3}{2}} \exp\left(-\frac{\rho}{2p} c_i c_i\right) , \tag{3.27}$$

which yields the Euler equations - describing the lowest-order equilibrium dynamics for a compressible monoatomic gas.

Introducing higher-order non-equilibrium dynamics, the next member of the maximum-entropy closure is obtained by including the second-order anisotropic moments. Specifically, the ten-moment-closure is obtained by selecting a vector of generating weights, $\boldsymbol{\mathcal{W}}_{10} = [m, m\,v_i, m\,v_i\,v_j]^{\mathrm{T}}$. The corresponding phase-space density distribution function is

$$\mathcal{F}_{10} = \mathcal{G} = \frac{n}{(2\pi)^{\frac{3}{2}} \left(\det \Psi_{ij}\right)^{\frac{1}{2}}} \exp\left(-\frac{1}{2} \Psi_{ij}^{-1} c_i c_j\right) , \tag{3.28}$$

which takes the form of a multivariate-Gaussian distribution function. An extension to the local equilibrium distribution of Equation (3.27), the anisotropic Gaussian distribution, $\mathcal{G}$, notably admits non-zero off-diagonal pressure tensor entries, which allows for a divergence

from isotropy observed at local thermodynamic equilibrium. Importantly, the ten-moment maximum-entropy closure provides a first-order hyperbolic set of equations for the treatment of adiabatic viscous compressible gases. Wherein thermodynamic heat transfer can be neglected, the ten-moment maximum-entropy closure has been shown to successfully recover a wide range of equilibrium and non-equilibrium gas flows. [7, 9, 10, 57, 66, 69, 101]. More recently however, this ten-moment model has successfully been applied to the case of non-interacting gas-particle multiphase flows [26, 29, 109], and thus provides the fundamental framework and motivation for the present work.

3.4 Hyperbolicity and Realizability

The choice of one's higher-order moment-closure method is unfortunately not overtly trivial. Rather, the well-posedness and hyperbolicity of the set of Equations (3.16) is not inherently guaranteed by the choice an arbitrary phase-space density distribution function. As previously mentioned, Grad's method from the theory of rational extended thermodynamics has been well-criticized for its loss of hyperbolicity for deviations from local equilibrium [60,106]. Likewise, the polynomial expansion of the Grad closure has also been criticized for its admission of negative phase densities—whereby definition the phase-space density distribution function is a strictly-positive function. Precisely, these criticisms have motivated the proposal of alternative moment-closures which provide a set of well-posed and hyperbolic moment equations.

The hyperbolicity of a set of partial differential equations brings numerous favorable mathematical and numerical properties, e.g., stability and well-posedness of local Cauchy problems [28]. In selecting a higher-order moment-closure method, ensuring the strict-hyperbolicity of the system of moment equations thus becomes a prime selection criteria. Precisely, the maximum-entropy closure gains its favourability from the strict-hyperbolicity of the resulting moment system. Proof of the strict-hyperbolicity of the maximum-entropy

closure can be demonstrated by first defining the density and flux potentials,

$$h(\boldsymbol{\alpha}) = \langle \mathcal{F} \rangle = \left\langle e^{\boldsymbol{\alpha}^{\mathrm{T}} \boldsymbol{\mathcal{W}}} \right\rangle , \tag{3.29}$$

$$f_i(\boldsymbol{\alpha}) = \langle v_i \mathcal{F} \rangle = \left\langle v_i e^{\boldsymbol{\alpha}^{\mathrm{T}} \boldsymbol{\mathcal{W}}} \right\rangle . \tag{3.30}$$

The conserved moment vector, $\boldsymbol{U}$, and corresponding flux dyad, $\boldsymbol{F}$, follow from these definitions as

$$\boldsymbol{U} = \frac{\partial h(\boldsymbol{\alpha})}{\partial \boldsymbol{\alpha}} = \left\langle \boldsymbol{\mathcal{W}}\, e^{\boldsymbol{\alpha}^{\mathrm{T}} \boldsymbol{\mathcal{W}}} \right\rangle , \tag{3.31}$$

$$\boldsymbol{F} = \frac{\partial f_i(\boldsymbol{\alpha})}{\partial \boldsymbol{\alpha}} = \left\langle \boldsymbol{\mathcal{W}}\, v_i e^{\boldsymbol{\alpha}^{\mathrm{T}} \boldsymbol{\mathcal{W}}} \right\rangle . \tag{3.32}$$

The flux Jacobian, $\partial \boldsymbol{F} / \partial \boldsymbol{U}$, may then be obtained by further differentiating both Equations (3.31) and (3.32),

$$\frac{\partial \boldsymbol{U}}{\partial \boldsymbol{\alpha}} = \frac{\partial h(\boldsymbol{\alpha})}{\partial \boldsymbol{\alpha} \partial \boldsymbol{\alpha}} = \left\langle \boldsymbol{\mathcal{W}} \boldsymbol{\mathcal{W}}^{\mathrm{T}}\, e^{\boldsymbol{\alpha}^{\mathrm{T}} \boldsymbol{\mathcal{W}}} \right\rangle , \tag{3.33}$$

$$\frac{\partial \boldsymbol{F}}{\partial \boldsymbol{\alpha}} = \frac{\partial f_i(\boldsymbol{\alpha})}{\partial \boldsymbol{\alpha} \partial \boldsymbol{\alpha}} = \left\langle \boldsymbol{\mathcal{W}} \boldsymbol{\mathcal{W}}^{\mathrm{T}}\, v_i e^{\boldsymbol{\alpha}^{\mathrm{T}} \boldsymbol{\mathcal{W}}} \right\rangle , \tag{3.34}$$

such that,

$$\frac{\partial \boldsymbol{F}}{\partial \boldsymbol{U}} = \left(\frac{\partial \boldsymbol{U}}{\partial \boldsymbol{\alpha}} \right)^{-1} \frac{\partial \boldsymbol{F}}{\partial \boldsymbol{\alpha}} = \left(\frac{\partial h(\boldsymbol{\alpha})}{\partial \boldsymbol{\alpha} \partial \boldsymbol{\alpha}} \right)^{-1} \frac{\partial f_i(\boldsymbol{\alpha})}{\partial \boldsymbol{\alpha} \partial \boldsymbol{\alpha}} . \tag{3.35}$$

The hyperbolicity of the system of moment equations is guaranteed if the flux Jacobian is diagonalizable and yields strictly real-valued Eigenvalues. According to the definitions of Equations (3.33) to (3.35), hyperbolicity of the maximum-entropy closure is guaranteed provided that $\left\langle \boldsymbol{\mathcal{W}} \boldsymbol{\mathcal{W}}^{\mathrm{T}}\, e^{\boldsymbol{\alpha}^{\mathrm{T}} \boldsymbol{\mathcal{W}}} \right\rangle$ is symmetric positive-definite. One observes quite plainly the weight vector product, $\boldsymbol{\mathcal{W}} \boldsymbol{\mathcal{W}}^{\mathrm{T}}$, is by definition inherently strictly symmetric positive-definite. Whereby the maximum-entropy phase density, $\mathcal{F} = e^{\boldsymbol{\alpha}^{\mathrm{T}} \boldsymbol{\mathcal{W}}}$, admits strictly non-zero positive densities, for any arbitrary non-zero real-valued vector, $\boldsymbol{m}$, the following

statement holds true:

$$\boldsymbol{m}^{\mathrm{T}} \frac{\partial h(\boldsymbol{\alpha})}{\partial \boldsymbol{\alpha} \partial \boldsymbol{\alpha}} \boldsymbol{m} = \left\langle \boldsymbol{m}^{\mathrm{T}} \boldsymbol{\mathcal{W}} \boldsymbol{\mathcal{W}}^{\mathrm{T}} e^{\boldsymbol{\alpha}^{\mathrm{T}} \boldsymbol{\mathcal{W}}} \boldsymbol{m} \right\rangle \geq 0 \,, \tag{3.36}$$

$$\left\langle \left(\boldsymbol{m}^{\mathrm{T}} \boldsymbol{\mathcal{W}} \right)^2 \mathcal{F} \right\rangle \geq 0 \,. \tag{3.37}$$

Specifically, as $\left(\boldsymbol{m}^{\mathrm{T}} \boldsymbol{\mathcal{W}}\right)^2$ is guaranteed positive, $\left\langle \boldsymbol{\mathcal{W}} \boldsymbol{\mathcal{W}}^{\mathrm{T}} e^{\boldsymbol{\alpha}^{\mathrm{T}} \boldsymbol{\mathcal{W}}} \right\rangle$ is then known to be strictly convex positive-definite and the hyperbolicity of the moment equations is guaranteed.

Despite its mathematical elegance, the maximum-entropy closure method is not without any discernable criticisms. While the criticisms highlighted herein of Grad's method have been shown to be alleviated by the maximum-entropy closure, the concern of realizability has not yet been discussed. The realizability of a moment state is defined as the existence of a positive distribution which corresponds to a given set of moments. Given the maximum-entropy phase-space density distribution function, satisfying the realizability criteria requires the polynomial in the exponent to be negative in both velocity limits, $c_i \to \pm\infty$. This requirement implies a restriction on the Lagrange multipliers of the system, and also restricts the set of admittable moments within $\boldsymbol{U}$ as mentioned in Section 3.3. Authors have explored the limits of the realizable space of the maximum-entropy closure hierarchy *ad-nauseam* [23, 46–48], determining the equilibria—the Maxwellians—lie on the limit of the realizable space [99]. As a result, for even small deviations from local equilibrium, the set of Lagrange multipliers may be artificially restricted such to yield a physically realizable phase density. Importantly, these criticisms of the maximum-entropy closure are notably graver for maximum-entropy closures of higher-order than the previously presented ten-moment model on which this work is based. However, encounters with the physical realizability limits of the ten-moment maximum-entropy closure do occur—depending particularly on the behavior of the yet discussed source term, $\boldsymbol{S}$. A further discussion of these concerns follows in Section 7.2.1. Nonetheless, barring higher-order closures, the attractive mathematical and numerical properties of the ten-moment maximum-entropy closure far outweigh the realizability concerns arising from this closure and thus justify its application in this work.

Chapter 4

Polydisperse Gaussian-Moment Models

The application of moment-methods, e.g., single-velocity, quadrature-based, Grad-closures and maximum-entropy closures, has seen varied success in providing accurate Eulerian-based predictions for gas-particle multiphase flows. Notably however, these investigations have widely been limited to strictly monokinetic (single-velocity) and polykinetic (multi-velocity) particle distributions. In most natural and industrial processes however, particles exhibit a range of distinguishing properties beyond simple polykineticy. In complex fuel-spray or bio-aerosol applications for instance, additional particle information such as size and temperature drive significant thermodynamic processes which influence the evolution of the particle flow. Fortunately, the kinetic theory of gases provides a mathematical framework which can provide the direct treatment of such extended particle properties. Precisely, following their investigations of high-order maximum-entropy closures for gas-particle multiphase flows, recent work by Forgues *et al.* [26] has provided a novel framework for the treatment of an arbitrary number of distinguishing particle properties inspired from the kinetic theory of gases. This framework promises to allow pervasive extension of moment-based models to previously unconsidered gas-particle multiphase flow applications—while providing improved large-scale computational performance given its Eulerian-field formulation. Within the following chapter, the theory of extended particle statistics inspired from the kinetic theory of gases is presented. Second, the framework provided by Forgues *et al.* is then discussed.

4.1 An Extension to the Kinetic Theory of Gases

Previously in Chapter 3, the kinetic theory of gases provided an mathematical description for the statistical treatment of a particle phase based upon arguments of traditional gas-dynamics. Recalling the fundamental assumptions provided therein, particles were importantly assumed to be physically identical, i.e., indistinguishable. While reasonable at the molecular level, particle distributions in practical fuel-spray, bio-aerosol, atmospheric pollution, etc. problems are expected to exhibit a range of distinguishing properties. These properties drive important thermodynamic processes which govern the behavior of the particle flow, e.g., phase change, radiation and reactivity. Fortunately, the kinetic theory of gases can be extended to capture these additional particle properties.

In order to treat particle phases composed of an arbitrary number of additional distinguishable variables, the phase-space density distribution function, $\mathcal{F}$, from traditional kinetic theory must be supplemented with additional information. Whereby $\mathcal{F}$ is already a high-dimensional function of phase-space, the traditional distribution function can be extended into further higher dimensions,

$$\mathcal{F} = \mathcal{F}(x_i, v_i, \zeta_{\breve{i}}, t)\,. \tag{4.1}$$

Here, $\zeta_{\breve{i}}$ represents an arbitrary particle property of interest, e.g., size, temperature, radioactivity, etc. and $\mathcal{F}$ describes the particle density within the extended phase-space. The breve adorned indices, $\breve{i}$, are used to distinguish separate independent dimensions of the extended variable-space, $\zeta_{\breve{i}}$, which do not transform as regular tensors—unadorned indices are reserved for the treatment of traditional tensors, e.g., velocity tensors. Where the expanded phase-space density distribution function is defined as $\mathcal{F}(x_i, v_i, \zeta_0, \zeta_1, \ldots, \zeta_N)$ for N arbitrary variables, the collisionless kinetic equation governing its evolution becomes

$$\frac{\partial \mathcal{F}}{\partial t} + v_\alpha \frac{\partial \mathcal{F}}{\partial x_\alpha} + \frac{\partial}{\partial v_\alpha}\left(a_\alpha \mathcal{F}\right) + \sum_{\breve{i}=0}^{N} \frac{\partial}{\partial \zeta_{\breve{i}}}\left(\Upsilon_{\breve{i}} \mathcal{F}\right) = 0\,. \tag{4.2}$$

Similar to a_α which describes acceleration fields acting upon the particles, here $\Upsilon_{\breve{i}}$ describes the time rate of change of the $\breve{i}$th property, $\zeta_{\breve{i}}$.

By extension, moments of the extended distribution function are defined as

$$\langle w\mathcal{F} \rangle = \iiint\limits_{\infty} \cdots \int w\mathcal{F} \, \mathrm{d}\zeta_{\breve{i}} \, \mathrm{d}v_i \,, \tag{4.3}$$

where integration spans both velocity-space and the extended variable-space. As a result, a particular caveat is raised concerning the domain of the extended variable-space. In general, no restriction is placed on the span of $\zeta_{\breve{i}}$. In fact, $\zeta_{\breve{i}}$ need not span all real numbers, nor be continuous in nature. The choice of variable does however restrict the integration bounds of Equation (4.3), and will also limit the applicability of certain moment-closure techniques. Particularly, discrete variables, e.g., chemical composition, would inherently be better suited to single-property (analogous to single-velocity) or quadrature-based moment-closures—perhaps also inspiring hybrid continuous-discrete methods. Investigations into such moment-closures will however remain beyond the scope of the present work.

While in traditional gas-kinetic theory the weight, w, is a velocity dependant weight, it may also express a $\zeta_{\breve{i}}$ dependant weight within the context of the extended moment definition of Equation (4.3). Similar to the first-order velocity moment, the average value of the $\breve{i}$th variable, $\zeta_{\breve{i}}$, is defined as,

$$n \, \bar{\zeta}_{\breve{i}} = \langle \zeta_{\breve{i}} \, \mathcal{F} \rangle \ . \tag{4.4}$$

Note, within the above equation, the bar notation is used to differentiate $\zeta_{\breve{i}}$ from its average value $\bar{\zeta}_{\breve{i}}$. Given Equation (4.4), the deviatoric variable vector, $c_{\tilde{i}}$, follows by definition as,

$$c_{\tilde{i}} = \left[v_i - u_i, \ \zeta_{\breve{i}} - \bar{\zeta}_{\breve{i}} \right]^{\mathbf{T}} \ , \tag{4.5}$$

which is notably adorned by $\tilde{i}$ tensor indices which follow tensor contraction notation, but do not follow standard tensor transformations. The definition of increasingly higher-order moments, e.g., variance and skewness, follows as in traditional gas-kinetic theory. Most interestingly however, by extension of the variable space, higher-order statistical correlations between the extended particle variables of $\mathcal{F}$ may be evaluated. For instance, the lowest-order moments of such statistics are contained within the second-order deviatoric

moment, defined as

$$n\,\Psi_{\tilde{i}\tilde{j}} = \left\langle c_{\tilde{i}}\, c_{\tilde{j}}\, \mathcal{F} \right\rangle \,. \tag{4.6}$$

Here, the extended variance-covariance tensor, $\Psi_{\tilde{i}\tilde{j}}$, contains both the variance and covariance moments of the traditional velocity components, v_i, and additional variables, $\zeta_{\breve{i}}$. Expanded, it becomes

$$\Psi_{\tilde{i}\tilde{j}} = \begin{bmatrix} \Psi_{ij} & \Psi_{i\breve{j}} \\ \Psi_{\breve{i}j} & \Psi_{\breve{i}\breve{j}}\,, \end{bmatrix} \,, \tag{4.7}$$

with the symmetric off-diagonal entries, $\Psi_{\breve{i}j}$ and $\Psi_{i\breve{j}}$, describing, for instance, the second-order covariance between velocity and the additional particle properties. Such statistical information provides insightful information regarding the underlying coupling between variables and consequent particle behaviour—information which is otherwise unavailable without post-processing of data using traditional Lagrangian-particle formulations.

The methodology for obtaining an extended set of transfer equations for the extended moments of $\mathcal{F}$ is consistent with that of traditional gas-kinetic theory. By simple extension, the collisionless Maxwell's equation of change for the extended phase density becomes

$$\frac{\partial}{\partial t}\left\langle \boldsymbol{\mathcal{W}}\mathcal{F}\right\rangle + \frac{\partial}{\partial x_\alpha}\left\langle v_\alpha \boldsymbol{\mathcal{W}}\mathcal{F}\right\rangle = \left\langle a_\alpha \mathcal{F}\frac{\partial \boldsymbol{\mathcal{W}}}{\partial v_\alpha}\right\rangle + \sum_{\breve{i}=0}^{N}\left\langle \boldsymbol{\mathcal{W}}\,\frac{\partial}{\partial \zeta_{\breve{i}}}\left(\Upsilon_{\breve{i}}\mathcal{F}\right)\right\rangle \,, \tag{4.8}$$

which can be expressed in balance-law form,

$$\frac{\partial}{\partial t}\boldsymbol{U} + \frac{\partial}{\partial x_\alpha}\boldsymbol{F_\alpha} = \boldsymbol{S}\,, \tag{3.16}$$

as is convention from traditional gas-kinetic theory. Of course, the generating weight vector, $\boldsymbol{\mathcal{W}}$, of Equation (4.8) contains both velocity, v_i, and extended variable, $\zeta_{\breve{i}}$, dependant weights. As a result, the conserved solution vector, $\boldsymbol{U} = \langle \boldsymbol{\mathcal{W}}\mathcal{F}\rangle$, now contains an extended set of both velocity and additional particle variable moments. Again however, the system of equations remains unclosed, i.e., the flux dyad, $\boldsymbol{F}_\alpha = \langle v_\alpha \boldsymbol{\mathcal{W}}\mathcal{F}\rangle$, remains dependant of a higher-order velocity moment than its corresponding entry in $\boldsymbol{U}$. Consequently, the application of a moment-closure technique is required such to obtain a closed system of equations for the extended set of moments. As was briefly discussed, the inherent nature of

the choice of extended set of variables may restrict one's choice of moment-closure method. For example, in the case of discrete variables, hybrid discrete-velocity-like moment-closures, or quadrature-based moment-closures (QBMMs), may lend themselves nicely to recovering the underlying description of $\mathcal{F}$. In the present work however, the set of possible ζ_i is restrained to strictly continuous real-valued variables. Given the various modelling and numerical advantages discussed in Section 3.4, a maximum-entropy moment-closure method can thus provide an attractive framework for closing the extended moment-system of Equation (4.8).

4.2 The Polydisperse Gaussian-Moment Model Framework

The application of the maximum-entropy moment-closure technique for the extended set of moment equations from Equation (4.8) was first proposed by Forgues *et al.* [26]. The derivation of their proposed framework follows the methodology of the traditional maximum-entropy moment-closure technique—refer to Section 3.3. Specifically, the entropy-maximization problem of Equation (3.19) is expanded to the case of the extended phase-space density distribution function, $\mathcal{F}$, of Equation (4.1). Where the informational entropy for both the velocity and additional variable is maximized, the maximum-entropy moment-closure extended phase-space density distribution function can be shown to maintain its exponential form,

$$\mathcal{F} = \exp\left(\boldsymbol{\alpha}^{\boldsymbol{T}}\boldsymbol{\mathcal{W}}\right) , \tag{3.26}$$

from traditional extended thermodynamics. Again, the free parameters, $\boldsymbol{\alpha}$, of $\mathcal{F}$ are determined as a function of the target set of moments within the extended conserved moment vector, $\boldsymbol{U}$.

Recently, Forgues *et al.* [26] have proposed a generalized extension to the previously discussed ten-moment maximum-entropy closure. Specifically, the traditional Gaussian-moment model derived from the ten-moment closure is extended to an arbitrary number of additional distinguishing particle properties by extending the vector of generating weights such to include both first-order and second-order extended variable weights,

$$\boldsymbol{\mathcal{W}} = \left[1 \; v_i \; \zeta_{\breve{i}} \; v_i v_j \; \zeta_{\breve{i}}\zeta_{\breve{j}} \; v_i\zeta_{\breve{i}}\right]^{\mathrm{T}} . \tag{4.9}$$

The resulting maximum-entropy phase-space density distribution function takes the form of

$$\tilde{G} = \frac{n}{(2\pi)^{\frac{3+N}{2}} \left(\det \Psi_{\tilde{i}\tilde{j}}\right)^{\frac{1}{2}}} \exp\left(-\frac{1}{2}\Psi^{-1}_{\tilde{i}\tilde{j}} c_{\tilde{i}} c_{\tilde{j}}\right) , \tag{4.10}$$

describing an extended multivariate-Gaussian distribution for N considered additional distinguishing variables. Trivially, when $N = 0$, Equation (4.10) recovers the non-extended ten-moment distribution in Equation (3.28). Moreover, the proposed maximum-entropy closure restricts the underlying distribution of the additional distinguishable variables to a normal distribution. The validity of such a restriction is not inherently guaranteed, and requires justification in the choice of the selected variables.

Given the distribution function, $\tilde{G}$, the resulting set of spacetime-coupled partial differential equations (PDEs) of the Polydispersed Gaussian-moment model (PGM) framework becomes,

$$\frac{\partial n}{\partial t} + \frac{\partial}{\partial x_\alpha} n u_\alpha = S^{(0)} , \tag{4.11}$$

$$\frac{\partial}{\partial t} n u_i + \frac{\partial}{\partial x_\alpha} n(\Psi_{i\alpha} + u_i u_\alpha) = S^{(1)}_i , \tag{4.12}$$

$$\frac{\partial}{\partial t} n\zeta_{\breve{i}} + \frac{\partial}{\partial x_\alpha} n\left(\Psi_{\alpha\breve{i}} + u_\alpha \zeta_{\breve{i}}\right) = S^{(2)}_{\breve{i}} , \tag{4.13}$$

$$\frac{\partial}{\partial t} n\left(\Psi_{ij} + u_i u_j\right) + \frac{\partial}{\partial x_\alpha} n\left(u_i\Psi_{j\alpha} + u_j\Psi_{i\alpha} + u_\alpha\Psi_{ij} + u_i u_j u_\alpha\right) = S^{(3)}_{ij} , \tag{4.14}$$

$$\frac{\partial}{\partial t}\, n(\Psi_{\breve{i}\breve{j}} + \zeta_{\breve{i}}\zeta_{\breve{j}}) + \frac{\partial}{\partial x_\alpha}\, n\left(u_\alpha \Psi_{\breve{i}\breve{j}} + \zeta_{\breve{i}}\Psi_{\alpha\breve{j}} + \zeta_{\breve{j}}\Psi_{\alpha\breve{i}} + u_\alpha \zeta_{\breve{i}}\zeta_{\breve{j}}\right) = S^{(4)}_{\breve{i}\breve{j}}\,, \tag{4.15}$$

$$\frac{\partial}{\partial t} n(\Psi_{i\breve{i}} + u_i\zeta_{\breve{i}}) + \frac{\partial}{\partial x_\alpha}\, n\left(u_i \Psi_{\alpha\breve{i}} + u_\alpha \Psi_{i\breve{i}} + \zeta_{\breve{i}}\Psi_{i\alpha} + u_i u_\alpha \zeta_{\breve{i}}\right) = S^{(5)}_{i\breve{i}}\,. \tag{4.16}$$

Obviously, when $N = 0$, the above equations reduce to Equations (4.11), (4.12) and (4.14) and recover the traditional ten-moment maximum-entropy closure equations [26, 29, 109]. Most notably however, the PGM framework provides a generalized set of first-order hyperbolic PDEs for the treatment of gas-particle multiphase flows exhibiting an arbitrary number of additional distinguishing particle properties. In fact, assuming all additional distinguishing variables have domains spanning all real numbers, the strict-hyperbolicity and Eigenstructure of the maximum-entropy moment-closure hierarchy is conserved by the PGM framework [26]. However, not all distinguishing variables, $\zeta_{\breve{i}}$, are guaranteed to span the full-space of real numbers, e.g., particle diameter is non-negative real number, $\{d \in \mathbb{R} \,|\, d \geq 0\}$. In such a case, the odd function symmetry of odd-numbered moments is lost due to integration over the positive half-space of the $\zeta_{\breve{i}}$ variable-space, subsequently introducing higher-order skewness moments and altering the Eigenstructure of the resulting PDEs. Some care must thus be taken in selecting the set of additional distinguishing variables to maintain the numerous modelling and numerical advantages of the maximum-entropy closure. A discussion on the choice of variables for the application of spray modelling follows within the next chapter.

Chapter 5

A Two-Scalar PGM for Evaporating Sprays

The case of sprays is a particularly challenging gas-particle multiphase flow in which the particle phase is considered as a discrete liquid phase in the form of droplets within a continuously connected gaseous carrier phase [93]. On various scales, complex transport and thermodynamic processes are observed within the droplet phase, which induce strong stiff coupling between the droplet and carrier phases. Traditionally, the numerical treatment of detailed evaporating sprays has largely been considered with Lagrangian-particle methods due to the subgrid nature of droplet-heating and -vaporization [93]. Investigation into the application of kinetic modelling for sprays has however been performed; whereby the mesoscopic statistical formalism for the description of droplet transport was first proposed by Williams in his seminal paper in 1958 [50,79,102,117,118]. Inspired from the kinetic theory of gases, a statistical description for the underlying droplet phase, or droplet distribution function (DDF), was developed for applications in spray modelling. The proposed DDF is a specialization to the extended phase-space density distribution function derived from the extended kinetic description of gas-dynamics presented in Section 4.1. Specifically, in order to capture strong size and temperature dependant inertial, heating and vaporization driven coupling, the phase-space density distribution function is supplemented with a minimum of two additional scalars which provide such additional dimensional and thermal information regarding the underlying droplet phase.

Where the Weber number (We) is small, i.e., droplet deformation due to viscous interactions with the carrier phase are small, and the droplet Knudsen number (Kn) is high, a monocomponent description of droplet size can be considered reasonable [117, 118]. As such, for small, relatively low-velocity spray problems, polydispersity of the droplet distribution function can be described by a single additional variable for size—which in the present work is the droplet diameter, d. Regarding droplet temperature, the absolute temperature, T, of a droplet, measured in Kelvin, becomes a rather trivial choice for the polythermal description of the droplet distribution. The resulting phase-space density distribution function, or so-called droplet distribution function, for sprays is thus represented by the high-dimensional function,

$$\mathcal{F} = \mathcal{F}(x_i, v_i, d, T, t)\,. \tag{5.1}$$

The corresponding extended kinetic equation for the DDF, $\mathcal{F}$, is obtained from the generalized extended kinetic equation, Equation (4.2),

$$\frac{\partial \mathcal{F}}{\partial t} + v_\alpha \frac{\partial \mathcal{F}}{\partial x_\alpha} + \frac{\partial}{\partial v_\alpha}\left(a_\alpha \mathcal{F}\right) + \sum_{\breve{i}=0}^{N} \frac{\partial}{\partial \zeta_{\breve{i}}}\left(\Upsilon_{\breve{i}} \mathcal{F}\right) = \frac{\delta \mathcal{F}}{\delta t}\,, \tag{4.2}$$

$$\frac{\partial \mathcal{F}}{\partial t} + v_\alpha \frac{\partial \mathcal{F}}{\partial x_\alpha} + \frac{\partial}{\partial v_\alpha}\left(a_\alpha \mathcal{F}\right) + \frac{\partial}{\partial d}\left(\Upsilon_d \mathcal{F}\right) + \frac{\partial}{\partial T}\left(\Upsilon_T \mathcal{F}\right) = Q + \Gamma\,. \tag{5.2}$$

This extended kinetic equation is commonly referred to as the Williams-Boltzmann equation [117]. Here, both Υ_d and Υ_T are the time rates of change of the additional particle variables for diameter and temperature, respectively, and represent droplet heating and vaporization processes. As for the RHS collision operator of Equation (4.2), it is expanded into Q and Γ which also describe droplet nucleation, liquid breakup, and collisions. However, in low mass fraction situations in which small droplets are considered, these effects may largely be neglected [81, 102, 117, 118]. The collisionless Williams-Boltzmann equation therefore becomes,

$$\frac{\partial \mathcal{F}}{\partial t} + v_\alpha \frac{\partial \mathcal{F}}{\partial x_\alpha} = -\frac{\partial}{\partial v_\alpha}\left(a_\alpha \mathcal{F}\right) - \frac{\partial}{\partial d}\left(\Upsilon_d \mathcal{F}\right) - \frac{\partial}{\partial T}\left(\Upsilon_T \mathcal{F}\right)\,. \tag{5.3}$$

As was previously mentioned however, some consideration to the physical nature of the extended variable-space is required. Rather, both the particle diameter and temperature are strictly non-negative real numbers, i.e., $\{d \in \mathbb{R} \,|\, d \geq 0\}$ and $\{T \in \mathbb{R} \,|\, T \geq 0\}$, respectively. Physical moments of the proposed DDF would therefore be evaluated as

$$\langle w\mathcal{F} \rangle = \iiint\limits_{\infty} \iint\limits_{0}^{\infty} w\mathcal{F} \, \mathrm{d}T \, \mathrm{d}d \, \mathrm{d}v_i \,, \tag{5.4}$$

where diameter- and temperature-space are integrated over the positive half-spaces. Assuming both improper integrals are convergent, this particularity introduces significant complexities, as was explored by Marchildon [61]. A solution to the diameter-space constraint was proposed by Forgues *et al.* in their original one-scalar treatment of a polydisperse particle phase [26]. A mapping of the non-negative real diameter-space to the span of all real numbers is proposed by applying a natural logarithm transformation to the diameter-space, whereby $\ln(d) \,:\, (d \geq 0) \rightarrow \mathbb{R}$, and,

$$\mathcal{F} = \mathcal{F}(x_i, v_i, \ln(d), T, t) \,. \tag{5.5}$$

Of course, the mapping alters the underlying kinetic equation, such that the equivalent collisionless Williams-Boltzmann equation becomes

$$\frac{\partial \mathcal{F}}{\partial t} + v_\alpha \frac{\partial \mathcal{F}}{\partial x_\alpha} = -\frac{\partial}{\partial v_\alpha} \left(a_\alpha \mathcal{F} \right) - \frac{\partial}{\partial \ln(d)} \left(\frac{\Upsilon_d}{d} \mathcal{F} \right) - \frac{\partial}{\partial T} \left(\Upsilon_T \mathcal{F} \right) \,. \tag{5.6}$$

Regarding temperature-space, an assumption of near-zero contribution of the negative half-space is proposed. In most, if not all, practical spray applications, temperature distributions are unlikely to approach absolute zero. Consequently, despite integration over the non-physical negative temperature half-space, moments of the DDF are assumed to

remain physical. Moments of the DDF can then taken as

$$\langle w\mathcal{F}\rangle \approx \idotsint_{\infty} w\mathcal{F}\,\mathrm{d}T\,\mathrm{d}\ln(d)\,\mathrm{d}v_i \approx \idotsint_{\infty} \left(\cancel{\int_{-\infty}^{0} w\mathcal{F}\,\mathrm{d}T}^{\;0} + \int_{0}^{\infty} w\mathcal{F}\,\mathrm{d}T\right)\mathrm{d}\ln(d)\,\mathrm{d}v_i\,. \tag{5.7}$$

As discussed at length in previous chapters, the theory of moments from the kinetic theory of gases leads to the formulation of an unclosed system of partial differential moment-equations which reduces the high-dimensionality of Equation (5.3). Fortunately, the Polydisperse Gaussian-moment hierarchy of maximum-entropy closures provides an elegant moment-closure for the William-Boltzmann-based set of moment-equations.

Where two additional distinguishing particle properties ($N = 2$) have been considered, the vector of generating weights is selected as,

$$\boldsymbol{\mathcal{W}} = \begin{bmatrix} 1 & v_i & \ln(d) & T & v_iv_j & \ln(d)^2 & T^2 & v_i\ln(d) & v_iT & \ln(d)T \end{bmatrix}^{\mathrm{T}}. \tag{5.8}$$

The above set of weights effectively describes to the two-scalar specialization of the PGM family of models. The corresponding droplet distribution function resulting from the two-scalar PGM formulation becomes

$$\tilde{G} = \frac{n}{d\,(2\pi)^{\frac{5}{2}}\left(\det\Psi_{\tilde{i}\tilde{j}}\right)^{\frac{1}{2}}}\exp\left(-\frac{1}{2}\Psi^{-1}_{\tilde{i}\tilde{j}}c_{\tilde{i}}c_{\tilde{j}}\right), \tag{5.9}$$

where the extended deviatoric variable vector, $c_{\tilde{i}}$, and extended variance-covariance matrix, $\Psi_{\tilde{i}\tilde{j}}$, are respectively

$$c_{\tilde{i}} = \begin{bmatrix} v_i - u_i & \ln(d) - \mu & T - \theta \end{bmatrix}^{\mathrm{T}}, \qquad \text{and} \qquad \Psi_{\tilde{i}\tilde{j}} = \begin{bmatrix} \Psi_{ij} & \Psi_{id} & \Psi_{iT} \\ \Psi_{jd} & \Psi_{dd} & \Psi_{dT} \\ \Psi_{jT} & \Psi_{dT} & \Psi_{TT} \end{bmatrix}. \tag{5.10}$$

According to Equation (5.9), one plainly remarks the assumed natural lognormal distribution of particle diameters due to the change of variables defined in Equation (5.5). Such an assumption has several physical and mathematical arguments. Namely, measurements

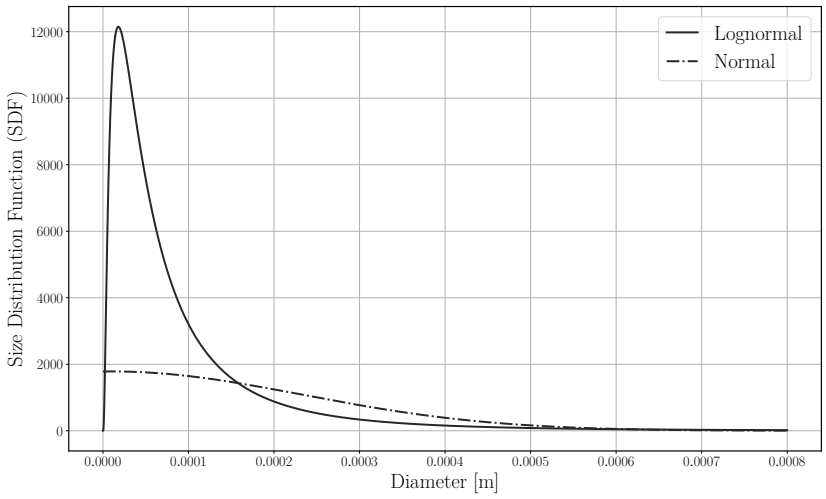

Figure 5.1: Comparison of lognormal diameter size distribution function against equivalent normal diameter size distribution function.

of particle size distributions in a variety natural bio-aerosol, fuel-injection, atmospheric pollutant, etc. processes have been widely demonstrated to generally fit lognormal distributions [2, 6, 24, 25, 54, 58, 59, 72, 107, 108, 120, 121] Furthermore, adoption of a lognormal distribution functions recovers expected physical behaviour in the lower-limit, where $d \to \mathbf{0}$, given the lognormal-mapping of diameter space. Specifically, as $\ln(d) \, : \, (d \geq 0) \to \mathbb{R}$, the lower-limit of the DDF is by definition,

$$\lim_{d \to \mathbf{0}} \tilde{G} \to \lim_{ln(d) \to -\infty} \tilde{G} = \mathbf{0} \, . \tag{5.11}$$

Consequently, the underlying DDF, $\tilde{G}$, admits no zero-size particles, as would physically be expected. For visualization purposes, Figure 5.1 provides a comparison of a lognormal distribution against a normal distribution for an arbitrary size distribution. However, this mathematical property of $\tilde{G}$ does introduce a notable dilemma when treating completely evaporating sprays which motivates the application of surface-weighted statistics, for which a comprehensive justification follows in Section 5.1. The study of surface-weighted moment-equations within the PGM hierarchy of models was first performed by Marchildon [61]. Designed to provide closed-form expressions and reduce the non-linearity of moments taken of

the RHS of Equation (4.8), surface-weighting of the set of generating weights was demonstrated to provide well-posed and strictly-hyperbolic moment-equations for a surface-based polydisperse phase density.

The definition of surface-weighted conserved moments of the DDF is obtained by pre-multiplying the previously considered set of generating weights, $\boldsymbol{\mathcal{W}}$, by the surface. Where droplets are assumed spherical, $s = \pi d^2$, the set of surface-weighted generating weights thus becomes

$$\bar{\boldsymbol{\mathcal{W}}} = (\pi d^2) \cdot \begin{bmatrix} 1 & v_i & \ln(d) & T & v_i v_j & \ln(d)^2 & T^2 & v_i \ln(d) & v_i T & \ln(d) T \end{bmatrix}^{\mathrm{T}} . \tag{5.12}$$

Given the distribution function, $\tilde{G}$, the resulting set of spacetime-coupled partial differential equations (PDEs) of the surface-weighted two-scalar PGM for evaporating sprays, in balance-law form, becomes

$$\frac{\partial \bar{s}}{\partial t} + \frac{\partial}{\partial x_\alpha} \bar{s}\bar{u}_\alpha = \bar{S}^{(0)} , \tag{5.13}$$

$$\frac{\partial}{\partial t} \bar{s}\bar{u}_i + \frac{\partial}{\partial x_\alpha} \bar{s}\big(\Psi_{i\alpha} + \bar{u}_i\bar{u}_\alpha\big) = \bar{S}_i^{(1)} , \tag{5.14}$$

$$\frac{\partial}{\partial t} \bar{s}\bar{\mu} + \frac{\partial}{\partial x_\alpha} \bar{s}\left(\Psi_{\alpha d} + \bar{u}_\alpha\bar{\mu}\right) = \bar{S}_d^{(2)} , \tag{5.15}$$

$$\frac{\partial}{\partial t} \bar{s}\bar{\theta} + \frac{\partial}{\partial x_\alpha} \bar{s}\left(\Psi_{\alpha T} + \bar{u}_\alpha\bar{\theta}\right) = \bar{S}_T^{(3)} , \tag{5.16}$$

$$\frac{\partial}{\partial t} \bar{s}\left(\Psi_{ij} + \bar{u}_i\bar{u}_j\right) + \frac{\partial}{\partial x_\alpha} \bar{s}\left(\bar{u}_i\Psi_{j\alpha} + \bar{u}_j\Psi_{i\alpha} + \bar{u}_\alpha\Psi_{ij} + \bar{u}_i\bar{u}_j\bar{u}_\alpha\right) = \bar{S}_{ij}^{(4)} , \tag{5.17}$$

$$\frac{\partial}{\partial t} \bar{s}\big(\Psi_{dd} + \bar{\mu}^2\big) + \frac{\partial}{\partial x_\alpha} \bar{s}\left(\bar{u}_\alpha\Psi_{dd} + 2\bar{\mu}\Psi_{\alpha d} + \bar{u}_\alpha\bar{\mu}^2\right) = \bar{S}_{dd}^{(5)} , \tag{5.18}$$

$$\frac{\partial}{\partial t} \bar{s}\big(\Psi_{TT} + \bar{\theta}^2\big) + \frac{\partial}{\partial x_\alpha} \bar{s}\left(\bar{u}_\alpha\Psi_{TT} + 2\bar{\theta}\Psi_{\alpha T} + \bar{u}_\alpha\bar{\theta}^2\right) = \bar{S}_{TT}^{(6)} , \tag{5.19}$$

$$\frac{\partial}{\partial t} \bar{s}\big(\Psi_{id} + \bar{u}_i\bar{\mu}\big) + \frac{\partial}{\partial x_\alpha} \bar{s}\left(\bar{u}_i\Psi_{\alpha d} + \bar{u}_\alpha\Psi_{id} + \bar{\mu}\Psi_{i\alpha} + \bar{u}_i\bar{u}_\alpha\bar{\mu}\right) = \bar{S}_{id}^{(7)} , \tag{5.20}$$

$$\frac{\partial}{\partial t} \bar{s}\big(\Psi_{iT} + \bar{u}_i\bar{\theta}\big) + \frac{\partial}{\partial x_\alpha} \bar{s}\left(\bar{u}_i\Psi_{\alpha T} + \bar{u}_\alpha\Psi_{iT} + \bar{\theta}\Psi_{i\alpha} + \bar{u}_i\bar{u}_\alpha\bar{\theta}\right) = \bar{S}_{iT}^{(8)} , \tag{5.21}$$

$$\frac{\partial}{\partial t} \bar{s}\big(\Psi_{dT} + \bar{\mu}\bar{\theta}\big) + \frac{\partial}{\partial x_\alpha} \bar{s}\left(\bar{u}_\alpha\Psi_{dT} + \bar{\mu}\Psi_{\alpha T} + \bar{\theta}\Psi_{\alpha d} + \bar{u}_\alpha\bar{\mu}\bar{\theta}\right) = \bar{S}_{dT}^{(9)} . \tag{5.22}$$

Table 5.1: Summary of surface-weighted moments in canonical form.

Name	Weight	Moment	Expression
Surface Density	s	$\bar{s}$	$n\sigma$
Average Surface	s/n	σ	$\pi\ \exp(2(\Psi_{dd}+\mu))$
Weighted Average Velocity	$v_i/\bar{s}$	$\bar{u}_i$	$u_i + 2\Psi_{id}$
Weighted Average $\ln(d)$	$\ln(d)/\bar{s}$	$\bar{\mu}$	$\mu + 2\Psi_{dd}$
Weighted Average Temperature	$T/\bar{s}$	$\bar{\theta}$	$\theta + 2\Psi_{dT}$
Velocity Variance	$c_i c_j/\bar{s}$	Ψ_{ij}	–
$\ln(d)$ Variance	$c_d^2/\bar{s}$	Ψ_{dd}	–
Temperature Variance	$c_T^2/\bar{s}$	Ψ_{TT}	–
Velocity-$\ln(d)$ Co-variance	$c_i c_d/\bar{s}$	Ψ_{id}	–
Velocity-Temperature Co-variance	$c_i c_T/\bar{s}$	Ψ_{iT}	–
$\ln(d)$-Temperature Co-variance	$c_d c_T/\bar{s}$	Ψ_{dT}	–

A summary of the various canonical variable definitions is provided in Table 5.1. Notice, the lowest-order moment has becomes the surface-density, $\bar{s} = \pi n \exp(2\mu)$ which is often described in spray-modelling. Likewise, from this point onwards, the bar notation is adopted to differentiate surface-weighted quantities from their unweighted counterparts. Regarding the equations, their interpretation remains intuitive. Specifically, Equation (5.13) is a continuity equation for the surface density of the droplets. Equations (5.14) to (5.16) are five equations which describe the evolution of the first-order moments: three equations for the velocity density vector, one equation for the logarithmic size density and a last for the temperature density—all of which are surface-weighted. Equations (5.17) to (5.22) are fifteen equations which described the evolution of the second-order weighted moments which consists of six equations for the three-by-three symmetric velocity variance-covariance tensor, two equations for the variance of size and temperature, and seven equations for the covariance between velocity, size and temperature. As a result, the two-scalar surface-weighted PGM yields a set of twenty-one coupled moment-equations. In the above equations, the right-hand side terms, $\bar{S}_{\tilde{i}\tilde{j}}$, result from the integration of the various fields describing gas-droplet coupling and various thermodynamic processes such as vaporization. A comprehensive derivation of these expressions follows in Chapter 6. Further, while surface-weighting

has introduced significantly increased coupling between moments, i.e., all equations are coupled to the size-related moments, the first-order structure of the PGM hierarchy is conserved, along with the strict-hyperbolicity of the generalized formulation—which will be demonstrated in Section 5.2.

5.1 Surface-Weighted Moment-Equations

The investigations performed by Marchildon regarding surface-weighted moment-equations were specifically concerned with the linearization of relaxation coefficients within the source term of their proposed surface-based one-scalar PGM [61]. Therein, a logarithmic transformation of the size-space was not performed, whereby particles were assumed to exhibit a normal surface distribution. As a result, moments were obtained by truncated integration of the underlying phase-space density distribution function which namely admitted a realizable phase-density who's most likely surface was a non-positive real number. While non-physical, such a formulation avoided mathematical artifacts within the moment-equations when treating a completely evaporating particle phase. Rather, the mathematical artifacts discovered herein in the treatment of evaporating sprays is uniquely encountered using the logarithm-based formulation originally proposed by Forgues *et al.*, as briefly discussed above in Chapter 5. Namely, as the logarithmic mapping stretches $\{0:1\} \rightarrow \{-\infty:0\}$, a singularity is introduced in the moment-equations as droplets undergo evaporation. To demonstrate, two analyses are performed. The first providing a rigorous proof of the ill-behaved nature of the logarithm-based moment-equations using a simplified monodispersed droplet-size distribution function, followed by the demonstration of the corrective effect of surface-weighted statistics. The second argues by extension to a polydispersed natural log-normal droplet-size distribution function through numerical integration of both unweighted and weighted sets of moment-equations, and comparison against a Monte-Carlo solution of the underlying discrete droplet evolution.

5.1.1 Analysis of a Strictly-Monodisperse Logarithm-Based Evaporating Size Distribution

Consider the following reduced droplet-size distribution function (SDF),

$$\mathcal{F} = \mathcal{F}(\ln(d), t)\,, \tag{5.23}$$

which solely describes a statistical distribution of the natural logarithm of diameter of an arbitrary droplet phase. The corresponding space-homogeneous kinetic equation governing the evolution of the proposed SDF becomes

$$\frac{\partial \mathcal{F}}{\partial t} = -\frac{\partial}{\partial d}\left(\Upsilon_d \mathcal{F}\right)\,. \tag{5.24}$$

Assuming the strict-monodispersity of $\mathcal{F}$, the set, $\boldsymbol{\mathcal{W}} = [1\ \ln(d)]^{\mathrm{T}}$, is sufficient to produce a fully-defined set of moments, $\boldsymbol{U} = [n\ n\mu]^{\mathrm{T}}$, where μ is the mean of the logarithm-based distribution. To close the system of partial differential moment-equations,

$$\frac{\partial \langle \boldsymbol{\mathcal{W}}\, \mathcal{F}\rangle}{\partial t} = -\left\langle \boldsymbol{\mathcal{W}} \frac{\partial}{\partial \ln(d)}\left(\frac{\Upsilon_d}{d}\mathcal{F}\right)\right\rangle\,, \tag{5.25}$$

the droplet-size distribution function is chosen as a Dirac delta centered about the mean,

$$\mathcal{F} = n\,\delta(\ln(d) - \mu)\,. \tag{5.26}$$

For the purpose of simple demonstration, a rudimentary expression for the time-rate of change of droplet diameter, $\Upsilon_d = \mathrm{d}d/\mathrm{d}t$, can be obtained by consideration of the well-known d^2-law, the simplest evaporation law cited in the literature [4, 14, 21, 37, 55, 87, 93]. Describing a particle undergoing complete evaporation, the d^2-law is simply

$$\frac{\mathrm{d}d^2}{\mathrm{d}t} = -\alpha\,, \tag{5.27}$$

$$\Upsilon_d = \frac{\mathrm{d}d}{\mathrm{d}t} = -\frac{\alpha}{2d}\,. \tag{5.28}$$

Integrating the system of moment-equations (5.25) yields a system of two coupled ordinary differential equations (ODEs),

$$\frac{\mathrm{d}n}{\mathrm{d}t} = 0\,, \tag{5.29}$$

$$\frac{\mathrm{d}}{\mathrm{d}t}(n\mu) = -\frac{1}{2}\alpha\, n \exp(-2\mu)\,. \tag{5.30}$$

The exact analytical solution to the initial value problem, $[n(0) = n_0, \mu(0) = \mu_0]$, is trivially obtained as

$$n(t) = n_0\,, \tag{5.31}$$

$$n\mu(t) = \frac{n_0}{2}\,\ln(\exp(2\mu_0) - \alpha\, t)\,. \tag{5.32}$$

By simple inspection of Equation (5.32), one remarks an infinite discontinuity at $t = \exp(2\mu_0)/\alpha$—the system of moment-equations becomes undefined. The existence of this singularity is well-understood, however, and inherently expected. Given the logarithmic transformation, droplets evaporate towards zero size but never reach singularity. As a result, number density is conserved despite evaporation, and the size density, $n\mu$, tends toward negative infinity as droplets become infinitely small. In reality, number density is not expected to be conserved within the evaporating spray—neglecting non-evaporating impurities contained within the droplets, i.e., non-volatile contents. Consequently, a sink of number density within the moment-equations is required to control the divergence of the moments.

A sink of number density may be introduced by reformulating the system of moment-equations using surface-weighted moments, such that, as droplets become infinitely small (i.e. zero surface), their weighted contribution to the moment-equations also becomes infinitely small. Precisely, the surface-weighted conserved moments for the SDF considered above is obtained by pre-multiplying the previously considered set of generating weights, $\boldsymbol{\mathcal{W}}$, by the surface. Where droplets are assumed spherical, $s = \pi d^2$, the set of surface-weighted generating weights thus becomes $\bar{\boldsymbol{\mathcal{W}}} = (\pi\, d^2)\cdot[1\ \ln(d)]^{\mathrm{T}}$, and the set of conserved moments becomes $\bar{\boldsymbol{U}} = [\bar{s}\ \bar{s}\mu]^{\mathrm{T}}$. Substituting for $\bar{\boldsymbol{\mathcal{W}}}$ in Equation (5.25), the resulting system of surface-weighted moment-ODEs becomes

$$\frac{\mathrm{d}\bar{s}}{\mathrm{d}t} = \frac{\mathrm{d}}{\mathrm{d}t}(\pi n \exp(2\mu)) = -\alpha\pi n\,, \tag{5.33}$$

$$\frac{\mathrm{d}}{\mathrm{d}t}(\bar{s}\mu) = -\frac{1}{2}\alpha\, n(2\mu+1)\,. \tag{5.34}$$

Similarly, the exact solution to the initial value problem, $[n(0) = n_0, \mu(0) = \mu_0]$, is trivially obtained. When expressed in terms of the unweighted conserved moments, it is

$$n(t) = n_0\, \exp(-\alpha\,\pi\,t)\,, \tag{5.35}$$

$$n\mu(t) = \frac{1}{2} n_0\, \exp(-\alpha\,\pi\,t)\,(2\mu_0 - \alpha\,\pi\,t)\,. \tag{5.36}$$

As expected, a sink of number density is obtained in Equation (5.35). Likewise, Equation (5.36) exhibits no undefined behaviour, as opposed to Equation (5.32), and is a continuous real-valued function. In fact, the size density, $n\mu$, of Equation (5.36) is continuous, well-defined, and, by inspection of L'Hopital's rule, is shown to asymptote to zero as t increases without bound,

$$\begin{aligned}
\lim_{t\to\infty} n\mu &= \lim_{t\to\infty} -\frac{1}{2}\cdot\frac{n_0\,(2\mu_0 - \alpha\,\pi\,t)}{\exp(\alpha\,\pi\,t)}\,,\\
&= \lim_{t\to\infty} -\frac{1}{2}\cdot\frac{\frac{\partial}{\partial t}\left(n_0\,(2\mu_0 - \alpha\,\pi\,t)\right)}{\frac{\partial}{\partial t}\left(\exp(\alpha\,\pi\,t)\right)}\,,\\
&= \lim_{t\to\infty} \frac{1}{2}\frac{n_0}{\exp(\alpha\,\pi\,t)}\,,\\
&= 0\,.
\end{aligned} \tag{5.37}$$

Interestingly, where a monodisperse collection of droplets evaporate to zero size, the number density, while not constant, should behave as a step function, i.e., all droplets reach singularity at once and a discontinuous loss of droplets is expected. The solution obtained in Equation (5.35) does not recover this behaviour and instead describes a continuous exponential loss of number density. However, where a polydisperse collection of droplets is considered, a continuous loss of number density is expected, assuming the underlying SDF is itself continuous. Consequently, the proposed surface-weighted moment model is expected to better recover the situation of polydisperse droplet distribution functions.

5.1.2 Analysis of a Polydisperse Logarithm-Based Evaporating Size Distribution

The demonstration performed within Section 5.1.1 extends to the polydisperse droplet-size distribution function. Where one assumes the natural logarithm-based SDF, $\mathcal{F}$, is polydisperse, the maximum-entropy moment-closure of Equation (5.25) yields

$$\mathcal{F} = \frac{n}{d\sqrt{2\pi\Psi_{dd}}} \exp\left(-\frac{1}{2}\Psi_{dd}^{-1}\left(\ln(d)-\mu\right)^2\right), \tag{5.38}$$

for a set of generating weights $\boldsymbol{W} = \left[1 \;\; \ln(d) \;\; \ln(d)^2\right]^{\mathrm{T}}$. The systems of equations for both the unweighted and surface-weighted formulations, respectively, become

$$\boldsymbol{\mathcal{W}} = \left[1 \;\; \ln(d) \;\; \ln(d)^2\right]^{\mathrm{T}} :$$

$$\frac{\mathrm{d}n}{\mathrm{d}t} = 0\,, \tag{5.39}$$

$$\frac{\mathrm{d}}{\mathrm{d}t}(n\mu) = -\frac{1}{2}\,\alpha\, n\, \exp(2(\Psi_{dd}-\mu))\,, \tag{5.40}$$

$$\frac{\mathrm{d}}{\mathrm{d}t}(n(\Psi_{dd}+\mu^2)) = 2\alpha\, n\, \exp(2(\Psi_{dd}-\mu))(\mu - 2\Psi_{dd})\,. \tag{5.41}$$

$$\bar{\boldsymbol{\mathcal{W}}} = (\pi\, d^2)\cdot\left[1 \;\; \ln(d) \;\; \ln(d)^2\right]^{\mathrm{T}} :$$

$$\frac{\mathrm{d}\bar{s}}{\mathrm{d}t} = -\alpha\,\pi\, n\,, \tag{5.42}$$

$$\frac{\mathrm{d}}{\mathrm{d}t}(\bar{s}\bar{\mu}) = -\frac{1}{2}\,\alpha\,\pi\, n(1+2\mu)\,, \tag{5.43}$$

$$\frac{\mathrm{d}}{\mathrm{d}t}(\bar{s}(\Psi_{dd}+\bar{\mu}^2)) = -\alpha\,\pi\, n(\mu+\mu^2+\Psi_{dd})\,. \tag{5.44}$$

By expansion using the chain-rule, the surface-weighted moment-equations can be expressed in terms of the unweighted conserved moments,

$$\bar{\boldsymbol{\mathcal{W}}} = (\pi\, d^2) \cdot \left[1 \;\; \ln(d) \;\; \ln(d)^2\right]^{\mathrm{T}} \; :$$

$$\frac{\mathrm{d}n}{\mathrm{d}t} = -8\alpha\, n \exp\left(-2(\Psi_{dd} + \mu)\right)\Psi_{dd}^2 \,, \tag{5.45}$$

$$\frac{\mathrm{d}}{\mathrm{d}t}(n\mu) = -\alpha\, n \exp\left(-2(\Psi_{dd} + \mu)\right)\left(\frac{1}{2} + 2\Psi_{dd} + (\mu - 1)\,\Psi_{dd}^2\right) \,, \tag{5.46}$$

$$\begin{aligned}\frac{\mathrm{d}}{\mathrm{d}t}(n(\Psi_{dd} + \mu^2)) = &-\alpha\, n \exp\left(-2(\Psi_{dd} + \mu)\right) \\ &\left(\mu + 4\left(\mu - \frac{1}{2}\right)\Psi_{dd} + 8\left(\mu^2 - 2\mu + \frac{1}{2}\right)\Psi_{dd}^2 + 8\Psi_{dd}^3\right) \,.\end{aligned} \tag{5.47}$$

Again, a sink of number density is obtained by applying a surface-weighted formulation to the moment-equations, as is shown in Equation (5.45). The strong coupling and strong non-linearity of these systems of ODEs renders their analytical solution significantly more difficult as compared to the previous considered strictly-monodisperse analysis. However, the behaviours of these ODEs may be easily investigated by numerical integration using a rudimentary higher-order Runge-Kutta time-marching method.

To this end, two exemplary initial-value problems are numerically integrated using the well-known Runge-Kutta 4^{th}-order explicit time-marching scheme. Further, to provide a quantitative assessment of the moment-approximation, a Monte-Carlo solution to the underlying discrete particle evolution shall be integrated. Comparative moments of a Monte-Carlo solution can be obtained by evaluating the moments of the discrete-droplet distribution using the discrete traditional definition of statistical moments. Where an initial number density of n_0 is considered and m_0 droplets are initially sampled, the unweighted

conserved moments of the discrete-droplet distribution are

$$n = n_0 \frac{m}{m_0}\,, \tag{5.48}$$

$$n\mu = n_0 \frac{\sum_{i=1}^{m} \ln(d_i)}{m_0}\,, \tag{5.49}$$

$$n(\Psi_{dd} + \mu^2) = n_0 \frac{\sum_{i=1}^{m} \left(\ln(d_i)\right)^2}{m_0}\,, \tag{5.50}$$

with m the number of sampled droplets with a non-zero size. Initialization of the Monte-Carlo solution is performed by sampling the initial droplet distribution function, $\mathcal{F}_0$, using a Mersenne-twister pseudo-random number generator algorithm [64], while the evolution of the discrete evaporating droplet distribution is described by the d^2-law from Equation (5.28). In both cases considered below, a d^2-law constant evaporation rate of $\alpha = 0.9 \times 10^{-6}\,\mathrm{m^2\,s^{-1}}$ for kerosene is considered [119], with initial $n_0 = 1 \times 10^6\,\mathrm{m^{-3}}$ droplets of geometric mean diameter $e^{\mu_0} = 0.75\,\mathrm{mm}$. Regarding the numerical scheme, over-resolution of the problem is guaranteed by a fixed-step size of $\mathrm{dt} = 1 \times 10^{-6}\,\mathrm{s}$ until a final time $t_f = 1.05\,\mathrm{s}$—barring an observed discontinuity within the solution.

As a first analysis, consider the monodisperse realizability limit of the proposed SDF, $\mathcal{F}$, where the initial size-variance, Ψ_{dd_0}, is near zero. Of course, the size-variance may not be taken as zero as $\mathcal{F}$ would otherwise be unrealizable. Consequently, the initial size-variance for the quasi-monodisperse analysis presented in Figure 5.2, is taken as $\Psi_{dd_0} = 1 \times 10^{-7}$. Note, results illustrated in the subsequent figures are presented as non-dimensional quantities normalized using the initial condition. As predicted by the initial monodisperse analysis of Section 5.1.1, an infinite discontinuity within the unweighted moment-equations is observed which is in agreement with its expected approximate non-dimensional time $\exp(2\mu_0)/(t_f\,\alpha) \approx 0.595$. In particular, the unweighted moment-equations fail to capture the abrupt loss of droplets due to the quasi-instantaneous evaporation of droplets which all simultaneously reach zero size, as shown in Figure 5.2(a). As for the first-order moment in Figure 5.2(b), one observes an initial exponential increase of size density. This increase is explained by the increasingly negative mean natural logarithm of diameter, as again, $d \to 0 : ln(d) \to -\infty$. However, due to loss of droplets, the exponential growth of the size density is controlled in both the surface-weighted moment-equation and Monte-Carlo

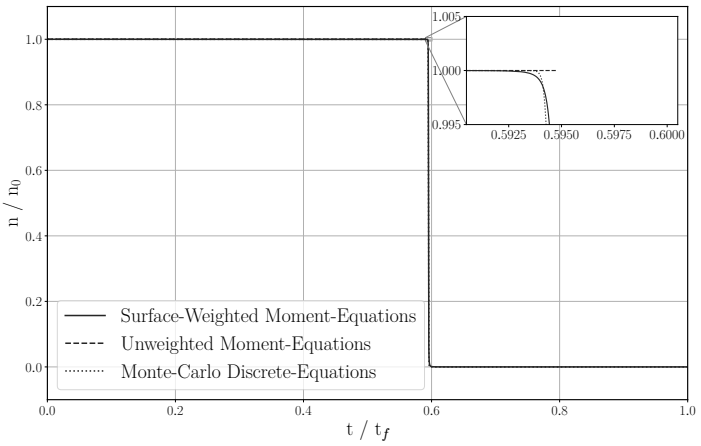

(a) Non-dimensional number density.

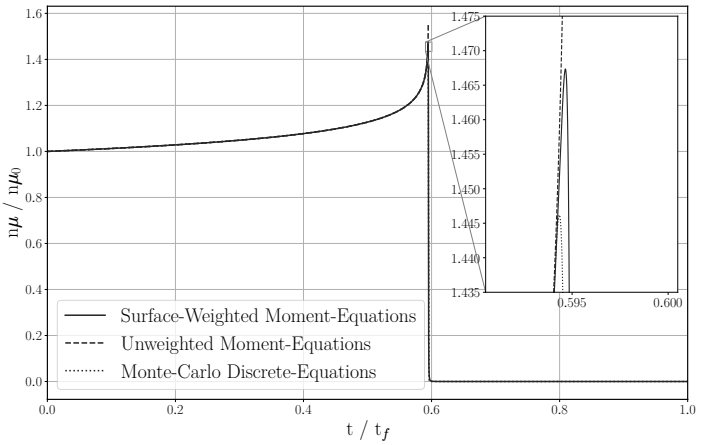

(b) Non-dimensional size density.

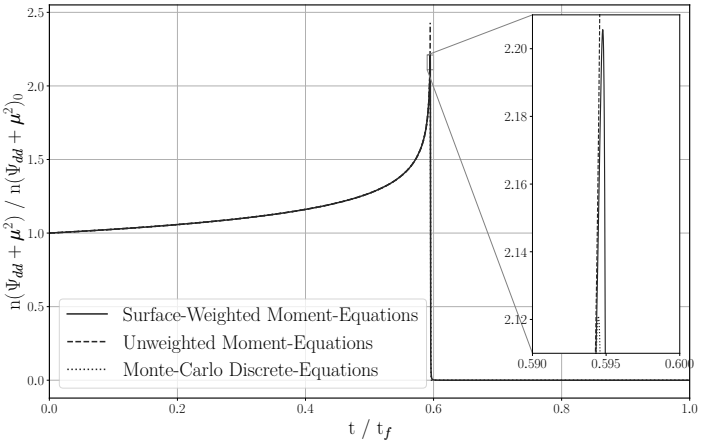

(c) Non-dimensional size-variance density.

Figure 5.2: Moment evolution of an initially lognormal quasi-monodisperse droplet-size distribution undergoing evaporation.

discrete-equation solutions while the unweighted moment-equation solution conversely diverges and becomes undefined. A similar behaviour is observed regarding the second-order size-variance density plot of Figure 5.2(c). Regarding the agreement between both the surface-weighted moment-equations and Monte-Carlo discrete-equations, good agreement is observed, whereby the quasi-discontinuity is properly captured by the surface-weighted moment-equations in the quasi-monodisperse limit. Rather, given the initial small non-zero size-variance, all moments of Figure 5.2 are expected to behave as continuous functions. However, in the absolute monodispserse limit, the Monte-Carlo discrete-equations can admit a discontinuity while the surface-weighted moment-equations become undefined due to the realizability limit of underlying distribution function.

A second analysis is performed for an initially polydisperse droplet-size distribution—as illustrated in Figure 5.3. Particularly, the initial size-variance is increased to introduce a continuous distribution of droplet sizes, with $\Psi_{dd_0} = 0.01$. Again, the unweighted moment-equations possess an infinite discontinuity, while the surface-weighted moment-equations remain physical and recover the behaviour of the Monte-Carlo discrete-equations solution. Notably however, a greater disagreement between the surface-weighted moment-equations and Monte-Carlo equations is observed for all quantities in Figures 5.3(a) to 5.3(c). The disagreement is well-understood herein however, and is a result of the underlying moment-closure. Where the initial conditions is described by a lognormal size distribution, there is no inherent guarantee that Υ_d will conserve the lognormal size distribution of the collection of discrete-droplets. Conversely, moment-equations are restricted in their behaviour such that the inherent nature of the assumed underlying distribution function is respected. As a result, the moments described by the surface-weighted moment-equations must remain within the realizable-space of the underlying distribution function, while no such restriction would physically be imposed in reality which can result in notable disagreement between moment-based solutions and discrete Lagrangian-based solutions. A further discussion on these matters follows in Chapter 8 within the scope of the two-scalar PGM moment approximation for sprays undergoing evaporation. Nevertheless, the analyses presented herein provide a complete and comprehensive argument for the necessity of surface-weighted moment-equations for logarithm-based size distributions within the PGM hierarchy of models. Rather, the consideration of surface-weighted statistics have been

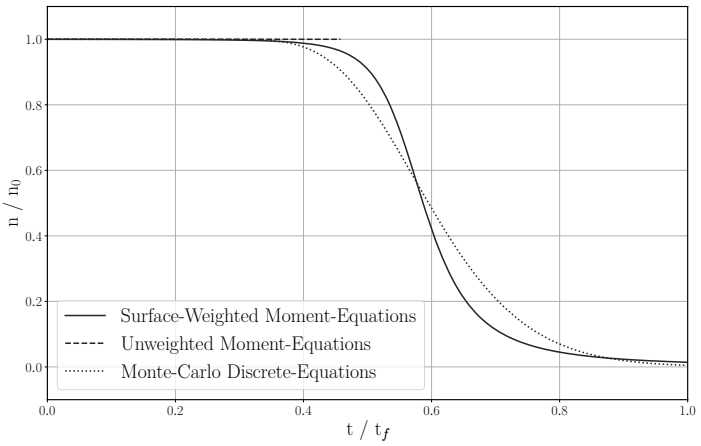

(a) Non-dimensional number density.

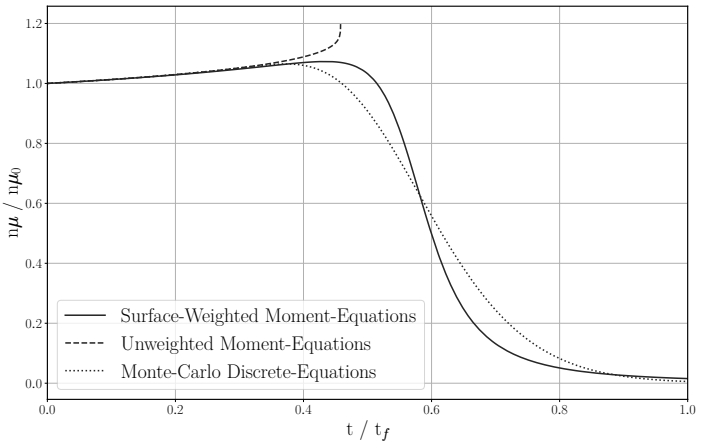

(b) Non-dimensional size density.

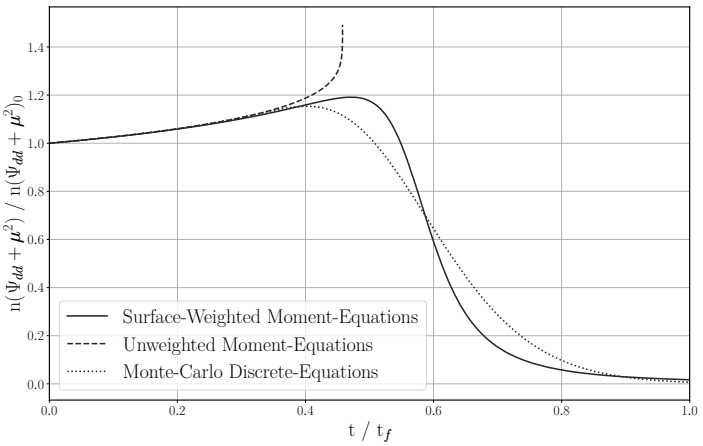

(c) Non-dimensional size-variance density.

Figure 5.3: Moment evolution of an initially lognormal polydisperse droplet-size distribution undergoing evaporation.

demonstrated to yield well-behaved sets of equations which recover solutions obtained using a comparative Lagrangian-type Monte-Carlo method for evaporating droplet sprays—while the instability, ill-behaved and undefined moment-equations of the unweighted PGM formulation have been rigorously shown to be erroneous.

5.2 Hyperbolicity and Eigenvalues of the Surface-Weighted Moment-Equations

The robust hyperbolicity of the proposed surface-weighted moment-equations was first demonstrated by Marchildon [61]. The demonstration of strict-hyperbolicity of these equations follows the argument presented in Section 3.4. Where the DDF, $\tilde{\mathcal{G}}$, remains unmodified by the surface-weighting, the surface-weighted density and flux potentials are obtained by pre-multiplying $\tilde{\mathcal{G}}$ by the surface, such that,

$$\bar{h}(\boldsymbol{\alpha}) = \left\langle s\, \tilde{\mathcal{G}} \right\rangle = \left\langle s\, e^{\boldsymbol{\alpha}^{\mathbf{T}}\boldsymbol{\mathcal{W}}} \right\rangle , \tag{5.51}$$

$$\bar{f}_i(\boldsymbol{\alpha}) = \left\langle s\, v_i \tilde{\mathcal{G}} \right\rangle = \left\langle s\, v_i e^{\boldsymbol{\alpha}^{\mathbf{T}}\boldsymbol{\mathcal{W}}} \right\rangle . \tag{5.52}$$

Both the surface-weighted conserved moment vector, $\bar{\boldsymbol{U}}$, and associated surface-weighted flux dyad, $\bar{\boldsymbol{F}}$, follow as

$$\bar{\boldsymbol{U}} = \frac{\partial \bar{h}(\boldsymbol{\alpha})}{\partial \boldsymbol{\alpha}} = \left\langle s\, \boldsymbol{\mathcal{W}}\, e^{\boldsymbol{\alpha}^{\mathbf{T}}\boldsymbol{\mathcal{W}}} \right\rangle , \tag{5.53}$$

$$\bar{\boldsymbol{F}} = \frac{\partial \bar{f}_i(\boldsymbol{\alpha})}{\partial \boldsymbol{\alpha}} = \left\langle s\, \boldsymbol{\mathcal{W}}\, v_i e^{\boldsymbol{\alpha}^{\mathbf{T}}\boldsymbol{\mathcal{W}}} \right\rangle . \tag{5.54}$$

The surface-weighted flux Jacobian, $\partial\bar{\boldsymbol{F}}/\partial\bar{\boldsymbol{U}}$, may then be obtained by further differentiating both Equations (5.53) and (5.54),

$$\frac{\partial \bar{\boldsymbol{U}}}{\partial \boldsymbol{\alpha}} = \frac{\partial \bar{h}(\boldsymbol{\alpha})}{\partial \boldsymbol{\alpha}\partial \boldsymbol{\alpha}} = \left\langle s\, \boldsymbol{\mathcal{W}}\boldsymbol{\mathcal{W}}^{\mathrm{T}}\, e^{\boldsymbol{\alpha}^{\mathbf{T}}\boldsymbol{\mathcal{W}}} \right\rangle , \tag{5.55}$$

$$\frac{\partial \bar{\boldsymbol{F}}}{\partial \boldsymbol{\alpha}} = \frac{\partial \bar{f}_i(\boldsymbol{\alpha})}{\partial \boldsymbol{\alpha}\partial \boldsymbol{\alpha}} = \left\langle s\, \boldsymbol{\mathcal{W}}\boldsymbol{\mathcal{W}}^{\mathrm{T}}\, v_i e^{\boldsymbol{\alpha}^{\mathbf{T}}\boldsymbol{\mathcal{W}}} \right\rangle , \tag{5.56}$$

such that,

$$\frac{\partial \bar{\boldsymbol{F}}}{\partial \bar{\boldsymbol{U}}} = \left(\frac{\partial \bar{\boldsymbol{U}}}{\partial \boldsymbol{\alpha}}\right)^{-1} \frac{\partial \bar{\boldsymbol{F}}}{\partial \boldsymbol{\alpha}} = \left(\frac{\partial \bar{h}(\boldsymbol{\alpha})}{\partial \boldsymbol{\alpha}\partial \boldsymbol{\alpha}}\right)^{-1} \frac{\partial \bar{f}_i(\boldsymbol{\alpha})}{\partial \boldsymbol{\alpha}\partial \boldsymbol{\alpha}} \,. \tag{5.57}$$

Again, the hyperbolicity of the system of moment-equations is guaranteed provided that $\left\langle s\, \boldsymbol{\mathcal{W}}\boldsymbol{\mathcal{W}}^{\mathrm{T}}\, e^{\boldsymbol{\alpha}^{\mathrm{T}}\boldsymbol{\mathcal{W}}} \right\rangle$ is non-singular and symmetric positive-definite. As the surface, s, is guaranteed a strictly positive number, then by extension to the previous maximum-entropy hyperbolicity argument, $\partial \bar{\boldsymbol{U}}/\partial \boldsymbol{\alpha}$, is a strictly convex positive-definite and the hyperbolicity of the moment-equations is guaranteed.

Furthermore, the hyperbolicity of the surface-weighted system of equations can be verified by examining the Eigenvalues of the proposed surface-weighted equations. For the one-dimensional case, the system of Equations (5.13) to (5.22) reduces to a system of ten coupled partial differential equations,

$$\frac{\partial \bar{s}}{\partial t} + \frac{\partial}{\partial x}\, \bar{s}\bar{u}_x = \bar{S}^{(0)} \,, \tag{5.58}$$

$$\frac{\partial}{\partial t}\, \bar{s}\bar{u}_x + \frac{\partial}{\partial x}\, \bar{s}(\Psi_{ix} + \bar{u}_x{}^2) = \bar{S}^{(1)}_x \,, \tag{5.59}$$

$$\frac{\partial}{\partial t}\bar{s}\bar{\mu} + \frac{\partial}{\partial x}\, \bar{s}\,(\Psi_{xd} + \bar{u}_x\bar{\mu}) = \bar{S}^{(2)}_d \,, \tag{5.60}$$

$$\frac{\partial}{\partial t}\bar{s}\bar{\theta} + \frac{\partial}{\partial x}\, \bar{s}\left(\Psi_{xT} + \bar{u}_x\bar{\theta}\right) = \bar{S}^{(3)}_T \,, \tag{5.61}$$

$$\frac{\partial}{\partial t}\, \bar{s}\left(\Psi_{xx} + \bar{u}_x{}^2\right) + \frac{\partial}{\partial x}\, \bar{s}\left(3\bar{u}_x\Psi_{xx} + \bar{u}_x{}^3\right) = \bar{S}^{(4)}_{xx} \,, \tag{5.62}$$

$$\frac{\partial}{\partial t}\, \bar{s}(\Psi_{dd} + \bar{\mu}^2) + \frac{\partial}{\partial x}\, \bar{s}\left(\bar{u}_x\Psi_{dd} + 2\bar{\mu}\Psi_{xd} + \bar{u}_x\bar{\mu}^2\right) = \bar{S}^{(5)}_{dd} \,, \tag{5.63}$$

$$\frac{\partial}{\partial t}\, \bar{s}(\Psi_{TT} + \bar{\theta}^2) + \frac{\partial}{\partial x}\, \bar{s}\left(\bar{u}_x\Psi_{TT} + 2\bar{\theta}\Psi_{xT} + \bar{u}_x\bar{\theta}^2\right) = \bar{S}^{(6)}_{TT} \,, \tag{5.64}$$

$$\frac{\partial}{\partial t}\bar{s}(\Psi_{xd} + \bar{u}_x\bar{\mu}) + \frac{\partial}{\partial x}\, \bar{s}\left(2\bar{u}_x\Psi_{xd} + \bar{\mu}\Psi_{xx} + \bar{u}_x{}^2\bar{\mu}\right) = \bar{S}^{(7)}_{xd} \,, \tag{5.65}$$

$$\frac{\partial}{\partial t}\bar{s}(\Psi_{xT} + \bar{u}_x\bar{\theta}) + \frac{\partial}{\partial x}\, \bar{s}\left(2\bar{u}_x\Psi_{xT} + \bar{\theta}\Psi_{xx} + \bar{u}_x{}^2\bar{\theta}\right) = \bar{S}^{(8)}_{xT} \,, \tag{5.66}$$

$$\frac{\partial}{\partial t}\bar{s}(\Psi_{dT} + \bar{\mu}\bar{\theta}) + \frac{\partial}{\partial x}\, \bar{s}\left(+\bar{u}_x\Psi_{dT} + \bar{\mu}\Psi_{xT} + \bar{\theta}\Psi_{xd} + \bar{u}_x\bar{\mu}\bar{\theta}\right) = \bar{S}^{(9)}_{dT} \,. \tag{5.67}$$

For the above equations, the surface-weighted flux Jacobian, $\partial\bar{\boldsymbol{F}}/\partial\bar{\boldsymbol{U}}$, is

$$\begin{bmatrix}
u_x & n & 0 & 0 & 0 & 4n\Psi_{xd} & 0 & 0 & 0 & 0 \\
\frac{\Psi_{xx}}{n} & u_x & 0 & 0 & 1 & -2\Psi_{xx} & 0 & -4\Psi_{xd} & 0 & 0 \\
\frac{\Psi_{xd}}{n} & 0 & u_x & 0 & 0 & -6\Psi_{xd} & 0 & 1 & 0 & 0 \\
\frac{\Psi_{xT}}{n} & 0 & 0 & u_x & 0 & -2\Psi_{xT} & 0 & 0 & 1 & -4\Psi_{xd} \\
0 & 2\Psi_{xx} & 0 & 0 & u_x + 2\Psi_{xd} & 0 & 0 & 4\Psi_{xx} & 0 & 0 \\
0 & 0 & 2\Psi_{xd} & 0 & 0 & u_x + 6\Psi_{xd} & 0 & 0 & 0 & 0 \\
0 & 0 & 0 & 2\Psi_{xT} & 0 & 0 & u_x + 2\Psi_{xd} & 0 & 0 & 4\Psi_{xT} \\
0 & \Psi_{xd} & \Psi_{xx} & 0 & 0 & 2\Psi_{xx} & 0 & u_x + 4\Psi_{xd} & 0 & 0 \\
0 & \Psi_{xT} & 0 & \Psi_{xx} & 0 & 0 & 0 & 2\Psi_{xT} & u_x + 2\Psi_{xd} & 2\Psi_{xx} \\
0 & 0 & \Psi_{xT} & \Psi_{xd} & 0 & 2\Psi_{xT} & 0 & 0 & 0 & u_x + 4\Psi_{xd}
\end{bmatrix}.$$

The Eigenvalues, i.e., the system wavespeeds, of the above matrix are determined by solving the roots of the characteristic equation for the Eigenvalue problem,

$$\begin{aligned}
\det\left(\frac{\partial\bar{\boldsymbol{F}}}{\partial\bar{\boldsymbol{U}}} - \lambda\boldsymbol{I}\right) = \left(u_x - \lambda + 2\Psi_{xd}\right)^4 \left(4\Psi_{xd}^2 + \left(4u_x - 4\lambda\right)\Psi_{xd} + u_x^2 - 2\lambda u_x + \lambda^2 - 3\Psi_{xx}\right) \\
\left(4\Psi_{xd}^2 + \left(4u_x - 4\lambda\right)\Psi_{xd} + u_x^2 - 2\lambda u_x + \lambda^2 - \Psi_{xx}\right)^2 . \qquad (5.68)
\end{aligned}$$

The ten Eigenvalues of the one-dimensional surface-weighted equations are then determined as

$$\lambda_{0,1} = u_x + 2\Psi_{xd} + \sqrt{3\Psi_{xx}}\,, \qquad (5.69)$$

$$\lambda_{2,3,4,5} = u_x + 2\Psi_{xd} + \sqrt{\Psi_{xx}}\,, \qquad (5.70)$$

$$\lambda_{6,7,8,9} = u_x + 2\Psi_{xd}\,. \qquad (5.71)$$

Where $\tilde{\mathcal{G}}$ is realizable, and the extended variance-covariance tensor, $\Psi_{\tilde{i}\tilde{j}}$, is symmetric positive-definite, one is guaranteed Ψ_{xx} is a strictly positive number. Consequently, the wavespeeds of the system of surface-weighted equations are guaranteed real-valued, and the proposed system is again verified robustly hyperbolic.

Chapter 6

Gas-Droplet Coupling of Evaporating Sprays

The evolution of evaporating sprays is complex. The underlying distribution of droplets is subjected to numerous intricate physical and thermodynamic processes which arise from gas-droplet and droplet-droplet coupling, of which a few notable examples include evaporation, coalescence, atomization, heat transfer and aerodynamic drag. In practice, the treatment of such processes for evaporating sprays has largely been achieved using Lagrangian-based discrete-droplet methods. However, the two-scalar PGM for evaporating sprays proposed within the present work introduces a novel Eulerian-based approach to spray modelling which is capable of capturing the complex gas-droplet and droplet-droplet interactions which dominate the behaviour of evaporating sprays.

Recalling from the formulation of the system of moment equations in balance law form from Section 3.2, the LHS of the system of Equations (3.15) represents the simple convective transport of the moments of the droplet distribution function. Therein, interactions between droplets and the gaseous carrier phase are not captured. Rather, such effects are treated within the as of yet largely ignored RHS of the system of Equations (5.13) to (5.22). Specifically, the RHS of the system of moment equations describes sources, or sinks, which act upon the macroscopic moments of the underlying droplet distribution. These terms arise from the treatment of fields which act upon the discrete droplets as described within

the RHS of the collisionless Williams-Boltzmann equation,

$$\frac{\partial \mathcal{F}}{\partial t} + v_\alpha \frac{\partial \mathcal{F}}{\partial x_\alpha} = -\frac{\partial}{\partial v_\alpha}\left(a_\alpha \mathcal{F}\right) - \frac{\partial}{\partial \ln(d)}\left(\frac{\Upsilon_d}{d}\mathcal{F}\right) - \frac{\partial}{\partial T}\left(\Upsilon_T \mathcal{F}\right) \ . \tag{5.3}$$

Expressions for the fields a_α, Υ_d, and Υ_T are derived from models for the aforementioned physical and thermodynamic processes which act upon the discrete droplets. As previously mentioned in Section 2.1, the considerations for inertial fields are uniquely limited to those of the steady-Stokes regime for irrotational droplets within the present work. However, formulations for the newly introduced size and temperature time rates of change, Υ_d, and Υ_T, respectively, are proposed herein for the treatment of evaporating sprays.

As such, the following chapter comprehensively elaborates upon the formulation of the RHS terms of the proposed two-scalar PGM for evaporating sprays. Content within the following sections includes both theoretical and numerical formulations for the mass and heat transfer gas-droplet coupling based upon classical monocomponent droplet evaporation theory, followed by a description of inertial gas-droplet coupling considerations, which namely includes a first-order, hyperbolicity maintaining, approximation to turbulent gas-droplet coupling.

6.1 Thermodynamic Gas-Droplet Coupling

The thermodynamic process of droplet evaporation in sprays is governed by the simultaneous transfer of both mass and heat between the gaseous carrier phase and droplet surface. During evaporation, mass transfer is controlled by the convective and diffusive transfer of droplet vapour, while heat transfer occurs primarily through both conductive and convective transfer at the gas-droplet interface [4, 55, 87], and in some cases, radiative heat transfer may also be considered but will largely be neglected herein. The theory of droplet evaporation has historically been a significant challenge, and numerous models of ranging complexity and applicability have been proposed. For instance, while the direct application of kinetic theory to the convective droplet mass transfer has been investigated [3, 44, 51, 52, 87–90], in most practical applications such convective effects are

largely ignored to due to the associated modelling complexities. While its consideration using the method of moments promises potential, it shall however remain beyond the scope of the present work. Instead, expressions describing the time rates of change of size and temperature, Υ_d, and Υ_T, respectively, due to evaporation can be simply obtained using traditional monocomponent droplet evaporation theory, or so-called hydrodynamic models of droplet evaporation [87], which are largely limited to the modelling of vapour diffusion.

As first mentioned in Section 5.1, the simplest droplet evaporation model cited in the literature is that of the d^2-law [4, 14, 21, 37, 55, 87, 93]. Neglecting the initial transient heat-up period, the d^2-law of droplet evaporation is considered a steady-state empirical evaporation model. Where one assumes the wet-bulb temperature has been reached, i.e., mass and heat transfer have reached a local thermodynamic equilibrium, experiments have widely validated the empirical correlation for the steady droplet diameter time rate of change,

$$\frac{\mathrm{d}d^2}{\mathrm{d}t} = -\alpha\,, \tag{5.27}$$

where α is known as the evaporation constant. The application of such a model is limited to cases in which the heat-up time, t_h, is insignificant due to the relative temperature change, or significantly shorter than the droplet lifetime, t_l. Furthermore, the evaporation constant for a d^2-law implementation is selected *a priori* based upon knowledge of the gaseous carrier and expected wet-bulb temperature. As a result, information regarding the droplet temperature may ultimately be ignored. The applicability of the d^2-law is therefore limited, but has seen wide adoption in a variety of applications such as for room-air bio-aerosol dispersion studies [17]. For cases in which the droplet lifetime and heat-up time are more comparable, transient heat and mass transfer rates during the initial droplet heat-up period become significantly more impactful. In liquid-fuel combustors for instance, initial droplet heat-up and vaporization rates produce stiff changes in droplet Reynolds number. Failure of capturing the strong size, temperature and inertial coupling risks producing erroneous mixing length estimates for example. These limitations therefore motivate the study of so-called unsteady hydrodynamic evaporation models which are discussed in the following section, and provide the basis for the present implementation.

6.1.1 Unsteady Hydrodynamic Evaporation

The traditional unsteady hydrodynamic evaporation models are based upon solutions to the conservation of mass, momentum, and energy at the inter-phase gas-droplet surface boundary. As mentioned, these models typically neglect the convective detachment of molecules and are instead primarily concerned with diffusive mass transfer from the droplet surface [55, 87]. The most rudimentary of these models was first proposed by Maxwell in 1877 [33] and provides a description for droplet evaporation controlled solely by molecular diffusion. Following the general approach of Godsave and Spalding [36, 96], the mass diffusion equation for a spherically symmetric droplet according to Maxwell's model is simply

$$\frac{\mathrm{d}m_\ell}{\mathrm{d}t} = 4\pi r^2 D_v \frac{\mathrm{d}\rho_v}{\mathrm{d}r} \,. \tag{6.1}$$

Note, here onward, subscript ℓ refers to the liquid droplet phase, while subscript v denotes the droplet vapour, and subscript g refers to the gaseous carrier phase. Above, Equation (6.1) states the time rate of change of droplet mass is uniquely a function of the inward mass flux at the surface of a spherical shell of radius r. Of course, where r is larger than the droplet radius, r_ℓ, the inward mass flow rate of an arbitrary shell must be equal to that of another such that mass does not accumulate at some arbitrary distance from the droplet surface. As a result, the droplet mass time rate of change is effectively independent of r and Equation (6.1) is constant. As such, the Maxwell droplet evaporation model is consequently often considered a quasi-steady state droplet evaporation model. However, where integration over $r_\ell \to \infty$ is performed,

$$\int_{\rho_{v,s}}^{\rho_{v,\infty}} \mathrm{d}\rho_v = \frac{\mathrm{d}m_\ell}{\mathrm{d}t} \int_{r_\ell}^{\infty} \frac{1}{4\pi r^2 D_v} \,, \tag{6.2}$$

$$\rho_{v,\infty} - \rho_{v,s} = \frac{\mathrm{d}m_\ell}{\mathrm{d}t} \int_{r_\ell}^{\infty} \frac{1}{4\pi r_\ell D_v} \,, \tag{6.3}$$

$$\frac{\mathrm{d}m_\ell}{\mathrm{d}t} = -4\pi r_\ell D_v \left(\rho_{v,s} - \rho_{v,\infty}\right) \,, \tag{6.4}$$

one observes the total mass time rate of change becomes a function of the relative partial vapour density, i.e., the difference between the partial vapour density at the droplet sur-

face, $\rho_{v,s}$, and within the ambient far-field, $\rho_{v,\infty}$. Consequently, the commonly referred to Maxwell equation for droplet evaporation [33, 87], Equation (6.4), can produce unsteady transient behaviour, where one quantifies changes of ambient partial vapour density as a product of time-dependant evaporation and, more importantly, by modelling an expression for the partial vapour density at the droplet surface which is often a time-dependant function of both pressure and temperature. However, this is only discussed later. The range of applicability of the Maxwell equation for droplet evaporation is unfortunately limited by its sole inclusion of molecular diffusion. Fortunately however, Maxwell's model may be improved by consideration of the advective bulk motion of the gas-vapour mixture away from the droplet surface commonly known as Stefan flow [33, 55, 87].

Not to be confused with convective effects due to molecular detachment, Stefan flow is a transport phenomenon described by the movement of vapour due to a flow within the gaseous phase induced by the addition or loss of mass at the gas-droplet interface. Its inclusion for the improvement of Maxwell's model was first suggested by Fuchs in 1959, and is commonly known as the Stefan-Fuchs droplet evaporation model [33,87,105]. Terms describing Stefan flow arise from the additional constraint of uniform total pressure within gas-vapour mixture of droplet surface near-field, and is imposed by restricting the spatial derivatives of the partial pressures of gas and vapour to be equal and opposite,

$$\frac{\mathrm{d}p_v}{\mathrm{d}r} = -\frac{\mathrm{d}p_g}{\mathrm{d}r}\,. \tag{6.5}$$

By invoking the ideal gas law for the gas-vapour mixture and knowing the net gas mass flux towards to gas-droplet interface during evaporation is effectively zero, the bulk velocity of the gas-vapour mixture can then be expressed as

$$u = \frac{D_g}{\rho_g}\frac{\mathrm{d}\rho_g}{\mathrm{d}r}\,. \tag{6.6}$$

For the case of monocomponent evaporation, the mass diffusivity of the vapour within the gas-vapour mixture is expected to simply be equal to that of gas within the gas-vapour mixture, i.e,. $D_g = D_v$ [87]. The resulting mass time rate of change considering both

molecular diffusion and Stefan flow of vapour is then consequently taken as

$$\frac{\mathrm{d}m_\ell}{\mathrm{d}t} = 4\pi r^2 \left(D_v \frac{\mathrm{d}\rho_v}{\mathrm{d}r} - \rho_v u \right) = 4\pi r^2 D_v \left(\frac{\mathrm{d}\rho_v}{\mathrm{d}r} - \frac{\rho_v}{\rho_g} \frac{\mathrm{d}\rho_g}{\mathrm{d}r} \right) . \tag{6.7}$$

The problem remains however under-constrained and further assumptions are required to solve Equation (6.7) in closed-form. Authors have suggested several assumptions, such as holding the total pressure and molar concentration of the gas-vapour mixture constant [33]. More commonly used in practice however, the total gas-vapour density is typically held constant [87]. The derivation provided herein assumes the latter, where $\rho = \rho_g + \rho_v =$ const., and the spatial derivative is therefore zero. Rearranging and substituting into Equation (6.7),

$$\frac{\mathrm{d}m_\ell}{\mathrm{d}t} = 4\pi r^2 D_v \left(\frac{\mathrm{d}\rho_v}{\mathrm{d}r} - \frac{\rho_v}{\rho - \rho_v} \frac{\mathrm{d}}{\mathrm{d}r} \left(\rho - \rho_v \right) \right) = 4\pi r^2 D_v \left(\frac{\rho}{\rho - \rho_v} \right) \frac{\mathrm{d}\rho_v}{\mathrm{d}r} , \tag{6.8}$$

a closed-form expression for the droplet mass time rate of change is obtained by performing integration over $r_\ell \to \infty$,

$$\frac{\mathrm{d}m_\ell}{\mathrm{d}t} \int_{r_\ell}^{\infty} \mathrm{d}r = 4\pi r^2 D_v \int_{\rho_{v,s}}^{\rho_{v,\infty}} \left(\frac{\rho}{\rho - \rho_v} \right) \frac{\mathrm{d}\rho_v}{\mathrm{d}r} , \tag{6.9}$$

$$\frac{\mathrm{d}m_\ell}{\mathrm{d}t} = -4\pi r_\ell \rho D_v \ln \left(\frac{\rho - \rho_{v,\infty}}{\rho - \rho_{v,s}} \right) . \tag{6.10}$$

The above equation is often rearranged in terms of the dimensionless Spalding mass transfer number,

$$B_M = \frac{\rho_{v,s} - \rho_{v,\infty}}{\rho_{g,s}} = \frac{Y_{v,s} - Y_{v,\infty}}{Y_{g,s}} , \tag{6.11}$$

where $Y_i = \rho_i / \rho_t$ is the dimensionless mass fraction for the ith specie. The droplet mass time rate of change for the Stefan-Fuchs droplet evaporation model then takes the form of

$$\frac{\mathrm{d}m_\ell}{\mathrm{d}t} = -4\pi r_\ell \rho D_v \ln \left(1 + B_M \right) . \tag{6.12}$$

Interestingly, when $Y_{v,s} \ll 1$ and $Y_{v,\infty} \ll 1$, meaning $B_M \ll 1$, the Stefan-Fuchs equation reduces to the Maxwell equation for droplet evaporation of Equation (6.4) [87]. Moreover,

the above equation shares a similar quasi-steady state behaviour without consideration of neither time-dependant pressure nor temperature changes at the gas-droplet interface. However, where the gas-droplet partial vapour pressure is large, i.e., $B_M \gg 1$, disagreement between predicted evaporation rates becomes strong, as the Stefan flow transport phenomenon produces a significant increase of vapour mass transport from the gas-droplet interface. Notably, the accuracy of the above equation is strongly dependant on the accuracy of the estimated vapour mass diffusivity within the gas-vapour mixture, D_v. Most commonly, authors have proposed a unitary Lewis number assumption at the gas-droplet interface [55, 87, 92], where

$$\mathrm{Le} = 1 = \frac{k_m}{c_{p,m}\rho D_v}\,. \tag{6.13}$$

Here, the subscript m represents mixture-averaged quantities of the thermal conductivity, k, and heat capacity, c_p, of the gas-vapour mixture. According to Lefebvre and McDonell [55], estimates for these mixture averaged properties may be obtained using the one-third rule [45, 97]. Specifically, an approximate weighted reference temperature, T_r, and weighted vapour mass fraction, $Y_{v,r}$, are estimated using

$$T_r = \frac{2}{3}T_s + \frac{1}{3}T_\infty\,, \tag{6.14}$$

$$Y_{v,r} = \frac{2}{3}Y_{v,s} + \frac{1}{3}Y_{v,\infty}\,. \tag{6.15}$$

A simple linear mass fraction weighting rule is then commonly used to determine the mixture-averaged quantities, using the properties of both phases evaluated at the one-third rule reference values. Explicitly, these rules are

$$k_m = Y_{v,r}k_v(T_r) + (1 - Y_{v,r})k_g(T_r)\,, \tag{6.16}$$

$$c_{p,m} = Y_{v,r}c_{p,v}(T_r) + (1 - Y_{v,r})c_{p,g}(T_r)\,. \tag{6.17}$$

These weighted rules notably assume temperature-dependant values for all species are provided, either using empirical correlations or interpolated experimental data. By substitution of Equations (6.13), (6.16) and (6.17) into Equation (6.12), the mass time rate of

change within the Stefan-Fuchs droplet evaporation model becomes

$$\frac{\mathrm{d}m_\ell}{\mathrm{d}t} = -4\pi r_\ell \frac{k_m}{c_{p,m}} \ln\left(1 + B_M\right). \tag{6.18}$$

Generalizations have been proposed to Equation (6.18) which introduce its dependency to the ratio of convective and diffusive mass transfer, also known as the dimensionless Sherwood number, Sh. Also known as the mass transfer Nusselt number, the Sherwood number takes into account the movement of droplets [1, 87]. Where Stefan flow is considered, the Sherwood number is expressed as

$$Sh = Sh_0 \frac{\ln\left(1 + B_M\right)}{B_M}, \tag{6.19}$$

with Sh_0 a function of the droplet Reynolds number and Schmidt number, Sc, which is a dimensionless number describing the ratio of momentum diffusivity and mass diffusivity. An analogous expression may be derived for the dimensionless Nusselt number, i.e., the ratio of convective and conductive heat transfer, in Stefan flow,

$$Nu = Nu_0 \frac{\ln\left(1 + B_M\right)}{B_M}. \tag{6.20}$$

For the case of stationary non-evaporating droplets, $Nu_0 = Sh_0 = 2$ [1, 55, 87]. For moving droplets, empirical corrective correlations have been suggested by several authors as identified by Sazhin [11, 16, 33, 92, 115, 124], of which the simplest expressions are typically deployed for numerical implementations. Generally, these take the form of

$$Nu_0 = 2\left(1 + c\, Re^{\frac{1}{2}}\, Pr^{\frac{1}{3}}\right), \tag{6.21}$$

$$Sh_0 = 2\left(1 + c\, Re^{\frac{1}{2}}\, Sc^{\frac{1}{3}}\right). \tag{6.22}$$

Among the most widely known correlations are those of Frössling [32] and those of Ranz and Marshall [82], which proposed $c = 0.276$ and $c = 0.3$, respectively. The selection of an appropriate corrective correlation for both the Nusselt and Sherwood numbers remains however *ad hoc* and dependant on the observed gaseous flow. Expressed in terms of the

Sherwood number, the mass time rate of change of the corrected Stefan-Fuchs droplet evaporation model then finally becomes

$$\frac{\mathrm{d}m_\ell}{\mathrm{d}t} = -2\pi r_\ell \frac{k_m \, Sh_0}{c_{p,m}} \ln\left(1 + B_M\right). \tag{6.23}$$

Where droplets are strictly spherical, an expression for the diameter time rate of change may then be obtained by simple transformation of Equation (6.12),

$$m_\ell = \frac{\pi}{6} \rho_\ell \, d_\ell^3 \,, \tag{6.24}$$

$$\frac{\mathrm{d}m_\ell}{\mathrm{d}t} = \frac{\pi}{2} \rho_\ell \, d_\ell^2 \frac{\mathrm{d}d_\ell}{\mathrm{d}t} \,, \tag{6.25}$$

$$\frac{\mathrm{d}d_\ell}{\mathrm{d}t} = \Upsilon_d = -\frac{2 \, k_m \, Sh_0}{c_{p,\ell} \, c_{p,m} \, d} \ln\left(1 + B_M\right). \tag{6.26}$$

The unsteady nature of Stefan-Fuchs droplet evaporation model is introduced by modelling of droplet heating and partial vapour pressure at the gas-droplet interface. A model for the unsteady droplet heating can be obtained by following the derivation provided by Lefebvre and McDonell [55]. Therein, a quasi-steady gas phase assumption is proposed, whereby the boundary layer at the gas-droplet interface is assumed identical to that of a steady boundary layer for identical conditions, e.g., velocity, surface area, temperature and pressure. For such an assumption, with the consideration of Stefan flow of Equation (6.20), the Nusselt number is taken as

$$Nu = \frac{h d_\ell}{k_m} = Nu_0 \frac{\ln(1 + B_M)}{B_M} \,, \tag{6.27}$$

where h is the convective heat transfer coefficient, d_ℓ the droplet diameter and k_m the thermal conductivity of the gas-vapour mixture. The convective heat transfer observed at the gas-droplet interface is obtained using Newton's law of cooling, whereby

$$Q_c = \pi d_\ell^2 h \left(T_\infty - T_s\right) . \tag{6.28}$$

The convective heat transfer coefficient is obtained by rearrangement of Equation (6.27)

for subsequent substitution into Equation (6.28),

$$Q_c = \pi d_\ell k_m Nu_0 \frac{\ln(1+B_M)}{B_M} \left(T_\infty - T_s\right) . \tag{6.29}$$

The net heat flux at the gas-droplet interface is however not solely a function of the convective heat transfer. Rather, heat transfer is also incurred by the inherent transport of energy during the transport of mass during vaporization. Consequently, the heat transfer due to vaporization must be considered, and is evaluated as

$$Q_e = \Delta h \frac{\mathrm{d}m_\ell}{\mathrm{d}t} , \tag{6.30}$$

with Δh being the latent heat of vaporization of the liquid droplet. The mass time rate of change in the above expression is obtained by substitution of Equation (6.18) from the Stefan-Fuchs droplet evaporation model, thus yielding

$$Q_e = -\pi d_\ell \Delta h \frac{k_m}{c_{p,m}} Nu_0 \, \ln\left(1+B_M\right) . \tag{6.31}$$

where Equation (6.18) is expressed in terms of the Nusselt number of Equation (6.27). Note, where heat transfer rates are controlling during droplet heat-up, a substitution of Sh_0 for Nu_0 is justified [55]. The net inward heat flux at the gas-droplet interface becomes the sum of both convective and latent heat transfer effects,

$$Q_{\mathrm{net}} = Q_c + Q_e , \tag{6.32}$$

$$Q_{\mathrm{net}} = \pi d_\ell \, k_m \, Nu_0 \ln(1+B_M) \left(\frac{T_\infty - T_s}{B_M} - \frac{\Delta h}{c_{p,m}} \right) . \tag{6.33}$$

In order to obtain a simplified expression for the temperature time rate of change of the liquid droplet, a zero internal temperature gradient assumption is proposed. Rather, the gas-droplet interface temperature, T_s, is assumed equal to the mean volumetric temperature, T_ℓ, of the discrete liquid droplet. This assumption implies thermal diffusion waves travel rapidly from the gas-droplet interface into the droplet core, such that the droplet lifetime becomes significantly larger than the droplet heat-up period. Limitations on the

range of applicability of this assumption within the present work are noted. The reader is invited to further investigate these limitations as discussed by Sazhin [87]. The temperature time rate of change of the liquid droplet is thus obtained as,

$$c_{p,\ell}\, m_\ell \frac{\mathrm{d}T_\ell}{\mathrm{d}t} = Q_{\text{net}}\,. \tag{6.34}$$

Here, the liquid droplet mass is obtained from Equation (6.24), rearrangement of Equation (6.34), along with subsequent substitution of Equation (6.33) to finally yield an expression for a Stefan-Fuchs based unsteady droplet heating model,

$$\frac{\mathrm{d}T_\ell}{\mathrm{d}t} = \Upsilon_T = \frac{6\, k_m\, Nu_0}{c_{p,\ell}\, \rho_\ell\, d_\ell^2} \ln(1 + B_M) \left(\frac{T_\infty - T_\ell}{B_M} - \frac{\Delta h}{c_{p,m}} \right)\,. \tag{6.35}$$

While not overtly conspicuous, the temperature dependency of the mass time rate of change of Equation (6.18) arises from modelling of the partial vapour mass fraction. Traditionally, the partial vapour mass fraction at the gas-droplet interface, $Y_{v,s}$, is evaluated using the Clausius-Clapeyron relation by proposing a phase-equilibrium assumption within the droplet boundary layer [55, 87, 92]. The Clausius-Clapeyron relation is derived from the state postulate, and using the ideal gas approximation, it takes the form of

$$\ln\left(\frac{p_2}{p_1}\right) = -\frac{\Delta H}{R}\left(\frac{1}{T_2} - \frac{1}{T_1}\right)\,, \tag{6.36}$$

where the numerical subscripts refer to two distinct partial pressures, p_i, and temperature, T_i, states. Moreover, ΔH refers to the molar latent heat of vaporization and R is the universal gas constant. The relation of Equation (6.36) is then rewritten in terms of a desired partial vapour pressure, e.g., $p_{v,s}$, at temperature T_ℓ as related to some reference state. Commonly, the reference state is chosen to be the boiling temperature in standard atmosphere. However, the Clausius-Clapeyron relation is only applicable to states near the reference state. As such, some care in the choice of the reference state is required during *a priori* selection for a desired case. Isolating for $p_{v,s}$, an expression for the partial vapour

pressure is obtained from Equation (6.36) as

$$p_{v,s} = p_{v,r} \exp\left(-\frac{\Delta H}{R}\left(\frac{1}{T_\ell} - \frac{1}{T_r}\right)\right) . \tag{6.37}$$

Note, the reference temperature selected above is distinct from the reference temperature obtained from the one-third rule for evaluating gas-vapour mixture quantities. By definition, the partial vapour mass fraction is simply

$$Y_{v,s} = \frac{\rho_{v,s}}{\rho} . \tag{6.38}$$

Treating both the vapour and gas-vapour mixture as ideal gases, i.e., $\rho = p\,M/RT$, the following expression for the vapour mass fraction at the gas-droplet interface is derived,

$$Y_{v,s} = \frac{p_{v,s} M_v}{p_{v,s} M_v + p_{g,s} M_g} , \tag{6.39}$$

with M_i the molar masses, and $p_{i,s}$ the partial pressures of the ith specie. Applying Dalton's law, $p_s = p_{v,s} + p_{g,s}$, along with assumption of constant total pressure, i.e., p_s is assumed to be equivalent to the ambient far-field pressure, P, Equation (6.39) may be rearranged as

$$Y_{v,s} = \frac{p_{v,s} M_v}{p_{v,s} M_v + (P - p_{v,s})\, M_g} . \tag{6.40}$$

Substitution of the Clausius-Clapeyron relation into the above expression allows the dimensionless Spalding mass transfer number be then expressed as a function of ambient pressure and droplet temperature. The resulting system of equations produces strong coupling between both mass and temperature time rates of change, and effectively produces the so-called Stefan-Fuchs unsteady hydrodynamic droplet evaporation model.

6.1.2 An Approximate Stefan-Fuchs Droplet Evaporation Model

While more advanced unsteady hydrodynamic evaporation models have been developed, such as that of Abramzon and Sirignano's film theory-based approach [1], implementation of these models within a moment-based framework proves markedly difficult. As previously discussed in Section 3.1, weights of the phase-space density distribution function are typically higher-order monomials of the extended phase-space variables. However, where expressions for the time rates of change of these phase-space variables, $\Upsilon_{\breve{i}}$, become significantly non-linear or complex, the existence of closed-form or even defined integrals for the RHS moments is not inherently guaranteed. As a result, difficulties in the implementation of the discussed droplet evaporation models arise from the consequent troublesome integrals found within the RHS of the system of moment equations. Appropriate approximations to the expressions are consequently often required such to close the moments of the RHS. Precisely, such efforts are described below for the development of an approximate corrected Stefan-Fuchs droplet evaporation model within the scope of the proposed two-scalar PGM.

Provided within the above derivation of Section 6.1.1, expressions for the time rate of change of diameter, Υ_d, and temperature, Υ_T, were obtained for strictly spherical moving droplets in accordance to the Stefan-Fuchs evaporation model. These expression were, respectively,

$$\Upsilon_d = -\frac{2\,k_m\,Sh_0}{c_{p,\ell}\,c_{p,m}\,d}\ln\left(1+B_M\right), \tag{6.26}$$

$$\Upsilon_T = \frac{6\,k_m\,Nu_0}{c_{p,\ell}\,\rho_\ell\,d^2}\ln(1+B_M)\left(\frac{T_\infty - T}{B_M} - \frac{\Delta h}{c_{p,m}}\right). \tag{6.35}$$

For simplicity's sake, the ℓ subscript has been omitted from the variables of integration. Both expressions unfortunately contain strongly non-linear and complex functions of the internal variables of the extended phase-space density distribution, $\tilde{\mathcal{G}}$. Most notably, the troublesome terms are the mixture-average quantities, k_m and $c_{p,m}$, the corrected dimensionless numbers, Nu_0 and Sh_0, and lastly terms containing the dimensionless Spalding mass transfer number, B_M. While the former contribute significant non-linearity to the moments due to polykinetic, polydispersed and polythermal considersations, these terms are largely neglected within the present work. Rather, the approximate model developed

herein is primarily concerned with recovery of Stefan flow effects, i.e., terms related to the dimensionless Spalding mass transfer number, B_M. Crudely, corrective coefficients and gas-vapour mixture quantities are instead simply evaluated using moment variables, i.e., u_i, σ and θ, which greatly simplifies the required moment integrals. Investigations into their full contributions to the moment-equations and subsequent accuracy improvement remain subject of future work. Consequently, where integration of these terms is neglected, the simplified Stefan-Fuchs equations are rearranged in a streamlined form as

$$\Upsilon_d^* = \frac{C_0}{d}\mathcal{H}_0(T)\,, \tag{6.41}$$

$$\Upsilon_T^* = \frac{C_1}{d^2}\left[(T_\infty - T)\,\mathcal{H}_1(T) - C_2\,\mathcal{H}_0(T)\right]\,. \tag{6.42}$$

Above, all integration constants have been collected. Likewise, approximate functions $\mathcal{H}_0(T) \approx \ln(1+B_M)$ and $\mathcal{H}_1(T) \approx \ln(1+B_M)/B_M$ have been introduced. The shape of either approximate function must be determined by analysis of the exact functions, but must also be chosen such to produce closed-form moment expressions, such as a polynomial fit for instance. Importantly, the recovery of the behaviour of the exact functions is necessary for the recovery of unsteady vaporization rates predicted by the inclusion of Stefan flow at higher partial vapour pressures.

The general behaviour of both exact functions is examined by graphical analysis. Example curves are shown for water droplets evaporating in dry air in standard atmosphere at $293\,\mathrm{K}$ and n-heptane droplets evaporating in dry air at $607.950\,\mathrm{Pa}$ and $593\,\mathrm{K}$ in Figure 6.1. Therein, one observes both functions are either monotonically decreasing, or increasing. Moreover, both functions exhibit asymptotic-like convergence in the lower limit, $T \to 0$, while both functions also admit singularities in their upper limits, $T \to \infty$. Notably, both these behaviours are physical. Specifically, where droplets theoretically approach absolute zero, vaporization due to vapour diffusion expectedly ceases. As a result, the vapour mass fraction tends to zero as the temperature approaches absolute zero, i.e., $\lim_{T\to 0} Y_{v,s} = 0$. Fortunately, algebraic expressions for these lower limits of the approximate functions are

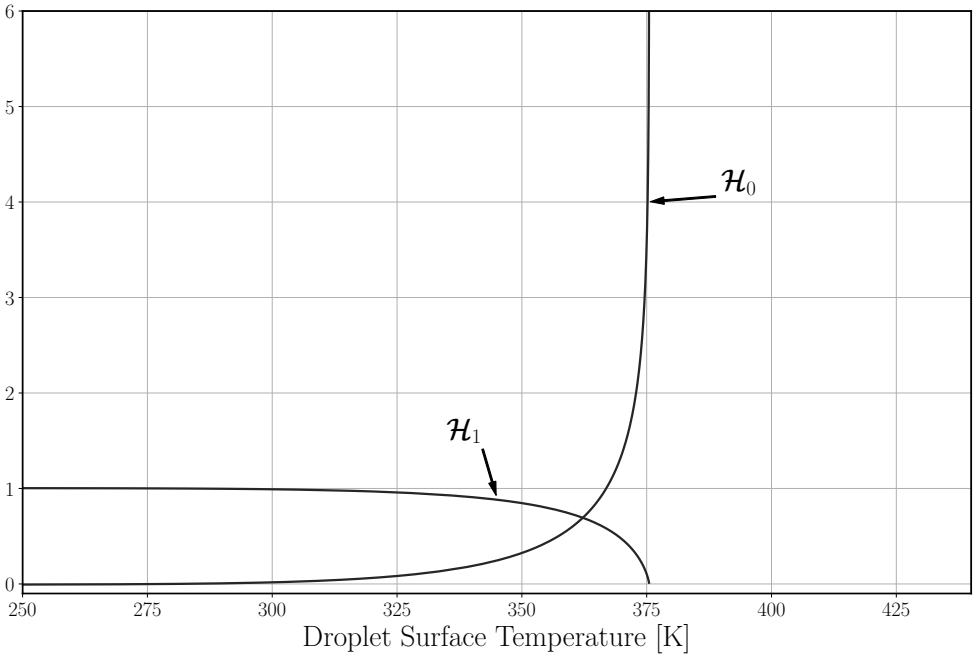

(a) Spray of water in dry air at **293 K** and **1 atm**.

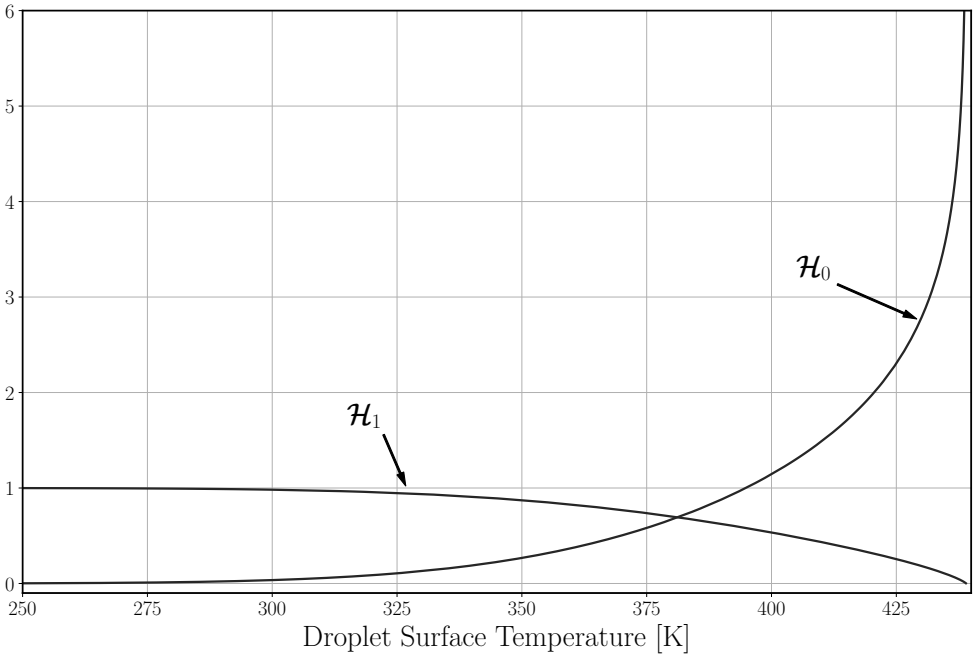

(b) Spray of n-heptane in dry air at **593 K** and **607 950 Pa**.

Figure 6.1: Exact functions $\mathcal{H}_0$ and $\mathcal{H}_1$ for two sprays.

well-defined,

$$\lim_{T\to 0} \ln(1+B_M) = \lim_{T\to 0} \ln\left(\frac{Y_{v,s}-Y_{v,\infty}}{1-Y_{v,s}}\right) = \ln(1-Y_{v,\infty})\,, \tag{6.43}$$

$$\lim_{T\to 0} \frac{\ln(1+B_M)}{B_M} = \frac{\ln(1-Y_{v,\infty})}{Y_{v,\infty}}\,. \tag{6.44}$$

Regarding the singularities, by inspection of Equation (6.11), B_M is observed to admit a discontinuity as the gas mass fraction, $Y_{g,s}$, tends to zero. This behaviour is expected. Specifically, as the partial vapour pressure at the gas-droplet interface approaches the total ambient atmospheric pressure, the rate of vaporization diverges to infinity as the droplet experiences instantaneous vaporization, or in other terms, the liquid proceeds to boil. The discontinuity in B_M, and therefore those of both exact functions, is thus located at the boiling temperature, T_b, of the liquid droplet. Within the proposed model, the upper boiling limit of both exact functions may be determined by the Clausius-Clapeyron relation, whereby

$$T_b = \frac{\Delta H\, T_r}{\Delta H - R T_r\, \ln(P/p_{v,r})}\,. \tag{6.45}$$

Again, the subscript r in the equation above refers not to the one-third averaging values, but to the Clausius-Clapeyron reference state. Given the exponential-like growth of both exact functions, the proposal of an exponential fit is an obvious choice in determining approximate functions. Specifically, exponential fits with three degrees of freedom are proposed for both functions,

$$\mathcal{H}_i(T) = Z_{i,0} + Z_{i,1} \exp(Z_{i,2}\, T)\,. \tag{6.46}$$

Note, the i subscript is adopted for generalization purposes and does not transform as regular tensors. Such to close the equations, two degrees of freedom are constrained by the lower and upper limits of the exact functions discussed above. As for the third degree of freedom, it is chosen such to recover the exact functions at steady-state. The so-called steady-state of the Stefan-Fuchs model is reached once the heat-up period is completed, i.e., droplets have reached their wet-bulb temperature, T_w. As previously mentioned, the wet-bulb temperature is the temperature at which convective heat transfer and advective

heat transfer of latent heat from vaporization reach equilibria. Importantly, the wet-bulb temperature is independent of the instantaneous droplet temperature. Rather, it may be determined *a priori* using gas-vapour mixture properties and ambient quantities. As such, when $\boldsymbol{\Upsilon}_T = \mathbf{0}$, the wet-bulb temperature becomes the solution to the following root optimization problem derived from Equation (6.35),

$$\begin{aligned} T_w &= \text{RootOf}\left(\frac{c_{p,m}}{\Delta h}\left(T_\infty - T\right) - B_M\right) , \\ &= \text{RootOf}\left(B_T - B_M\right) , \end{aligned} \tag{6.47}$$

where $B_T = c_{p,m}\left(T_\infty - T\right)/\Delta h$ is the dimensionless Spalding heat transfer number [33, 55, 87, 92, 96]. In other words, the steady-state wet-bulb temperature is found at the intersection of both dimensionless Spalding transfer number functions, i.e., where $B_T = B_M$. No analytical solution to Equation (6.47) has been found, however the numerical solution of the optimization problem is easily performed using a Newton-Raphson algorithm. Subsequently, the generalized solution for the free parameters, $Z_{i,j}$, of the ith exponential fit are obtained as

$$\begin{aligned} Z_{i,0} &= \exp(\eta_i)\frac{\mathcal{H}_{i,0}\exp(\eta_i) - \mathcal{H}_{i,w}}{1 - \exp(\eta_i)} , \\ Z_{i,1} &= \exp(\eta_i)\frac{\mathcal{H}_{i,w} - \mathcal{H}_{i,0}}{1 - \exp(\eta_i)} , \\ Z_{i,2} &= \frac{\eta_i}{T_w} . \end{aligned} \tag{6.48}$$

Here, the variable η_i is the solution to a root optimization problem for the ith fit. In generalized form, the root optimization problem is expressed as

$$\eta_i = \text{RootOf}\left(\eta_i\, T_b - \ln\left(\frac{\exp(\eta_i)\left(\mathcal{H}_{i,0} - \mathcal{H}_{i,b}\right) + \mathcal{H}_{i,b} - \mathcal{H}_{i,w}}{\mathcal{H}_{i,0} - \mathcal{H}_{i,w}}\right)\right) \tag{6.49}$$

In Equations (6.48) and (6.49), the values for $\mathcal{H}_{i,j}$ are evaluated from the aforementioned

constraints. For both functions, these are simply

$$\begin{aligned} \mathcal{H}_{0,0} &= \ln(1 - Y_{v,\infty})\,, & \mathcal{H}_{1,0} &= \frac{\ln(1 - Y_{v,\infty})}{Y_{v,\infty}}\,, \\ \mathcal{H}_{0,w} &= \ln\left(1 - B_T(T_w)\right)\,, & \mathcal{H}_{1,w} &= \frac{\ln\left(1 - B_T(T_w)\right)}{B_T(T_w)}\,, \\ \mathcal{H}_{0,b} &= \ln(1 - B_M(\varepsilon\, T_b))\,, & \mathcal{H}_{1,b} &= \frac{\ln(1 - B_M(\varepsilon\, T_b))}{B_M(\varepsilon\, T_b)}\,. \end{aligned} \tag{6.50}$$

Here, ε is a numerical tolerance for evaluating B_M near the singularity. Of course, an exponential fit does not admit a discontinuity. Therefore, a sufficiently large value near the discontinuity is instead evaluated with an *ad hoc* defined ε. As a result, the approximate functions are fully defined, and Equations (6.41) and (6.42) describe an approximate Stefan-Fuchs droplet evaporation model for the closed-form integration of moments of the two-scalar PGM phase-space density distribution function, $\tilde{\mathcal{G}}$.

The variability of the absolute error produced by the proposed approximate functions is very high-dimensional. Functions of the Clausius-Clapeyron relation, gas-vapour mixture-averaged quantities and ambient conditions, the incurred error over the integrable domain varies significantly between various sprays. An illustration of this variability is provided in Figure 6.2, whereby plots of the approximate functions are compared against the exact functions previously shown in Figure 6.1. Upon investigation of the $\mathcal{H}_0$ curves, one observes the largest disagreement in the upper limit, while the exact function is very well recovered in the lower limit. In particular, the approximate $\mathcal{H}_0$ function is continuous at the boiling temperature, T_b, while the exact function is not. While such behaviour prevents the capturing of instantaneous evaporation for near boiling sprays, the continuous nature of the approximate function is a necessary requirement for integration of the RHS moments of the two-scalar PGM. Concerning the curves of $\mathcal{H}_1$, great agreement is observed using the proposed approximate function for the n-heptane spray, with lesser agreement in the upper limit for the water spray. Nevertheless, the absolute error remains small and the exact value at the boiling temperature is recovered. Moreover, upon identifying the wet-bulb temperature on both plots, the expected exact recovery of both $\mathcal{H}_0$ and $\mathcal{H}_1$ is observed. In fact, in the regime near the wet-bulb temperature expected of water droplets sprayed into typical

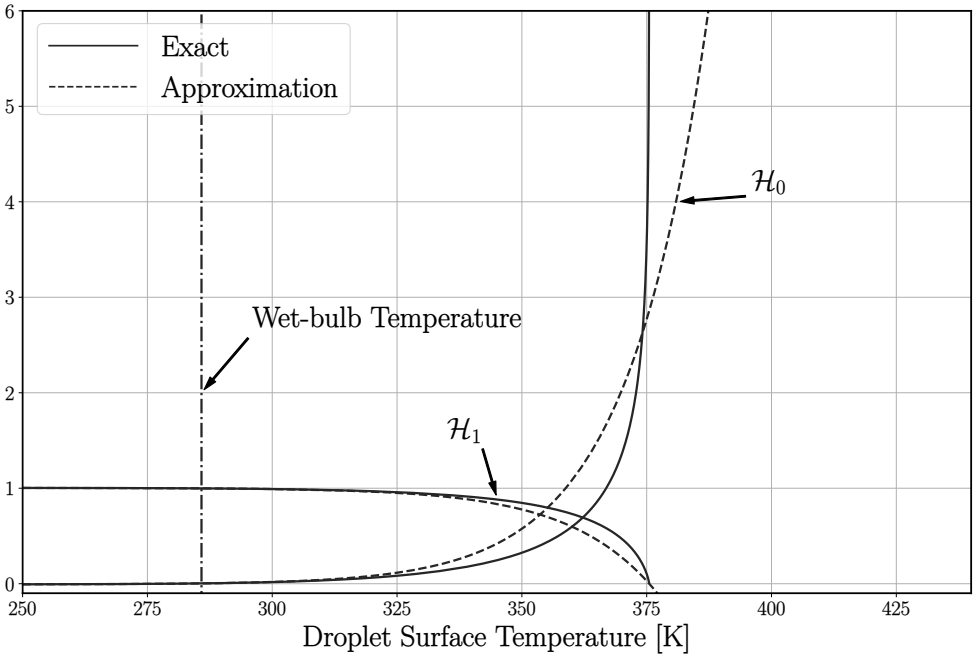

(a) Spray of water in dry air at **293 K** and **1 atm**.

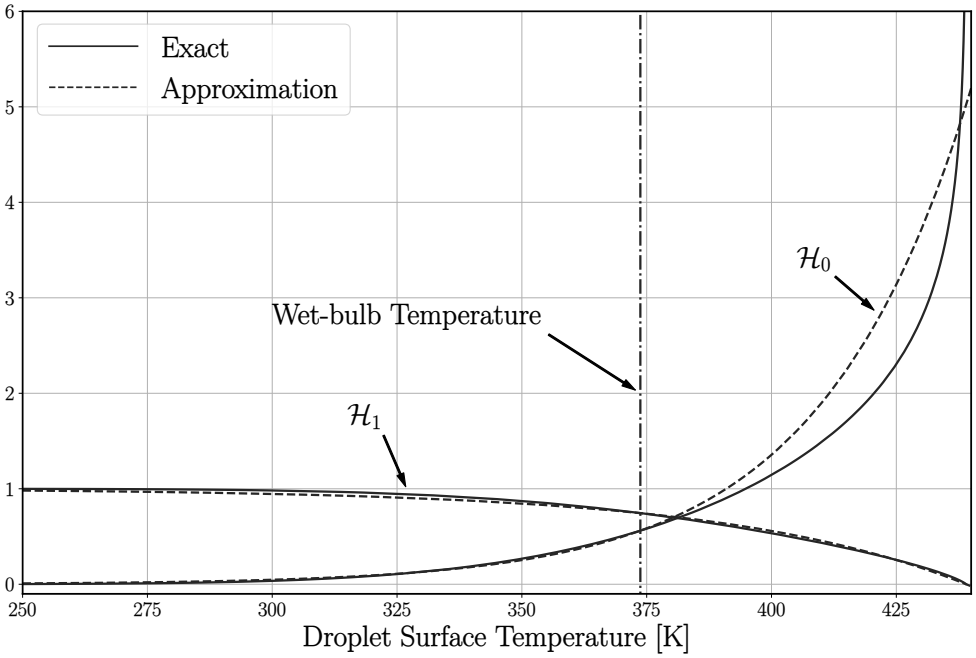

(b) Spray of n-heptane in dry air at **593 K** and **607 950 Pa**.

Figure 6.2: Comparison of the exact and approximate functions $\mathcal{H}_0$ and $\mathcal{H}_1$ for two sprays.

room-air, the error incurred by the approximate functions is near negligible. Conversely, a larger error is expected for n-heptane droplets above the wet-bulb temperature. However, at the temperatures illustrated, heat transfer rates are expectedly large and droplets will quickly settle to the wet-bulb temperature, i.e., the error will quickly decrease. Given these observations, the proposed approximate functions are deemed sufficiently accurate for implementation within the two-scalar PGM for evaporating sprays.

The proposed approximate Stefan-Fuchs droplet evaporation model can finally be integrated within the partial RHS of the moment equations, where

$$\bar{\boldsymbol{S}}_e = \bar{\boldsymbol{S}}_d + \bar{\boldsymbol{S}}_T = -\left\langle \bar{\boldsymbol{\mathcal{W}}} \frac{\partial}{\partial \ln(d)} \left(\frac{\Upsilon_d^*}{d} \tilde{\mathcal{G}} \right) \right\rangle - \left\langle \bar{\boldsymbol{\mathcal{W}}} \frac{\partial}{\partial T} \left(\Upsilon_T^* \tilde{\mathcal{G}} \right) \right\rangle . \tag{6.51}$$

Integration of the moments for the surface-weighted weight vector, $\bar{\boldsymbol{\mathcal{W}}}$, with approximate time rates of change, Υ_d^* and Υ_T^*, is achieved through square completion of the exponent from the resulting product of $\exp(Z_{i,2}T)\,\tilde{\mathcal{G}}$. The resulting integrated moments are presented separately below in streamlined form. The diameter time rate of change related terms are

$$\bar{S}_d^{(0)} = 2\,\pi\,C_0\,n\left[Z_{0,0} + Z_{0,1}\,\mathcal{E}_0\right] , \tag{6.52}$$

$$\bar{S}_{d_i}^{(1)} = 2\,\pi\,C_0\,n\left[Z_{0,0}\,u_i + Z_{0,1}\,\mathcal{E}_0\left(u_i + Z_{0,2}\Psi_{iT}\right)\right] , \tag{6.53}$$

$$\bar{S}_{d_d}^{(2)} = 2\,\pi\,C_0\,n\left[Z_{0,0}\left(\mu + 0.5\right) + Z_{0,1}\,\mathcal{E}_0\left(\mu + Z_{0,2}\Psi_{dT} + 0.5\right)\right] , \tag{6.54}$$

$$\bar{S}_{d_T}^{(3)} = 2\,\pi\,C_0\,n\left[Z_{0,0}\,\theta + Z_{0,1}\,\mathcal{E}_0\left(\theta + Z_{0,2}\Psi_{TT}\right)\right] , \tag{6.55}$$

$$\begin{aligned}\bar{S}_{d_{ij}}^{(4)} = 2\,\pi\,C_0\,n\big[&Z_{0,0}\left(\Psi_{ij} + u_i u_j\right) \\ &+ Z_{0,1}\,\mathcal{E}_0\left(\Psi_{ij} + \left(u_i + Z_{0,2}\Psi_{iT}\right)\left(u_j + Z_{0,2}\Psi_{jT}\right)\right)\big] ,\end{aligned} \tag{6.56}$$

$$\begin{aligned}\bar{S}_{d_{dd}}^{(5)} = 2\,\pi\,C_0\,n\big[&Z_{0,0}\left(\Psi_{dd} + \mu^2 + \mu\right) \\ &+ Z_{0,1}\,\mathcal{E}_0\left(\Psi_{dd} + \left(\mu + Z_{0,2}\Psi_{dT}\right)^2 + \left(\mu + Z_{0,2}\Psi_{dT}\right)\right)\big] ,\end{aligned} \tag{6.57}$$

$$\bar{S}_{d_{TT}}^{(6)} = 2\,\pi\,C_0\,n\left[Z_{0,0}\left(\Psi_{TT} + \theta^2\right) + Z_{0,1}\,\mathcal{E}_0\left(\Psi_{TT} + \left(\theta + Z_{0,2}\Psi_{TT}\right)^2\right)\right] , \tag{6.58}$$

$$\begin{aligned}\bar{S}_{d_{id}}^{(7)} = 2\,\pi\,C_0\,n\big[&Z_{0,0}\left(\Psi_{id} + u_i\mu + 0.5\,u_i\right) \\ &+ Z_{0,1}\,\mathcal{E}_0\left(\Psi_{id} + \left(u_i + Z_{0,2}\Psi_{iT}\right)\left(\mu + Z_{0,2}\Psi_{dT}\right) + 0.5\left(u_i + Z_{0,2}\Psi_{iT}\right)\right)\big] ,\end{aligned} \tag{6.59}$$

(6.60)

$$\bar{S}_{d_{iT}}^{(8)} = 2\,\pi\,\pi\,C_0\,n\,[Z_{0,0}\,(\Psi_{iT} + u_i\theta) \tag{6.61}$$
$$+Z_{0,1}\,\mathcal{E}_0\,(\Psi_{iT} + (u_i + Z_{0,2}\Psi_{iT})\,(\theta + Z_{0,2}\Psi_{TT}))]\ ,$$
$$\bar{S}_{d_{dT}}^{(9)} = 2\,\pi\,C_0\,n\,[Z_{0,0}\,(\Psi_{dT} + \mu\theta + 0.5\,\theta) \tag{6.62}$$
$$+Z_{0,1}\,\mathcal{E}_0\,(\Psi_{dT} + (\mu + Z_{0,2}\Psi_{dT})\,(\theta + Z_{0,2}\Psi_{TT}) + 0.5\,(\theta + Z_{0,2}\Psi_{TT}))]\ ,$$

with $\mathcal{E}_0 = \exp\left(0.5\,Z_{0,2}\,(\Psi_{TT}\,Z_{0,2} + 2\,\theta)\right)$. Similarly, the non-zero temperature time rate of change related terms are

$$\bar{S}_{T_T}^{(3)} = \pi\,C_1\,n\,[Z_{1,0}\,(T_\infty - \theta) + Z_{1,1}\mathcal{E}_1\,(T_\infty - (\theta + Z_{1,2}\Psi_{TT})) \tag{6.63}$$
$$-C_2\,(Z_{1,0} + Z_{1,1}\mathcal{E}_1)]\ ,$$
$$\bar{S}_{T_{TT}}^{(6)} = 2\,\pi\,C_1\,n\,\left[Z_{1,0}\,\left(T_\infty\theta - \left(\Psi_{TT} + \theta^2\right)\right)\right. \tag{6.64}$$
$$+ Z_{1,1}\mathcal{E}_1\,\left(T_\infty\,(\theta + Z_{1,2}\Psi_{TT}) - \left(\Psi_{TT} + (\theta + Z_{1,2}\Psi_{TT})^2\right)\right)$$
$$-C_2\,(Z_{1,0}\,\theta + Z_{1,1}\mathcal{E}_1\,(\theta + Z_{1,2}\Psi_{TT}))]\ ,$$
$$\bar{S}_{T_{iT}}^{(8)} = \pi\,C_1\,n\,[Z_{1,0}\,(T_\infty u_i - (\Psi_{iT} + u_i\theta)) \tag{6.65}$$
$$+ Z_{1,1}\mathcal{E}_1\,(T_\infty\,(u_i + Z_{1,2}\Psi_{iT}) - (\Psi_{iT} + (u_i + Z_{1,2}\Psi_{iT})\,(\theta + Z_{1,2}\Psi_{TT})))$$
$$-C_2\,(Z_{1,0}\,u_i + Z_{1,1}\mathcal{E}_1\,(u_i + Z_{1,2}\Psi_{iT}))]\ ,$$
$$\bar{S}_{T_{dT}}^{(9)} = \pi\,C_1\,n\,[Z_{1,0}\,(T_\infty\mu - (\Psi_{dT} + \mu\theta)) \tag{6.66}$$
$$+ Z_{1,1}\mathcal{E}_1\,(T_\infty\,(\mu + Z_{1,2}\Psi_{dT}) - (\Psi_{dT} + (\mu + Z_{1,2}\Psi_{dT})\,(\theta + Z_{1,2}\Psi_{TT})))$$
$$-C_2\,(Z_{1,0}\,\mu + Z_{1,1}\mathcal{E}_1\,(\mu + Z_{1,2}\Psi_{dT}))]\ ,$$

with $\mathcal{E}_1 = \exp\left(0.5\,Z_{1,2}\,(\Psi_{TT}\,Z_{1,2} + 2\,\theta)\right)$. As a reminder, the coefficients within the above equations are explicitly

$$C_0 = -\frac{2\,k_m\,Sh_0}{c_{p,m}}\,, \tag{6.67}$$
$$C_1 = \frac{6\,k_m\,Nu_0}{c_{p,\ell}\,\rho_\ell}\,, \tag{6.68}$$
$$C_2 = \frac{\Delta h}{c_{p,m}}\,. \tag{6.69}$$

Here, the gas-vapour mixture-averaged quantities are evaluated using the one-third rule at θ, and the convection correction terms, Sh_0 and Nu_0, evaluated using the Frössling correlations with the use of first-order moments. Substitution of the 27 equations presented above into the RHS of the proposed two-scalar PGM for evaporating sprays effectively provides a novel Eulerian-based treatment for unsteady evaporating sprays. Further analyses regarding the accuracy of the moment-based system of equations is provided in Chapter 8.

6.2 Inertial Gas-Droplet Coupling

The consideration of inertial gas-droplet coupling arises from the inclusion of various body forces which result from gas-droplet interactions. Within the two-scalar PGM for evaporating sprays, these acceleration fields are collected within the RHS velocity time rate of change, a_α, and describe the instantaneous acceleration of a discrete particle in extended phase-space due to physical interaction with the gaseous carrier phase. In traditional gas-particle multiphase flow models, these forces typically include inertial drag, rotational lift and gravitational forces—among others [122]. The inclusion of these forces is however subject to an evaluation of their individual relevance. Within the scope of the present two-scalar PGM for evaporating sprays, these forces have as a result been limited to those of droplets in steady Stokes regime for irrotational particles, whereby rotational lift forces are neglected. The following section details the inertial modelling decisions in length for the proposed two-scalar PGM for evaporating sprays. Specifically, a review of traditional aerodynamic drag laws for gas-droplet multiphase flows shall be presented, along with a description of the implemented model. Moreover, and most notably, additional considerations for turbulent droplet dispersion will be discussed and a novel approximation to turbulent gas-droplet coupling is proposed within the scope of the present model.

6.2.1 Aerodynamic One-way Coupling

Traditionally, inertial gas-droplet coupling is characterized by the dimensionless Stokes number, St, which describes the degree of inertial coupling between the gaseous carrier and discrete droplet [14, 125]. This Stokes number is expressed as the ratio between the momentum response timescale of a droplet and the characteristic velocity timescale of the gaseous flow. Explicitly, it is

$$St = \frac{\tau_d}{\tau_g}\,, \tag{6.70}$$

where τ_d is the momentum response timescale and τ_g the velocity timescale of the gaseous phase. Generally, the momentum response timescale for a discrete droplet is expressed as

$$\tau_d = \frac{\rho_\ell\, d^2}{18\mu_g}\,, \tag{6.71}$$

from which a conspicuous relationship between droplet size and momentum response is observed. The response timescale is however also a function of the droplet mass density, ρ_ℓ, and gaseous carrier dynamic viscosity, μ_g. Intuitively, where the Stokes number is small, i.e., $St \ll 1$, gas-droplet momenta are strongly coupled. In other words, the droplet momentum response timescale is amply small to accommodate changes, or fluctuations, of the flow velocity, and droplets exhibit increasingly tracer-like behaviour. Conversely, where $St \gg 1$, droplets experience weaker coupling to changes of the background flow velocity, whereby high-frequency fluctuations of the velocity field do not interact with droplets at large Stokes numbers. In the context of polydispersed evaporating sprays, droplet distributions can be expected to develop wide ranges of local Stokes numbers. Consequently, inclusion of aerodynamic drag within the proposed model can be expected to introduce significant non-linear contributions to the moment-equations. Robust and simple expressions are consequently preferred and therefore guide the proposal of a steady-Stokes regime assumption within the present work. Note, the description of a steady regime within this context refers to the omission of effects related to accelerations within the background gaseous flow field.

The general equation for the discrete-droplet velocity time rate of change due to aerodynamic effects is [14, 55, 77, 87, 92, 100, 125],

$$\frac{\mathrm{d}v_i}{\mathrm{d}t} = \frac{f(Re_d)}{\tau_d}\left(U_i - v_i\right) . \tag{6.72}$$

The equation describes the hydrodynamic resistance force exerted by the gaseous phase upon the droplet as a function of the droplet momentum response timescale and relative gas-droplet veloicty. Here, U_i is the background fluid velocity and v_i is the discrete-droplet velocity. Notably however, the equation also includes effects of the inertia force, $f(Re_d)$, which is a function of the droplet Reynolds number, Re_d. Simply, the droplet Reynolds number is expressed as the traditional characteristic fluid flow Reynolds number but evaluated at the droplet scale. It is therefore

$$Re_d = \frac{\rho_g \, d \left|U_i - v_i\right|}{\mu_g} , \tag{6.73}$$

and describes the relative importance of inertial forces against viscous forces at the droplet lengthscale. A generalization to the function is presented as [14]

$$f(Re_d) = \frac{\mathrm{C}_d \, Re_d}{24} , \tag{6.74}$$

where C_d is the dimensionless aerodynamic drag coefficient. However, numerous other expressions have been proposed for $f(Re_d)$, whether by analytical or empirical justification, and vary greatly in algebraic complexity and accuracy over ranges of Re_d. According to Zaichik, the most common of these is the Schiller-Neumann approximation [11, 125],

$$f(Re_d) = \begin{cases} 1 + 0.15 \, Re_d^{0.687} & Re_d \leq 10^3 \\ 0.11 \, Re_d / 6 & Re_d > 10^3 \end{cases} . \tag{6.75}$$

Unfortunately, Equation (6.75) introduces both piece-wise behaviour and non-integer degree monomials of the discrete-droplet velocity. Subsequent consideration of Equation (6.72) by implementation of Equation (6.75) therefore introduces significant challenges in producing closed-form moment expressions within the RHS of the proposed two-scalar PGM.

These limitations, in the absence of an approximate function for $f(Re_d)$, therefore motivate the assumption of steady Stokes regime. First described by Stokes in 1851 [98], the Stokes regime is observed at low droplet Reynolds number, i.e., $Re_d \leq 1$. Within this viscosity dominated regime, the aerodynamic drag coefficient becomes linearly proportional to Re_d, whereby

$$\mathrm{C}_d = \frac{Re_d}{24}\,. \tag{6.76}$$

By substitution of Equation (6.76) into Equation (6.74), $f(Re_d)$ becomes unity [14]. As a result, Equation (6.72) reduces to

$$\frac{\mathrm{d}v_i}{\mathrm{d}t} = a_{S_i} = \frac{(U_i - v_i)}{\tau_d}\,. \tag{6.77}$$

which is widely known as the Stokes drag law. The justification of a Stokes flow assumption is however precarious within the context of spray modelling, as typical fuel sprays exhibit appreciable droplet Reynolds numbers [91]. These modelling limitations are duly noted within the present work, and future work shall investigate appropriate approximations to $f(Re_d)$ for a larger range of expected regimes. Similarly, for the situation of evaporating droplets, no-slip assumptions of the Stokes' law are widely known to fail at small particle scales, i.e., the sub-micron scale [18, 34, 65, 78]. Rather, rarefaction effects become non-negligible at such scales which requires the adoption of Stokes-Cunningham drag [78],

$$\mathrm{C}'_d = \frac{\mathrm{C}_d}{C_c}\,, \tag{6.78}$$

in which the coefficient C_c is the Cunningham correction to Stokes' drag law. In its generalized form, this coefficient is expressed as [18]

$$C_c = 1 + \frac{2\,\lambda}{d}\left(A_1 + A_2 \exp\left(\frac{-A_3\,d}{\lambda}\right)\right)\,, \tag{6.79}$$

with some experimentally determined coefficients, A_n, and the mean free path of the carrier fluid, λ. Again, the expression provided by Equation (6.79) poses a significant challenge in producing closed-form moment expressions—thus resulting in its omission within the present work. However, future work shall investigate the inclusion of Stokes-Cunningham drag.

Furthermore, while gravitational effects may often widely be neglected within fuel spray applications, buoyancy forces become significantly more important for larger scale problems, e.g., those of spray sedimentation observed in atmospheric pollution or bio-aerosol applications for instance. Their additional consideration within the inertial gas-droplet coupling model is trivial, and was first studied by Forgues *et al.* [26, 29]. Where droplet buoyancy is considered, the velocity time rate of change related to its effects is expressed as

$$\frac{\mathrm{d}v_i}{\mathrm{d}t} = a_{g_i} = \frac{\rho_\ell - \rho_g}{\rho_g}\, g_i \,, \tag{6.80}$$

where g_i is the gravitational acceleration vector. Of course, the proposed inertial acceleration, a_α, considered herein consists of the summation of both Equations (6.77) and (6.80). The implementation of the proposed model within a lognormal diameter-based PGM is not entirely novel, and was first performed by Forgues *et al.* [26, 29]. Where the relevant partial RHS of the moment equations is

$$\bar{\boldsymbol{S}}_{\boldsymbol{v}} = \left\langle \left(a_{S_\alpha} + a_{g_\alpha}\right) \tilde{\mathcal{G}} \frac{\partial \bar{\boldsymbol{\mathcal{W}}}}{\partial v_\alpha} \right\rangle \tag{6.81}$$

integration of the resulting surface-weighted moment-equations produces non-zero contributions to first- and second-order velocity moments, which also includes co-variances with the extended phase-space variables of diameter and temperature. These contributions to the RHS source term for the proposed two-scalar PGM for evaporating sprays are

$$\bar{S}_{vi}^{\,(1)} = \frac{\pi\, n}{\gamma}\, \left(U_i - u_i\right) + a_{g_i}\, \bar{s} \,, \tag{6.82}$$

$$\bar{S}_{vij}^{\,(4)} = \frac{\pi\, n}{\gamma}\, \left[U_i\, u_j + U_j\, u_i - 2\left(\Psi_{ij} + u_i\, u_j\right)\right] + 2\, a_{g_i}\, \bar{s}\, \bar{u}_i \,, \tag{6.83}$$

$$\bar{S}_{vid}^{\,(7)} = \frac{\pi\, n}{\gamma}\, \left[U_i\, \mu - \left(\Psi_{id} + u_i \mu\right)\right] + a_{g_i}\, \bar{s}\, \bar{\mu} \,, \tag{6.84}$$

$$\bar{S}_{viT}^{\,(8)} = \frac{\pi\, n}{\gamma}\, \left[U_i\, \theta - \left(\Psi_{iT} + u_i \theta\right)\right] + a_{g_i}\, \bar{s}\, \bar{\theta} \,, \tag{6.85}$$

with $\gamma = 18\mu_g/\rho_\ell$. Where laminar droplet sedimentation is concerned, the above equations have been demonstrated by both Forgues *et al.* and Marchildon to yield an erroneous settling velocity-variance [26, 61]. The issue is well-understood, and as shown by

Marchildon, results in little disagreement with comparable model formulations which recover the exact solution for droplet sedimentation on small scales. Studies on larger scale atmospheric pollution-type problems may however suffer of inaccuracies based upon the Equations (6.82) to (6.85). Despite these concerns, the present work seeks to extend the proposed inertial gas-droplet coupling model of Forgues *et al.* by introducing turbulent dispersion. As mentioned, previous works have been uniquely concerned with laminar flow problems and have neglected effects of unresolved turbulence within the gaseous background flow. To this end, the following section introduces a novel first-order hyperbolicity maintaining approximation to unresolved turbulence coupling within the scope of the proposed two-scalar PGM for evaporating sprays.

6.2.2 Unresolved Turbulent One-way Coupling

Turbulence in gas-droplet multiphase flows introduces a multitude of physical phenomena which, at present, remain subject of ongoing research [5,27,39,100,110,125–127]. Responsible for enhanced coagulation, breakage, clustering, dispersion, evaporation, etc., turbulent flow considerations in gas-droplet multiphase flow are of great importance for the recovery of accurate predictions for myriad industrial and natural processes.

Traditionally, models for turbulent gas-droplet coupling are categorized into two types: Lagrangian or Eulerian formulations [125]. The former, much like was described in Section 2.1, are derived from a stochastic discrete-droplet trajectory formulation [110], which is typically obtained by solution of the Langevin equation. In such models, stochastic droplet trajectories are obtained by consideration of pseudorandom perturbations of the continuous flow field, i.e., turbulent eddies. The description of the perturbing force, or so-called complementary force, is generally related to Lagrangian statistics of the unresolved turbulent flow, e.g., the Lagrangian autocorrelation function of turbulent fluctuations, and is generally implemented using pseudorandom algorithms to described the random character of the eddy-droplet interactions. Among the most common of these are the discrete random walk (DRW) models first proposed by Gosman and Ioannides [39], in which droplet trajectories are perturbed by pseudorandom velocity fluctuations using discrete piecewise constant functions of time for a duration related to the characteristic eddy lifetime of

said fluctuation [113]. Much like their laminar counterparts however, implementation of stochastic Lagrangian gas-droplet models are computationally expensive in practice. As the characteristic scales of the turbulent flow field become small, or mass fraction of the droplet phase becomes large, the required frequency of the sampling of pseudorandom eddy-droplet interactions becomes increasingly large. Likewise, due to stochastic nature of these interactions, statistically accurate solutions may only be obtained by ensemble averaging of a sufficient number of realizations [125]. Consequently, while stochastic Lagrangian methods provide detailed descriptions of eddy-droplet interactions, these methods are accompanied by prohibitive computational expense in many practical engineering problems.

Alternatively to Lagrangian-based models, Eulerian approaches to turbulent gas-droplet coupling promise significantly reduced computational expense and algorithmic complexity, albeit not without also introducing caveats of their own. Specifically, in the zero-inertia limit, Eulerian formulations for eddy-droplet interactions reduce to simplifications of the theory of turbulent diffusion [110, 125]. However, as the Stokes number grows larger and dispersion becomes dominated by both diffusive and inertial turbulent transport, more generalized formulations based upon probabilistic kinetic equations are required. Where the Langevin equation is translated into a probabilistic form, generic kinetic/Fokker-Planck equations provide such Eulerian descriptions for the diffusion-inertia phenomena of eddy-droplet interactions [110, 114, 127]. Generalized, these kinetic equations for turbulent diffusion-inertia models (DIM) take the form of

$$\frac{\partial \mathcal{F}}{\partial t} + v_\alpha \frac{\partial \mathcal{F}}{\partial x_\alpha} + \frac{\partial}{\partial v_\alpha}\left(a_\alpha\right) = -\frac{1}{\tau_d}\frac{\partial \left\langle U_i' \mathcal{F}\right\rangle}{\partial v_\alpha} + \frac{D}{\tau_d^2}\frac{\partial^2 \mathcal{F}}{\partial v_\alpha \partial v_\beta}\,, \tag{6.86}$$

where U_i' is the turbulent fluid velocity fluctuation and D is a diffusion coefficient. Importantly, Equation (6.86) introduces two additional terms to the RHS of the generic collisonless-Boltzmann equation for turbulent eddy-droplet interactions, whereby the left-most term describes unresolved eddy-droplet interactions, and the right-most term describes Brownian motion due to turbulent diffusion. A few caveats however arise from the typical formulation of Equation (6.86). Specifically, the first left-most term of the RHS of Equation (6.86) describes the inherent inertial coupling resulting from unresolved

eddy-droplet correlation, which following from Zaichik, can be closed as [127]

$$-\frac{1}{\tau_d}\frac{\partial\left\langle U_i'\,\mathcal{F}\right\rangle}{\partial v_\alpha} = -\frac{1}{\tau_d}\frac{\partial}{\partial v_\alpha}\left[-\tau_d\left(\lambda_{\alpha\beta}\frac{\partial\mathcal{F}}{\partial v_\beta}+\mu_{\alpha\beta}\frac{\partial\mathcal{F}}{\partial x_\beta}\right)\right]. \tag{6.87}$$

A few remarks from Equation (6.87) are notable. Where tensors $\lambda_{\alpha\beta}$ and $\mu_{\alpha\beta}$ are related to the turbulent Reynolds stress-tensor of the unresolved turbulent flow field, the expression for Equation (6.87) more importantly introduces a new spatial flux term. Within the scope of the present work, such a term threatens the strict-hyperbolicity of the system of equations. Such a concern consequently motivates the development of a first-order, i.e., hyperbolicity maintaining, approximation to turbulent eddy-droplet interactions for the proposed two-scalar PGM. Specifically, the present work seeks to introduce a simple algebraic expression in the RHS which describes momentum and energy production based upon deterministic time-averaged eddy-droplet correlations.

Assuming all turbulence scales are fully-modelled, i.e., applying a typical Reynolds-averaged Navier-Stokes (RANS) approach [116], correlative terms may arise within the inertial gas-droplet coupling model from expansion of second-order surface-weighted velocity moments ($w = sv_iv_j$) of Equation (6.81) using Reynolds decomposition [110, 116],

$$\left\langle\frac{(U_i-v_i)}{\tau_d}\tilde{\mathcal{G}}\frac{\partial\left(sv_iv_j\right)}{\partial v_\alpha}\right\rangle = \frac{\pi}{\gamma}\left(\left\langle v_j\left(U_i-v_i\right)\tilde{\mathcal{G}}\right\rangle+\left\langle v_i\left(U_j-v_j\right)\tilde{\mathcal{G}}\right\rangle\right), \tag{6.88}$$

$$\left\langle v_j\left(U_i-v_i\right)\tilde{\mathcal{G}}\right\rangle = \left\langle\overline{v}_j\overline{U}_i\tilde{\mathcal{G}}\right\rangle+\left\langle v_j'\overline{U}_i\tilde{\mathcal{G}}\right\rangle+\left\langle v_j'U_i'\tilde{\mathcal{G}}\right\rangle+\left\langle\overline{v}_jU_i'\tilde{\mathcal{G}}\right\rangle-\left\langle v_jv_i\tilde{\mathcal{G}}\right\rangle. \tag{6.89}$$

Note, bolded overline notations refer to the ensemble-averaged quantities here onwards. Likewise, given the collisionless assumption of the proposed model, $\left\langle v_jv_i\tilde{\mathcal{G}}\right\rangle$ is not decomposed as turbulent droplet fluctuations will remain uncorrelated. Consequently, where Reynolds averaging rules apply to the moments of Equation (6.89), the remaining non-zero moments are

$$\left\langle v_j\left(U_i-v_i\right)\tilde{\mathcal{G}}\right\rangle = \left\langle\overline{v}_j\overline{U}_i\tilde{\mathcal{G}}\right\rangle+\left\langle v_j'U_i'\tilde{\mathcal{G}}\right\rangle-\left\langle\overline{v}_j\overline{v}_i\tilde{\mathcal{G}}\right\rangle, \tag{6.90}$$

$$= n\left(\overline{u}_j\overline{U}_i-\left(\overline{\Psi}_{ij}+\overline{u}_i\overline{u}_j\right)\right)+\left\langle v_j'U_i'\tilde{\mathcal{G}}\right\rangle. \tag{6.91}$$

As a result of the consideration of turbulent eddy-droplet correlations, an unresolved, or unclosed, second-order moment production term is shown to arise within the RHS of the moment-equations. Closure of Equation (6.91) may be achieved by several methods, such as gradient-closure [110], however such methods do not guarantee the hyperbolicity of the moment-equations. Instead, an argument for the closure of $\left\langle v_j' U_i' \tilde{\mathcal{G}} \right\rangle$ is proposed based upon a deterministic steady-state discrete-droplet response to turbulent eddy-droplet interactions to provide a first-order hyperbolicity maintaining algebraic expression.

6.2.2.1 Turbulent Lengthscales and Timescales

In turbulence theory, eddies can be described as local deviations, or fluctuations, of fluid from the macroscopic fluid flow [110, 125]. Generally, these fluctuations are generated by instabilities within the flow, producing vortical structures, and are observed on various macroscopic and microscopic scales. Within an Eulerian-framework, i.e., spatially-fixed reference system, eddies behave as waves and are described by the superposition of oscillatory fluctuations. Consequently, eddies are typically described by their wavenumber, k, which is associated with the vorticity of their particular scale. Specifically,

$$k = \frac{1}{\lambda} = \frac{\omega}{U}\,, \tag{6.92}$$

where λ is the eddy wavelength, ω is the eddy angular frequency, and U is the eddy velocity. Where a Reynolds decomposition is applied, the present work assumes the instantaneous flow velocity of a characteristic eddy can be expressed as a steady sinusoidal-fluctuation,

$$U_i = \overline{U}_i + U_i' \approx \overline{U}_i + \sqrt{2}\, U'_{\mathrm{rms},i}\, \sin\left(\omega\left(t + \phi\right)\right)\,, \tag{6.93}$$

with ϕ some arbitrary phase-shift and $\overline{U}_i$ the mean flow velocity. Specifically, the amplitude and frequency of the characteristic fluctuation are related to the characteristic scales of the unresolved turbulent flow. Generally, the amplitudes of turbulent fluctuations, U_i', are related to the energy spectrum contained by the spectrum of turbulent motion, whereby the characteristic amplitude of Equation (6.93) is analogous to the turbulence strength. The total energy contained within the spectrum, or so-called turbulent kinetic energy, is

obtained by integration of the energy spectrum,

$$\overline{E} = \int_0^\infty E(k)\mathrm{d}k\,, \tag{6.94}$$

where $E(k)$ is the spectral energy contained at a scale k. Of course, the turbulent kinetic energy is related to a measure of the kinetic energy of individual eddies at all scales. The turbulent kinetic energy can therefore also be expressed in terms of second-order moments of the spectral superposition of velocity fluctuations, U_i', as

$$\overline{E} = \frac{1}{2}\left\langle U_i' U_i' \right\rangle\,. \tag{6.95}$$

Again, Einstein summation notation applies. While anisotropy at inertial scales is expected, homogeneous isotropic turbulence assumptions are often proposed within the context of unresolved turbulence modelling [116]. Where homogeneous isotropic turbulence is therefore assumed, Equation (6.95) reduces to [110]

$$\overline{E} = \frac{3}{2}U_{\mathrm{rms}}'^2\,, \tag{6.96}$$

with U_{rms}' the characteristic turbulence strength, or root-mean-square turbulent velocity fluctuation.

The timescales associated to the energy containing eddies are those of the inertial range, i.e., the largest integral scales and Taylor microscale [110]. Importantly, following the energy cascade hypothesis, these energy containing timescales remain correlated to the smallest energy dissipation scale, or so-called Kolmogorov microscale [110]. Influenced by the kinematic fluid viscosity, ν, and energy dissipation rate, ε, the smallest Kolmogorov timescale defines the scale at which turbulent kinetic energy and viscous energy dissipation are in equilibrium. By dimensional analysis, it is expressed as

$$\tau_\eta = \left(\frac{\nu}{\varepsilon}\right)^{\frac{1}{2}}\,, \tag{6.97}$$

and is associated with the Kolmogorov lengthscale,

$$\eta = \left(\frac{\nu^3}{\varepsilon}\right)^{\frac{1}{4}} . \tag{6.98}$$

Note, the Kolmogorov lengthscale is the inverse of the eddy wavenumber, k_η, and as such, the Kolmogorov timescale is by definition also the inverse of the eddy frequency, ω_η. Therefore, the characteristic turbulent timescales which impart significant effects upon droplet or particulate matter are obtained by similar analysis. Many authors have proposed empirical estimates for the largest integral timescales. However, most estimates take the following generalized form [103],

$$T_{i,L} \cong C_L \frac{\overline{E}}{\varepsilon} , \tag{6.99}$$

with C_L the Lagrangian structure function constant [110]. Moreover, the subscript L importantly identifies the Lagrangian integral timescales. Defined in a Lagrangian frame of reference, the Lagrangian-based timescale is typically several order of magnitude larger than its Eulerian counterpart. The distinction thus results in significant discrepancies given either particular turbulent coupling approach. Notably however, due to the multi-scale spectral nature of turbulent fluctuations, smaller inertial sub-range timescales remain significant. Specifically, the Taylor microscale is often used to characterize the scale at which both large-scale (inertial) and small-scale (viscous) effects are observed. The Taylor timescale is generally expressed as [104]

$$\tau_\lambda = \sqrt{\frac{15\,\nu}{\varepsilon}} , \tag{6.100}$$

with its Eulerian microscale counterpart, as given by Comte-Bellot and Corrsin [12, 103], is expressed as

$$\tau_\mathcal{E} = \sqrt{\frac{6\,\nu}{\varepsilon}} . \tag{6.101}$$

Typically, the characteristic turbulence timescale used for eddy-droplet interactions is of the order of the larger integral timescales. However, some discussion on the particular choice of ω will follow in Chapter 8. Nevertheless, selection of an appropriate timescale is

required to capture turbulent eddy-droplet interactions, particularly when dealing with a distribution of droplet sizes as expected from the present two-scalar PGM.

6.2.2.2 An Approximate Turbulent Eddy-Droplet Interaction Model

Where droplets exhibit a low Stokes number, the instantaneous discrete-droplet velocity is expected to be directly correlated to the characteristic turbulent fluctuation, U', of Equation (6.93). However, where non-negligible Stokes numbers are considered, droplets begin to exhibit weaker correlations to U' for increasingly large turbulent Stokes number, St_e. Herein, the turbulent Stokes number is a dimensionless ratio of the droplet momentum response timescale, τ_d, and the characteristic turbulence timescale,

$$St_e = \tau_d \, \omega \, , \tag{6.102}$$

with ω the characteristic turbulence frequency which has units $[\mathrm{s}^{-1}]$. The droplet response in Stokes flow to a perturbing force produced by a turbulent fluctuation can be obtained analytically by solution of

$$\frac{\mathrm{d}v'}{\mathrm{d}t} = \frac{U' - v'}{\tau_d} \, , \tag{6.103}$$

where $U' = \sqrt{2} U'_{\mathrm{rms}} \sin\big(\omega(t+\phi)\big)$ from Equation (6.93). Consequently, the exact solution to the droplet velocity response is obtained as

$$\begin{aligned} v' = \exp\left(-\frac{t}{\tau_d}\right) \left(v'_0 - \frac{\sqrt{2} U'_{\mathrm{rms}}}{1 + \tau_d^2 \, \omega^2} \Big(\sin(\omega\phi) - \tau_d \, \omega \cos(\omega\phi) \Big) \right) \\ + \frac{\sqrt{2} U'_{\mathrm{rms}}}{1 + \tau_d^2 \, \omega^2} \Big(\sin\big(\omega(t+\phi)\big) - \tau_d \omega \cos\big(\omega(t+\phi)\big) \Big) \, . \end{aligned} \tag{6.104}$$

The left-most term of Equation (6.104) describes an initial transient relaxation to the steady-perturbation. In steady-state however, this term may be neglected. The steady-

state droplet response to a steady deterministic fluctuation is therefore taken as

$$\begin{aligned} v' &= \frac{\sqrt{2}U'_{\text{rms}}}{\sqrt{1+\tau_d^2\,\omega^2}}\Big(\sin\big(\omega(t+\phi)-\arctan(\tau_d\,\omega)\big)\Big)\,, \\ &= \frac{\sqrt{2}U'_{\text{rms}}}{\sqrt{1+St_e^2}}\Big(\sin\big(\omega(t+\phi)-\arctan(St_e)\big)\Big)\,. \end{aligned} \tag{6.105}$$

By inspection of Equation (6.105), one observes the amplitude response and phase-shift are, as expected, functions of the turbulent Stokes numbers. As a result, in the lower non-inertial limit, $St_e \to 0$, Equation (6.105) is shown to recover the turbulent fluctuation U'—describing complete eddy-droplet coupling. Conversely, where the turbulent Stokes number becomes large for more inertial droplets, Equation (6.105) tends to zero as the momentum response timescale dwarfs the oscillatory turbulent fluctuation timescales.

By consideration of both Equations (6.93) and (6.105), a time-averaged approximation of turbulent eddy-droplet correlation for the closure of $\left\langle v'_j U'_i \tilde{\mathcal{G}} \right\rangle$ is taken as

$$\begin{aligned} \left\langle v'_j U'_i \tilde{\mathcal{G}} \right\rangle = \Bigg\langle \frac{\omega}{2\,\pi} \int_0^{\frac{2\pi}{\omega}} \Bigg(&\frac{2\,U'^2_{\text{rms}}}{\sqrt{1+\tau_d^2\,\omega^2}}\Big(\sin\big(\omega(t+\phi)\big)\Big) \\ &\Big(\sin\big(\omega(t+\phi)-\arctan(\tau_d\,\omega)\big)\Big)\Bigg)\mathrm{d}t\,\delta_{ji}\tilde{\mathcal{G}}\Bigg\rangle\,, \end{aligned} \tag{6.106}$$

$$= \left\langle \frac{U'^2_{\text{rms}}}{1+\tau_d^2\,\omega^2}\delta_{ji}\tilde{\mathcal{G}} \right\rangle\,. \tag{6.107}$$

Note, the kronecker delta, δ_{ji}, is introduced by virtue of the previous isotropic turbulence assumption, i.e., fluctuations U'_i and v'_j are uncorrelated. Unfortunetaly, similar to challenges faced during the implementation of the Stefan-Fuch droplet evaporation model of Section 6.1.2, the moments of Equation (6.107) cannot be integrated in closed-form. Consequently, an approximate function is again required to close the RHS of the moment-equations.

In order to close Equation (6.107), an approximate function is defined such that

$$\mathcal{H}_e \approx \frac{1}{1+\tau_d^2\,\omega^2} = \frac{1}{1+d^4\,\gamma^2\,\omega^2}\,. \tag{6.108}$$

Here, an expression for the proposed approximate function is derived by the approximate recovery of the first-order derivative of the exact function. Specifically, given the first-order derivative of the exact function,

$$\frac{\mathrm{d}}{\mathrm{d}d}\left(\frac{1}{1+d^2\,\gamma^2\,\omega^2}\right) = -\frac{4\,d^3\,\gamma^2\,\omega^2}{\left(1+d^4\,\gamma^2\,\omega^2\right)^2}\,, \tag{6.109}$$

an approximate derivative for $\mathcal{H}_e$ is proposed by graphical analysis as

$$\frac{\mathrm{d}\mathcal{H}_e}{\mathrm{d}d} = -C\,\sqrt{\gamma\,\omega}\,\exp\left(-\pi\,\left(\ln\left(d\right)+\ln\left(\sqrt{\gamma\,\omega}\right)\right)^2\right)\,, \tag{6.110}$$

with C an undefined scaling coefficient. Demonstrative plots of both Equations (6.109) and (6.110) are illustrated in Figure 6.3. Where $\mathcal{H}_e$ is known to be equal to one in the zero-inertia limit, the approximate function is obtained by integration as

$$\begin{aligned}\mathcal{H}_e &= 1-\int_{-\infty}^{\ln(d)}\left(C\sqrt{\gamma\,\omega}\exp\left(\ln(d)\right)\exp\left(-\pi\left(\ln\left(d\right)+\ln\left(\sqrt{\gamma\,\omega}\right)\right)^2\right)\right)\mathrm{d}\ln(d)\,,\\ &= 1-\frac{C\exp\left((4\pi)^{-1}\right)}{2}\left(1+\operatorname{erf}\left(\sqrt{\pi}\left(\ln(d)+\ln\left(\sqrt{\gamma\,\omega}\right)\right)+\frac{1}{2\sqrt{\pi}}\right)\right)\,.\end{aligned} \tag{6.111}$$

By simple inspection, the scaling coefficient is selected as $C=\exp\left(-(4\pi)^{-1}\right)$ to ensure $\mathcal{H}_e$ asymptotes to zero in the infinite limit. Oddly, by graphical comparison, best agreement between the exact and approximate function is observed by dropping the additional constant term within the error function, as shown in Figure 6.4. As a result, the approximate function $\mathcal{H}_e$ is instead taken as

$$\mathcal{H}_e = \frac{1}{2}\operatorname{erfc}\left(\sqrt{\pi}\,\left(\ln(d)+\ln\left(\sqrt{\gamma\,\omega}\right)\right)\right)\,. \tag{6.112}$$

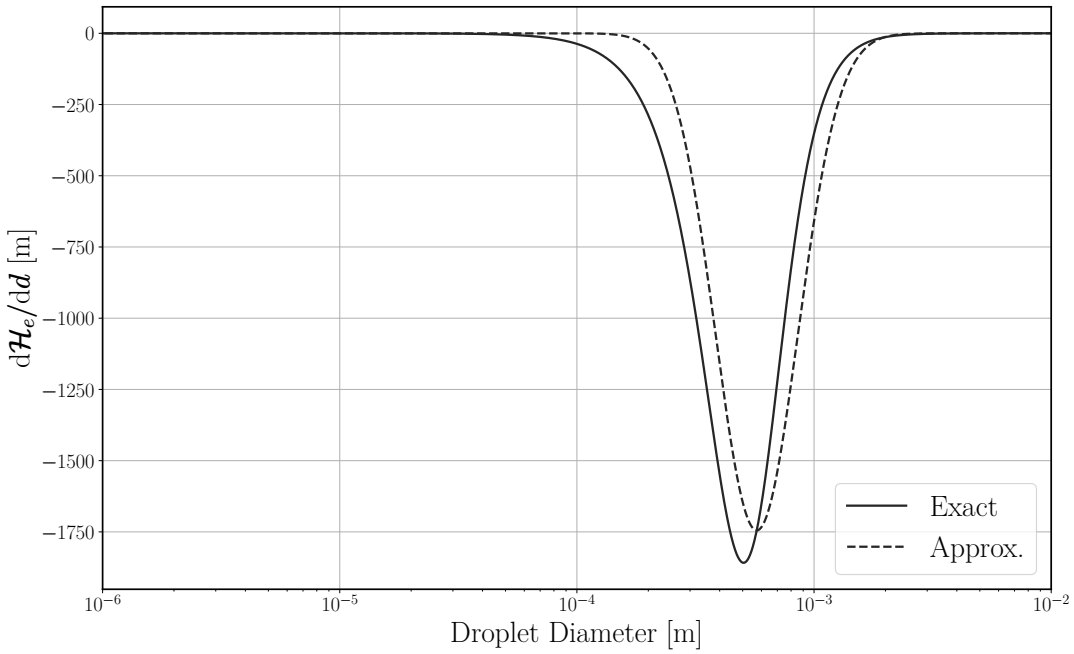

(a) Spray of water in dry air at $\mathbf{293\,K}$ and $\mathbf{1\ atm}$ in low-frequency turbulence $\omega = \mathbf{1}\,\mathrm{rad\,s^{-1}}$.

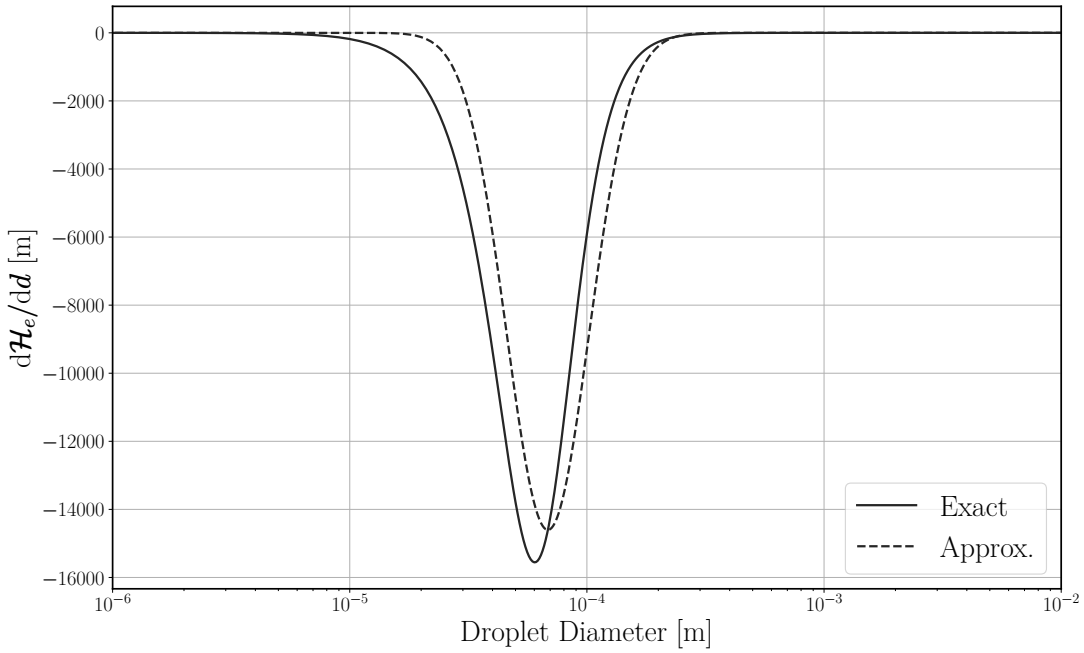

(b) Spray of n-heptane in dry air at $\mathbf{593\,K}$ and $\mathbf{607\,950\,Pa}$ in high-frequency turbulence $\omega = \mathbf{100}\,\mathrm{rad\,s^{-1}}$.

Figure 6.3: Comparison of exact and approximate derivatives of $\mathcal{H}_e$ for two sprays in different turbulence timescales with a unitary scaling coefficient.

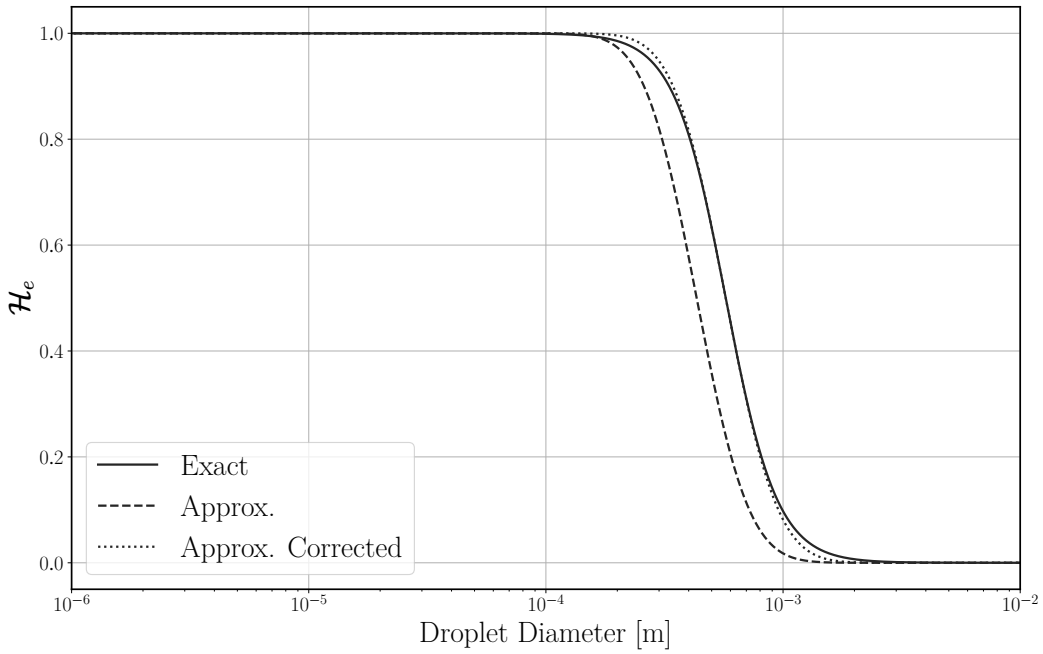

(a) Spray of water in dry air at $\mathbf{293\,K}$ and $\mathbf{1\ atm}$ in low-frequency turbulence $\omega = \mathbf{1}\,\mathrm{rad\,s^{-1}}$.

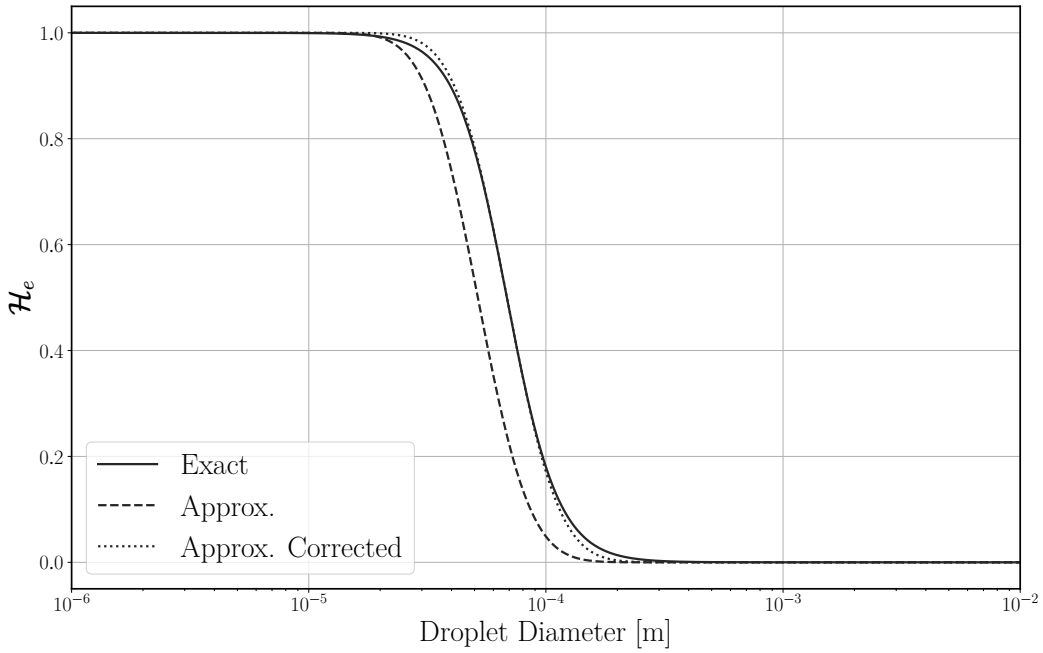

(b) Spray of n-heptane in dry air at $\mathbf{593\,K}$ and $\mathbf{607\,950\,Pa}$ in high-frequency turbulence $\omega = \mathbf{100}\,\mathrm{rad\,s^{-1}}$.

Figure 6.4: Comparison of exact and approximate functions of $\mathcal{H}_e$ for two sprays in different turbulence timescales with a scaling coefficient of $\exp\left(-(4\pi)^{-1}\right)$.

Finally, substitution of $\mathcal{H}_e$ into Equation (6.107) allows for the closed-form integration of the yet unclosed moment. Specifically, using the identity derived by Ng and Geller [74], Equation (6.107) is obtained as

$$\left\langle v_j' U_i' \tilde{\mathcal{G}} \right\rangle \approx \left\langle U_{\text{rms}}'^2 \, \mathcal{H}_e \, \delta_{ji} \tilde{\mathcal{G}} \right\rangle = \frac{n \, U_{\text{rms}}'^2}{2} \, \text{erfc} \left(\frac{\sqrt{\pi} \, \left(\mu + \ln \left(\sqrt{\gamma \, \omega} \right) \right)}{\sqrt{1 + 2 \Psi_{dd} \, \gamma \, \omega}} \right) \, \delta_{ji} \, . \tag{6.113}$$

Effectively, upon examination of the moment-expression contained within the complementary error function of Equation (6.113), the proposed expression describes eddy-droplet coupling as a function of the mean droplet size distribution lengthscale and the dimensional group, $\gamma \, \omega$. In fact, the group $\mu + \ln \left(\sqrt{\gamma \, \omega} \right)$ is analogous to the turbulent Stokes number, whereby strong turbulent eddy-droplet coupling is observed at values ≤ 0 and becomes weaker for increasingly large positive values. Importantly, the proposed expression describes turbulent eddy-droplet coupling without high-order spatial derivatives as desired to maintain the hyperbolicity of the two-scalar PGM moment-equations. Rather, the proposed turbulent coupling model remains a first-order algebraic expression using solely moments of the phase-space density distribution function and local characteristic turbulence quantities. Recalling the inertial gas-droplet coupling moment-equations provided in Section 6.2.1, the turbulent Reynolds-averaged inertial coupling model finally yields

$$\overline{\overline{S}}_{v_i}^{(1)} = \frac{\pi \, n}{\gamma} \, \left(\overline{U}_i - \overline{u}_i \right) + a_{g_i} \, \overline{s} \, , \tag{6.114}$$

$$\begin{aligned} \overline{\overline{S}}_{v_{ij}}^{(4)} = \frac{\pi \, n}{\gamma} \, & \left[\overline{U}_i \, \overline{u}_j + \overline{U}_j \, \overline{u}_i + U_{\text{rms}}'^2 \, \text{erfc} \left(\frac{\sqrt{\pi} \, \left(\mu + \ln \left(\sqrt{\gamma \, \omega} \right) \right)}{\sqrt{1 + 2 \Psi_{dd} \, \gamma \, \omega}} \right) \, \delta_{ij} - 2 \left(\overline{\Psi}_{ij} + \overline{u}_i \, \overline{u}_j \right) \right] \\ & + 2 \, a_{g_i} \, \overline{s} \, \overline{\overline{u}}_i \, , \end{aligned} \tag{6.115}$$

$$\overline{\overline{S}}_{v_{id}}^{(7)} = \frac{\pi \, n}{\gamma} \, \left[\overline{U}_i \, \mu - \left(\overline{\overline{\Psi}}_{id} + \overline{u}_i \mu \right) \right] + a_{g_i} \, \overline{s} \, \bar{\mu} \, , \tag{6.116}$$

$$\overline{\overline{S}}_{v_{iT}}^{(8)} = \frac{\pi \, n}{\gamma} \, \left[\overline{U}_i \, \theta - \left(\overline{\overline{\Psi}}_{iT} + \overline{u}_i \theta \right) \right] + a_{g_i} \, \overline{s} \, \bar{\theta} \, . \tag{6.117}$$

6.2.2.3 An Approximate Turbulent Droplet Drift Correction

The turbulent inertial gas-droplet model described by Equations (6.114) to (6.117) notably does not include a turbulent droplet drift correction. As many authors have explored, turbulent eddy-droplet interactions produce a drift phenomena, whereby droplets maintain inertia on timescales larger than the expected momentum response timescale [76, 80, 100, 125–127]. As suggested by Pai and Subramaniam [80], a modified droplet momentum response time representative of multiscale gas- and eddy-droplet interactions may be proposed to account for droplet drift. Within the present work, a modified mean momentum response timescale is proposed as

$$\tau_m = \mathcal{X}\,\tau_G + (1-\mathcal{X})\,\omega^{-1}\,, \tag{6.118}$$

where the mean momentum response time is

$$\tau_G = n\left\langle \frac{1}{\tau_d}\,\tilde{\mathcal{G}} \right\rangle^{-1} = \gamma \exp\left(2\left(\Psi_{dd}+\mu\right)\right)\,, \tag{6.119}$$

and the blending function is taken as

$$\mathcal{X} = \frac{1}{2}\,\mathrm{erfc}\left(\ln\left(\tau_G\,\omega\right)^{-1}\right)\,. \tag{6.120}$$

By definition of Equation (6.118), a modified γ is similarly obtained,

$$\gamma_m = \mathcal{X}\gamma + (1-\mathcal{X})\,\omega^{-1}\exp\left(-2\left(\Psi_{dd}+\mu\right)\right)\,, \tag{6.121}$$

which may then be substituted into Equations (6.114) to (6.117). The proposed correction is a preliminary attempt at providing an accurate account of multiscale inertial interactions within the two-scalar PGM. The proposed correction is based upon a comparative analysis of droplet momentum response and turbulence timescales. Specifically, where the turbulent Stokes number is small, i.e., $\tau_d \ll \omega^{-1}$, the modified momentum response timescale is skewed towards the characteristic eddy timescale as droplets are expected to remain coupled to eddies for the entire duration of their lifetime. When the inverse occurs and large

turbulent Stokes numbers are observed, i.e., $\tau_d \gg \omega^{-1}$, droplets are expected to maintain their inertia independently of small turbulent eddy interactions due to reduced eddy-droplet coupling – therefore τ_m is skewed towards τ_g. Furthermore, preliminary analyses conducted herein have demonstrated a dependency on the effective characteristic turbulence timescale and the Reynolds number of the flow. These dependencies are further discussed in Chapter 8. Nevertheless, future work is required for the derivation and analysis of a more robust turbulent droplet drift correction term.

Chapter 7

Numerical Methods and Algorithms

The cumulative information of Chapters 3 to 6 complete the comprehensive presentation of modelling efforts completed within the scope of the present work for the development of the two-scalar PGM for evaporating sprays. The following sections of this work focuses on numerical implementation of the proposed model, including analyses and discussion of results regarding the proposed modelling assumptions and approximations. Specifically, the subsections which follow suit will discuss the numerical methods and algorithms for three solvers—along with numerical algorithms required for their implementation. These include two zero-dimensional, i.e., space-homogeneous, solvers for both the surface-weighted two-scalar PGM equations, and a Monte-Carlo solver for integration of the discrete-droplet equations of the underlying droplet distribution function. Lastly, numerical methods for the implementation of a large-scale highly-parallelized two-dimensional finite-volume solver for the two-scalar PGM shall be presented.

7.1 Space-Homogeneous Moment and Monte-Carlo Solvers

Development of a Monte-Carlo solver for the discrete-droplet equations is motivated by the necessity of comparative analysis and validation against the modelled moment-equations. As discussed, moment-closure of the system of moment equations derived from the Williams-Boltzmann kinetic equation restricts the form of the underlying phase-space density distribution function, $\tilde{\mathcal{G}}$. The resulting system of moment-equations thus provides a description for the evolution of the restrained system of moments which satisfy the assumed underlying density distribution. Where the choice of extended phase-space variables for the closure-problem is unwise, the obtained moment-equations are not inherently guaranteed to recover the evolution of the underlying phase-density obtained by solution of the unrestrained kinetic equation—particularly in the transient-state. As such, agreement between the moment-equations and kinetic equation may be significantly poor, whereby steady-state moments may also markedly disagree. Numerical integration of the discrete-droplet equations is therefore performed to model the evolution of the underlying droplet distribution function and to thus provide an important measure of the error produced by the proposed moment approximation. As such, the implementation of a Monte-Carlo framework for the description of the discrete-droplet equations is selected to provide an accurate reference for the assessment and validation of the proposed moment-model.

The framework for both the space-homogeneous moment and Monte-Carlo solvers was discussed in Section 5.1.2, and is briefly summarized for extension to the complete two-scalar PGM model. Notably, given the space-homogeneity, spatial derivatives of both the moment-equations and Williams-Boltzmann equation are omitted. Consequently, both the system of moment-equations and discrete-droplet equations are therefore reduced to significantly simpler ordinary differential equations (ODEs) in time. Regarding the moment-equation implementation, the one-dimensional RHS moment-equations of the two-scalar PGM for evaporating sprays are obtained by combination of the thermodynamic and inertial gas-droplet coupling equations presented in Chapter 6. Due to their prohibitively complex notation, these equations are not summarized here—the reader is encouraged to review the equations separately. Nevertheless, the one-dimensional space-homogeneous reduction

of the aforementioned equations yields a system of ten stiff time-coupled ODEs for the evolution of the moments of $\tilde{\mathcal{G}}$. As for the Monte-Carlo implementation, the one-dimensional governing equations of the Monte-Carlo solver for the evolution of discrete-droplets are

$$\frac{\mathrm{d}v}{\mathrm{d}t} = \frac{(U-v)}{\tau_d} + \frac{\rho_\ell - \rho_g}{\rho_g}\, g\,, \tag{7.1}$$

$$\frac{\mathrm{d}d}{\mathrm{d}t} = -\frac{2\, k_m\, Sh_0}{c_{p,\ell}\, c_{p,m}\, d} \ln\left(1 + B_M\right), \tag{7.2}$$

$$\frac{\mathrm{d}T}{\mathrm{d}t} = \frac{6\, k_m\, Nu_0}{c_{p,\ell}\, \rho_\ell\, d^2} \ln(1 + B_M) \left(\frac{T_\infty - T}{B_M} - \frac{\Delta h}{c_{p,m}} \right). \tag{7.3}$$

A few remarks regarding Equations (7.1) to (7.3): contributions of turbulent perturbations are neglected, whereby validation of the proposed turbulence coupling approximation will be discussed in Section 8.2. Moreover, the current numerical implementation does not include thermodynamic tables for interpolative estimates for temperature-dependant quantities required for the Stefan-Fuchs droplet evaporation model. Implementation of such features to allow comparison against experimental laboratory results remains the subject of future work.

Again, comparative moments of the Monte-Carlo solution are obtained by evaluating moments of the discrete-droplet distribution using the discrete traditional definition of statistical moments. Where the one-dimensional two-scalar PGM reduces to a system of ten moment-equations, the equivalent discrete formulation for the Monte-Carlo surface-weighted moments for an initial number density n_0 using m_0 initial droplet samples are,

$$\bar{s} = \pi\, n_0\, \frac{\sum_{i=1}^{m} d_i^2}{m_0}\,, \tag{7.4}$$

$$\bar{s}\bar{u} = \pi\, n_0\, \frac{\sum_{i=1}^{m} d_i^2\, v_i}{m_0}\,, \tag{7.5}$$

$$\bar{s}\bar{\mu} = \pi\, n_0\, \frac{\sum_{i=1}^{m} d_i^2\, \ln(d_i)}{m_0}\,, \tag{7.6}$$

$$\bar{s}\bar{\theta} = \pi\, n_0\, \frac{\sum_{i=1}^{m} d_i^2\, T_i}{m_0}\,, \tag{7.7}$$

$$\tag{7.8}$$

$$\bar{s}(\bar{\Psi}_{xx} + \bar{u}^2) = \pi\, n_0\, \frac{\sum_{i=1}^{m} d_i^2\, v_i^2}{m_0}\,, \tag{7.9}$$

$$\bar{s}(\bar{\Psi}_{dd} + \bar{\mu}^2) = \pi\, n_0\, \frac{\sum_{i=1}^{m} d_i^2\, (\ln(d_i))^2}{m_0}\,, \tag{7.10}$$

$$\bar{s}(\bar{\Psi}_{TT} + \bar{\theta}^2) = \pi\, n_0\, \frac{\sum_{i=1}^{m} d_i^2\, T_i^2}{m_0}\,, \tag{7.11}$$

$$\bar{s}(\bar{\Psi}_{id} + \bar{u}\bar{\mu}) = \pi\, n_0\, \frac{\sum_{i=1}^{m} d_i^2\, v_i \ln(d_i)}{m_0}\,, \tag{7.12}$$

$$\bar{s}(\bar{\Psi}_{iT} + \bar{u}\bar{\theta}) = \pi\, n_0\, \frac{\sum_{i=1}^{m} d_i^2\, v_i T_i}{m_0}\,, \tag{7.13}$$

$$\bar{s}(\bar{\Psi}_{dT} + \bar{\mu}\bar{\theta}) = \pi\, n_0\, \frac{\sum_{i=1}^{m} d_i^2\, \ln(d_i) T_i}{m_0}\,. \tag{7.14}$$

with m the number of sampled droplets with a non-zero size. Importantly, the associated unweighted moments may also be evaluated by simple omission of the $\pi\, d_i^2$ pre-multiplication within the above equations. Furthermore, the initialization of the Monte-Carlo solver is achieved by a similar algorithm to that presented in Section 5.1.2. Rather, given a particular set of moments of $\tilde{\mathcal{G}}_0$ defining the initial condition of the two-scalar PGM, initial conditions for n droplets are produced by sampling the initial probability density distribution function, $\tilde{g}_0$, using a Mersenne-twister pseudo-random number generator algorithm [64]. Moreover, given the pseudorandom nature of the Monte-Carlo solver, ensemble averaging of a sufficient number of realizations is performed to yield a statistically converged result. Finally, solutions of both the system of moment-ODEs and Monte-Carlo discrete-droplet equations are numerically integrated using the well-known Runge-Kutta 4^{th}-order explicit time-marching scheme. Where computational efficiency is neglected for the present space-homogeneous analysis, over-resolution and stability of both solvers is guaranteed by a sufficiently small fixed time-step, while outputs for both solvers are outputted at significantly longer time intervals.

7.2 Two-Dimensional Finite-Volume Solver

Beyond the preliminary one-dimensional analyses, model validation efforts are followed by implementation of the proposed model into a two-dimensional large-scale and highly-parallelized Godunov-type finite-volume framework [49]. While extension of the implementation using a higher-order discontinuous Galerkin-Hancock method remains the subject of future work, the current implementation provides a first-order accurate numerical scheme for the preliminary investigations performed within the scope of the present work. Specifically, the implementation consists of a first-order finite-volume scheme using a point-implicit time-marching scheme with spatial fluxes treated explicitly using the Harten-Lax-van Leer (HLL) approximate Riemann solver [43]. Conversely, treatment of the locally stiff RHS of the proposed moment-equations is performed implicitly using a numerically optimized implicit-Euler scheme. In two-dimensions, the resulting spacetime discretization of the moment-equations, integrated over one computational cell, is expressed as

$$\bar{\boldsymbol{U}}^{n+1} = \bar{\boldsymbol{U}}^{n} + \frac{\Delta t}{A} \sum_{j}^{\text{faces}} \bar{\boldsymbol{F}}_j \cdot \hat{n}_j \, \ell_j + \Delta t \, \bar{\boldsymbol{S}}^{n+1} \,, \tag{7.15}$$

with A the cell area, and ℓ_j the length of the jth intercellular interface. Importantly, given the Godunov-type spatial discretization, the terms of Equation (7.15) also represent cell-average quantities of the surface-weighted conserved solution vector, $\bar{\boldsymbol{U}}$, flux dyad, $\bar{\boldsymbol{F}}$, and source term, $\bar{\boldsymbol{S}}$. Given the elegant Eigenstructure of the proposed model, treatment of the numerical flux dyad within the present implementation is straightforward. In fact, given as the minimum and maximum Eigenvalues of any arbitrary moment-state is guaranteed real-valued, as demonstrated in Section 5.2, numerical fluxes are easily evaluated using the HLL approximate Riemann solver with a high-degree of numerical stability. Unfortunately, due to the strong non-linearity and inter-moment coupling of the locally stiff source terms, stability sought by the implicit treatment of the RHS of the proposed model proves addedly more difficult to guarantee. As the source terms for the presented equations do not uncouple, no analytical solution for the treatment of the implicit-Euler time-marching scheme has been derived. Instead, solution of the implicit-Euler step-size is performed numerically using a high-dimensional Newton-Raphson method by leveraging numerical automatic differentiation libraries [53].

7.2.1 Treatment of Realizability Limits

As discussed in Section 3.4, for significant deviations from local equilibrium, realizability of the moment-state of the maximum-entropy closure hierarchy may not be inherently guaranteed. While these concerns have traditionally been notably graver for higher-order moment-closures, encounters with the realizable limits of the maximum-entropy closure do occur within the proposed two-scalar PGM model. Specifically, small errors produced by numerical precision limits and the implemented numerical scheme are sufficiently large to produce deviations from the limits of the realizable space. As a result, stability of the numerical implementation depends strongly on both the detection and correction of the inadvertent admission of non-realizable moment states, whereby the set of closure-coefficients may be artificially restricted to yield a physically realizable phase density without introduction of uncontrolled errors.

Realizability of the maximum-entropy closure hierarchy is primarily concerned with (i) the admission of strictly-positive phase densities, $n > 0$, and (ii) the admission of a symmetric positive-definite, variance-covariance tensor, $\mathbf{\Psi}_{\tilde{i}\tilde{j}}$. Detection of an unrealizable moment-state thus follows by ensuring both the above requirements are satisfied by an arbitrary moment-state. Such a verification can be achieved using a two-step verification algorithm which is described herein. The first-step of realizability verification is trivial, and allows to quickly verify both requirements (i) and (ii) are satisfied. Specifically, by simple inspection of all necessarily strictly-positive closure-coefficients, both requirements (i) and (ii) may be tested for validity, whereby verifying the phase-space number density, n, is non-negative is sufficient to robustly satisfy (i), and verifying the diagonal entries of the variance-covariance tensor are non-zero and positive is sufficient to partially satisfy (ii). Rather, where (i) is sufficiently satisfied by the trivial test of the first-step, demonstrating diagonal entries of $\mathbf{\Psi}_{\tilde{i}\tilde{j}}$ are strictly-positive is not sufficient to demonstrate positive-definiteness. To verify $\mathbf{\Psi}_{\tilde{i}\tilde{j}}$ is strictly symmetric positive-definite, a spectral decomposition is performed, such that

$$\mathbf{\Psi}_{\tilde{i}\tilde{k}}\, S_{\tilde{k}\tilde{j}} = S_{\tilde{i}\tilde{k}}\, \mathbf{\Lambda}_{\tilde{k}\tilde{j}}\,, \tag{7.16}$$

with $S_{\tilde{i}\tilde{j}}$ the matrix of right Eigenvectors of the real symmetric $\mathbf{\Psi}_{\tilde{i}\tilde{j}}$ tensor, and $\mathbf{\Lambda}_{\tilde{i}\tilde{j}}$ a

diagonal tensor of the Eigenvalues of $\Psi_{\tilde{i}\tilde{j}}$. Explicitly,

$$\Lambda_{\tilde{i}\tilde{j}} = \mathrm{diag}(\lambda_{\tilde{i}})\,, \tag{7.17}$$

where the Eigenvalue vector, $\lambda_{\tilde{i}}$, contains the principle stresses of the $\Psi_{\tilde{i}\tilde{j}}$ tensor. Finally, positive-definiteness is demonstrated if the entries of $\lambda_{\tilde{i}}$ are strictly-positive; else $\Psi_{\tilde{i}\tilde{j}}$ is shown to yield a non-realizable phase density distribution.

Correction of requirement (i) is achieved by simply increasing the local number density to an ad-hoc defined tolerance, ε. Where evaporation is prominent, encounters with this realizability limit may occur, particularly in regions distant from droplet injection regions. However, where the ill-conditionedness of the implicit-Euler source term treatment produces non-negligible errors in the converged moment-state, requirement (i) may also be violated by numerical errors in regions of stiff evaporation. Nevertheless, the artificial introduction of near-zero droplet density, ε, is justified in such regions as near-zero droplets should be expected from the process of evaporation. Correction of a violation of requirement (ii) is not as simple however. Within the proposed model, encounters with singular variance-covariance tensors is inherently expected from the physics described by both the proposed thermodynamic and inertial gas-droplet coupling models. Rather, where droplets settle to steady-sate, velocity distributions are expected to collapse onto infinitesimal lines of the extended velocity-size phase-space as the droplet distribution reaches its settling state. Likewise, a similar collapse of temperature distributions is inherently expected as droplets relax to the wet-bulb temperature—describing a size-temperature phase-space distribution collapsed onto an infinitesimal line of constant temperature. Coupled with aforementioned numerical errors, the subsequent realizability correction algorithm for requirement (ii) must be arduously robust such to ensure stability in both transient and steady-state regions of the computational domain.

Within the works of Marchildon [61], an algorithm based upon spectral decomposition was suggested. However, the suggested algorithm contained no scaling to control the introduction of energy by correction of the principle stresses of $\Psi_{\tilde{i}\tilde{j}}$. Instead, the present work implements a spectral decomposition algorithm proposed by Rebonato and Jäckel [83] which simply introduces a normalization of the reconstructed positive-definite variance-

covariance tensor such that the resulting tensor is not energy increasing where possible. Recalling the formulation of Equation (7.17), the algorithm follows by defining a modified diagonal Eigenvalue tensor,

$$\Lambda'_{\tilde{i}\tilde{j}} = \mathrm{diag}\left(\begin{cases} \lambda_{\tilde{i}} & \lambda_{\tilde{i}} > 0 \\ \varepsilon & \text{else} \end{cases}\right), \tag{7.18}$$

which allows for the definition of

$$B'_{\tilde{i}\tilde{j}} = S_{\tilde{i}\tilde{k}}\sqrt{\Lambda'_{\tilde{k}\tilde{j}}}\,. \tag{7.19}$$

By construction, an unscaled positive-definite variance-covariance tensor can then be taken as

$$C'_{\tilde{i}\tilde{j}} = B'_{\tilde{i}\tilde{k}}B'^{\mathrm{T}}_{\tilde{k}\tilde{j}}\,. \tag{7.20}$$

The resulting tensor $C'_{\tilde{i}\tilde{j}}$ is however not guaranteed to conserve the trace of the original non-realizable moment-state, $\mathbf{\Psi}_{\tilde{i}\tilde{i}}$, which is related to the total variance. In order to yield a conservative reconstruction where possible, i.e., where the diagonal entries of $\mathbf{\Psi}_{\tilde{i}\tilde{j}}$ are strictly-positive, a diagonal scaling tensor, $\mathcal{T}_{\tilde{i}\tilde{j}}$ is built by the following process,

$$\mathcal{N}_{\tilde{i}\tilde{j}} = \mathrm{diag}\left(\begin{cases} \mathbf{\Psi}_{\tilde{k}\tilde{j}} & \mathbf{\Psi}_{\tilde{k}\tilde{j}} > \varepsilon \\ C'_{\tilde{k}\tilde{j}} & \text{else} \end{cases}\right), \tag{7.21}$$

$$\mathcal{D}_{\tilde{i}\tilde{j}} = \mathrm{diag}\left(C'_{\tilde{k}\tilde{j}}\right), \tag{7.22}$$

$$\mathcal{T}_{\tilde{i}\tilde{j}} = \mathcal{N}_{\tilde{i}\tilde{k}}\,\mathcal{D}^{-1}_{\tilde{k}\tilde{j}} \tag{7.23}$$

such that a scaled positive-definite variance-covariance follows as

$$B_{\tilde{i}\tilde{j}} = \sqrt{\mathcal{T}_{\tilde{i}\tilde{k}}}\,S_{\tilde{k}\tilde{\ell}}\sqrt{\Lambda'_{\tilde{\ell}\tilde{j}}}\,, \tag{7.24}$$

$$\mathbf{\Psi}'_{\tilde{i}\tilde{j}} = B_{\tilde{i}\tilde{k}}\,B^{\mathrm{T}}_{\tilde{k}\tilde{j}}\,. \tag{7.25}$$

As a result, where the diagonal entries of $\mathbf{\Psi}_{\tilde{i}\tilde{j}}$ are strictly-positive, one is guaranteed by construction $\mathbf{\Psi}'_{\tilde{i}\tilde{i}} = \mathbf{\Psi}_{\tilde{i}\tilde{i}}$ and $\mathbf{\Psi}'_{\tilde{i}\tilde{j}}$ is a symmetric positive-definite tensor. Finally, $\mathbf{\Psi}'_{\tilde{i}\tilde{j}}$ may be substituted for $\mathbf{\Psi}_{\tilde{i}\tilde{j}}$ to satisfy requirement (ii) of the realizability of the moment-state.

Chapter 8

Numerical Results

8.1 One-Dimensional Space-homogeneous Sprays

As mentioned within the motivation of the present work, the objectives herein involved the development of a novel Eulerian-based spray model for a variety of industrial, energy conversion and medical processes. To this end, the following section describes preliminary investigations into the performance of the proposed two-scalar PGM for evaporating sprays for two illustrative spray problems; namely a typical viral bio-aerosol problem, and a simplified fuel injection problem. The primary goal of these analyses consists of a quantitative assessment of the proposed moment-approximation, i.e., identifying and quantifying modelling errors produced by the proposed moment-closure. As described in Section 7.1, significant errors may arise from the inherent choice of the extended phase-space dimensions of the proposed moment-closure. Specifically, where non-linear relationships between the selected extended phase-space dimensions develop, the underlying phase-space density described by the system of moment-equations may disagree with the Lagrangian-based discrete solution equivalent. As such, preliminary assessments of such errors are performed by consideration of the one-dimensional space-homogeneous formulation for the proposed moment model, with quantitative comparisons obtained by utilization of the developed Monte-Carlo solver described in Section 7.1.

8.1.1 Room-Air Bio-Aerosol Sedimentation Problem

8.1.1.1 Description and Numerical Methods

The modelling of human coughs is of particular interest for the study of epidemiology and the transmission of respirable pathogens. As these respiratory events are often approximated as pure liquid aerosol water sprays [6, 113, 120], such bio-aerosol problems provide the inspiration for the following analysis, whereby the proposed two-scalar PGM for evaporating sprays shall be utilized for the modelling of a typical evaporating human cough. Specifically, the problem considered herein considers a droplet sedimentation problem for a liquid water spray into a quiescent dry room-air environment, i.e., 0% relative humidity at an ambient temperature of $293.15\,\mathrm{K}$ and $1\ \mathrm{atm}$. A summary of relevant physical and thermodynamic properties of air and water utilized for this analysis are provided in Tables 8.1 and 8.2. As for the liquid droplet phase, droplet distribution data is obtained by

Table 8.1: Summary of constant physical and thermodynamic properties of air at $293.15\,\mathrm{K}$ and $1\ \mathrm{atm}$ ($0\%\,\mathrm{RH}$).

Property	Value
Molar Mass, M_g $[\mathrm{kg\,mol^{-1}}]$	2.896×10^{-2}
Density, ρ_g $[\mathrm{kg\,m^{-3}}]$	1.204
Dynamic Viscosity, μ_g $[\mathrm{m^2\,s^{-1}}]$	1.813×10^{-5}
Thermal Conductivity, k_g $[\mathrm{W\,m^{-1}\,K^{-1}}]$	2.638×10^{-2}
Specific Heat Capacity, $c_{p,g}$ $[\mathrm{J\,kg^{-1}\,K^{-1}}]$	1.004×10^{3}

review of available literature. For the present case, the initial condition is adapted from human cough data reviewed by Nicas *et al.* [2, 75] which reports the typical geometric mean diameter of ejected cough droplets as $14\,\mu\mathrm{m}$ with a geometric standard deviation of 2.6. A summary of the initial moment state is provided in Table 8.3. The numerical solution for the proposed problem is time-marched with a fixed time-step of $10 \times 10^{-6}\,\mathrm{s}$ until a final time of $6\,\mathrm{s}$. For the purpose of comparative analysis, outputs of the moment-states of both the moment model and Monte-Carlo solution are provided at $10 \times 10^{-3}\,\mathrm{s}$ intervals in both surface-weighted conserved and unweighted primitive moment forms. These results

Table 8.2: Summary of constant physical and thermodynamic properties of water with boiling temperature referenced at $375.51\,\mathrm{K}$ and $1\ \mathrm{atm}$.

Property	Value
Molar Mass, M_v $[\mathrm{kg\,mol^{-1}}]$	1.802×10^{-2}
Density, ρ_v $[\mathrm{kg\,m^{-3}}]$	9.999×10^{2}
Thermal Conductivity, k_v $[\mathrm{W\,m^{-1}\,K^{-1}}]$	0.598
Specific Heat Capacity, $c_{p,v}$ $[\mathrm{J\,kg^{-1}\,K^{-1}}]$	4.187×10^{3}
Latent Heat of Vaporization, Δh $[\mathrm{J\,kg^{-1}}]$	2.256×10^{6}

are illustrated in Figure 8.1. Moreover, such to ensure the sufficient statistical convergence of the Monte-Carlo solution, a total of 100 realizations, each with 2.0×10^6 particles, are averaged to yield the converged moment-state evolution. Lastly, qualitative illustrations of the underlying extended phase-space density distributions are also illustrated at various time intervals in Figures 8.2 and 8.3.

8.1.1.2 Results

Given the large size distribution of water droplets during an arbitrary respiratory event, complete evaporation of the produced bio-aerosol is expected to occur on timescales significantly larger than the median droplet lifetime. Consequently, for such problems, small aerosol droplets quickly evaporate to describe a sharp initial loss of droplets which is attenuated as the largest droplets solely remain. As shown in Figure 8.1(a), the described behaviour is properly captured by both the moment-model and Monte-Carlo solution, whereby the moment-model provides great recovery of both the surface-density and number density moments of the discrete droplet solution. Defining a time-based root-mean-square relative error (RMSRE) as [20, 42, 112]

$$\mathrm{RMSRE} = \sqrt{\frac{1}{N}\sum_{i=1}^{N}\left(\frac{Y_i - \hat{Y}_i}{Y_i}\right)^2}\,, \tag{8.1}$$

Table 8.3: Moments of a typical human cough droplet distribution function for a room-air bio-aerosol sedimentation problem.

Moment	Value
Number Density, n $[\mathrm{m}^{-3}]$	2.0×10^6
Average Velocity, u_x $[\mathrm{m\,s}^{-1}]$	0.0
Average $\ln(d)$, μ	$\ln(14 \times 10^{-6})$
Average Temperature, θ $[\mathrm{K}]$	308.15
Velocity Variance, Ψ_{xx} $[\mathrm{m^2\,s^{-2}}]$	0.1
$\ln(d)$ Variance, Ψ_{dd}	$(\ln(2.6))^2$
Temperature Variance, Ψ_{TT} $[\mathrm{K^2}]$	0.15
Velocity-$\ln(d)$ Co-variance, Ψ_{xd} $[\mathrm{m\,s}^{-1}]$	0.0
Velocity-Temperature Co-variance, Ψ_{xT} $[\mathrm{m\,K\,s}^{-1}]$	0.0
$\ln(d)$-Temperature Co-variance, Ψ_{dT} $[\mathrm{K}]$	0.0

where Y_i is the Monte-Carlo solution and $\hat{Y}_i$ the moment-model prediction for N outputs at times t_i, the RMSRE for the zeroth-order moments are indeed 8.22% and 9.45%. Here, the time-based RMSRE provides a dimensionless measure of the mean relative L2-type error incurred over the entire solution. Importantly, the RMSRE will identify errors committed during the transient-state of the solution. However, where the magnitude of the moment is large and the transient change remains small, the RMSRE may not provide a representative measure of the error. As such, a normalized root-mean-square error (NRMSE) is also defined as

$$\mathrm{NRMSE} = \frac{\sqrt{\frac{1}{N}\sum_{i=1}^{N}\left(Y_i - \hat{Y}_i\right)^2}}{|Y_i^{\max} - Y_i^{\min}|}\,, \tag{8.2}$$

which provides a dimensionless error normalized over the relative range of expected values. For the zeroth-order moments, these are comparatively both 3.08% and 0.98% for the surface and number densities, respectively. A summary of all RMSREs and NRMSEs are provided in Table 8.4.

Table 8.4: Summary of root-mean-square relative error (RMSRE) and normalized root-mean-square error (NRMSE) between the moment-model and Monte-Carlo solutions evaluated over time for a typical dry (0% RH) room-air (293.15 K at 1 atm) bio-aerosol spray.

Moment	Surface-Weighted Conserved			Unweighted Primitive		
	RMSRE	NRMSE	NQSSE	RMSRE	NRMSE	NQSSE
Zeroth-Order	8.24%	3.08%	4.44%	9.45%	0.98%	0.16%
First-Order Velocity	50.26%	47.16%	40.27%	18.46%	13.83%	24.80%
First-Order Size	7.30%	2.48%	3.53%	1.07%	6.48%	8.72%
First-Order Temperature	8.28%	2.71%	3.90%	0.07%	0.68%	$< 0.01\%$
Second-Order Velocity	92.00%	61.05%	92.95%	50.06%	27.04%	48.55%
Second-Order Size	6.38%	2.00%	2.78%	14.22%	26.92%	31.78%
Second-Order Temperature	8.23%	2.41%	3.43%	143.53%	5.16%	$< 0.01\%$
Second-Order Velocity-Size	46.57%	43.66%	35.00%	19.50%	12.61%	21.60%
Second-Order Velocity-Temperature	50.31%	47.20%	40.26%	112.56%	46.82%	0.04%
Second-Order Size-Temperature	7.30%	2.18%	3.11%	194.28%	6.82%	$< 0.01\%$

With regards to temperature related moments, both first- and second-order moments of Figures 8.1(c) and 8.1(g), the moment-model is shown to well-recover the discrete Monte-Carlo solution. Naturally, for such bio-aersol problems, the droplet heat-up time is several orders of magnitude smaller than the characteristic lifetimes of the droplets. Likewise, recalling the proposed Stefan-Fuchs approximation for these conditions from Figure 6.2(a), errors within the considered regime are expectedly small. In fact, both the RMSRE and NRMSE of the mean temperature moment, θ, are $\leq 0.68\%$. However, while the surface-weighted temperature-variance density errors are relatively small (i.e., $\leq 8.28\%$), the RMSRE of the temperature-variance, Ψ_{TT}, is large—indicating significant initial transient error. Referring to the $\ln(d)$-T phase-space density plots provided in Figures 8.3(a) to 8.3(c), this error is shown to arise from an inability to capture non-linear deformations of the phase-space density distribution function, whereby a Gaussian distribution in $\ln(d)$-T phase-space is incapable of capturing the transient asymmetry as small droplets quickly

reach the wet-bulb temperature and larger droplets have yet to heat-up. At $0.005\,\mathrm{s}$ specifically, while the moment-approximation is centered at the expected mean temperature, θ, the distribution is shown to effectively undershoot the expected wet-bulb temperature in order to conserve both size- and temperature-variance. Conversely, the discrete Monte-Carlo solution admits a sharp discontinuity in temperature distributions as droplets settle to the wet-bulb temperature without undershooting. Notably however, once the heat-up period is complete, the moment-approximation is shown to accurately recover the expected size-temperature distribution where all droplets have reached the wet-bulb temperature independent of size. The timescales of the transient error is nevertheless small as compared to the larger timescales at which size moments evolve. As such, the impact of such initial errors are negligible for a room-air bio-aerosol problem.

Next, inspection of the first-order size moments of Figure 8.1(c) reveals good initial agreement of the both surface-weighted conserved (left) and unweighted primitive moments (right), however the moment-model and Monte-Carlo solutions are shown to slightly diverge once the bulk of droplets has evaporated. Specifically, assuming the solution has reached a Stefan-Fuchs steady-state, the normalized quasi-steady-state error (NQSSE) provides a dimensionless error describing the disagreement between the moment-model and Monte-Carlo solution at the quasi-steady-state. It is computed as

$$\mathrm{NQSSE} = \frac{Y_N - \hat{Y}_N}{|Y_i^{\max} - Y_i^{\min}|}\,, \tag{8.3}$$

where N is the final measured output. While the previously considered unweighted primitive zeroth- and first-order moments have been described by a NQSSE $\leq 0.16\%$, the NQSSE of the unweighted primitive first-order size moment is 8.72%, which indicates the moment-model produces a relatively significant error in quasi-steady-state as compared to the discrete droplet solution. This error is amplified further with regard to the second-order size-variance, Ψ_{dd}, of Figure 8.1(f) where a significant under-prediction of size-variance is obtained using the moment-model. A summary of all NQSSEs are also provided in Table 8.4. These results suggest a transient error is committed by restriction of the underlying extended phase-density distribution during evaporation which produces an erroneous quasi-steady-state size-distribution to develop. However, as shown in the

provided surface-weighted conserved moments, these errors become increasingly small as they become weighted by the asymptotically decreasing surface density. Hence, it should be expected that while the unweighted primitive size moment errors will increase, these errors will only be observed in near zero density regions of an arbitrary solution field, therefore effectively providing negligible contributions to moment-states in high droplet density regions of the solution.

Finally, the reader is invited to turn their attention to the more significant errors observed for all velocity related moments of both first- and second-order, including covariances. Regarding the first-order moments of Figure 8.1(b), a considerable underprediction of surface-weighted momentum density is seen to quickly develop, producing an RMSRE of $\mathbf{50.26\%}$. Likewise, the unweighted primitive moment (the mean velocity), u_x, is also shown to also diverge from the discrete droplet solution, yielding an RMSRE of $\mathbf{18.83\%}$. With regard the second-order velocity-variance moments, larger errors are also observed—as large as an NQSSE of $\mathbf{92.95\%}$. The resulting velocity moment errors obtained using logarithm-size PGMs for sedimentation (i.e., particle settling) problems have however already previously been explored by both Forgues *et al.* and Marchildon [26, 61]. As was specifically demonstrated by Marchildon, these errors arise from the well-known linear relationship between the droplet surface and terminal velocity in Stokes flow. In order for a PGM to capture the correct settling velocity-size phase-space density distribution, it has been shown one must assume a normal surface distribution rather than a lognormal diameter distribution. Where a normal surface distribution distribution is considered, the v-s phase-space Gaussian distribution becomes capable of accommodating the expected linear distribution of settling velocities which develop as a function of surface. As illustrated in the Monte-Carlo solution of Figures 8.2(a) to 8.2(c) however, the settling velocity-size phase-space density distribution adopts a curvilinear shape plotted in v-$\ln(d)$ phase-space. Again, given the assumed Gaussian distribution within v-$\ln(d)$ phase-space, the proposed moment-model is incapable of capturing the correct curvilinear and asymmetric distribution. Instead, the moments are restricted such to provide an approximate fit but they do not recover the correct settling moment-state. Naturally, as the size-variance becomes increasingly monodispersed however, the proposed moment-closure does recover the exact solution for settling droplet distribution, i.e., as the length of the curvilinear

distribution becomes small, it may be linearized and accurately described by the proposed linear distribution. Importantly, velocity-size co-variance produces spatial size-segregation of droplet distributions where spatial fluxes are considered. Consequently, aerodynamically produced velocity-size co-variance is expected to disperse initially local polydispersed distributions into a spatially distributed locally monodispersed distributions. As a result, while an initial error is expected, size-segregation of droplets is expected allow for the recovery of droplet sedimentation problems—as was shown by Marchildon [61]. Consequently, while the present analysis has identified the erroneous behaviour of the proposed moment-closure within an academic space-homogeneous context, such large errors are not expected for higher-dimensional and practical problems. As such, the attractive mathematical and numerical properties of the proposed logarithm-based size closure are expected to significantly outweigh the marginal accuracy improvements of normally distributed surface closures for practical sedimentation problems.

In summary, the proposed two-scalar PGM for evaporating sprays has been shown to yield reasonable agreement against an equivalent Lagrangian-based solution for an arbitrary bio-aerosol sedimentation problem typical of a human cough. The moment-model was specifically demonstrated to accurately recover the stiff loss of droplets and exactly recover the quasi-steady-state temperature distribution resulting from transient droplet cool-down. Furthermore, while slight disagreements were observed in the evolution of the droplet size distribution, these were shown to expected only develop in negligible low-density regions of large timescale problems. Lastly, large errors were identified within the predicted velocity moments as a result of droplet settling whereby the proposed moment-closure was shown not provide an accurate approximation for settling velocity-size phase-space density distributions. These particularly large disagreements had however already been identified and discussed as part of previous PGM investigations [26, 61], and therefore are not explicitly a result of newly modelled thermodynamic and physical phenomena. Consequently, to both demonstrate the versatility of the proposed model and to isolate errors produced by the moment approximation evaporating sprays, a second problem is analyzed as part of the present investigations and is discussed in the following section.

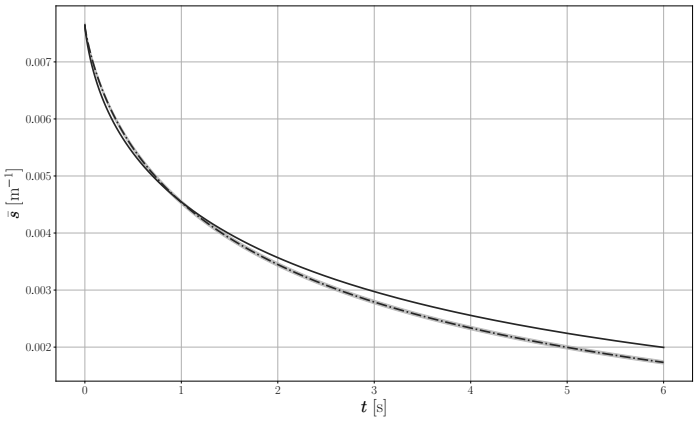

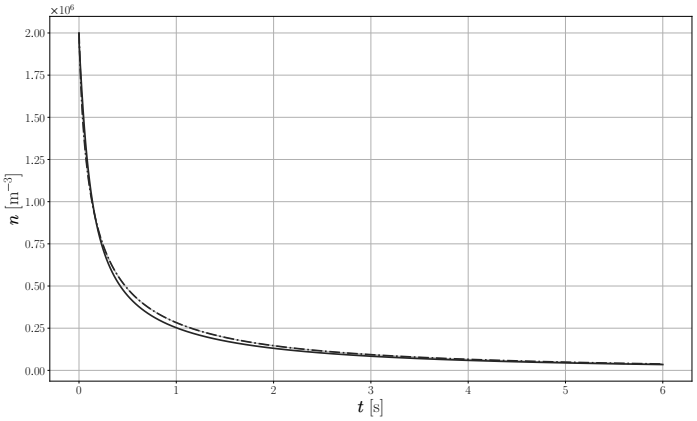

(a) Zeroth-order moments.

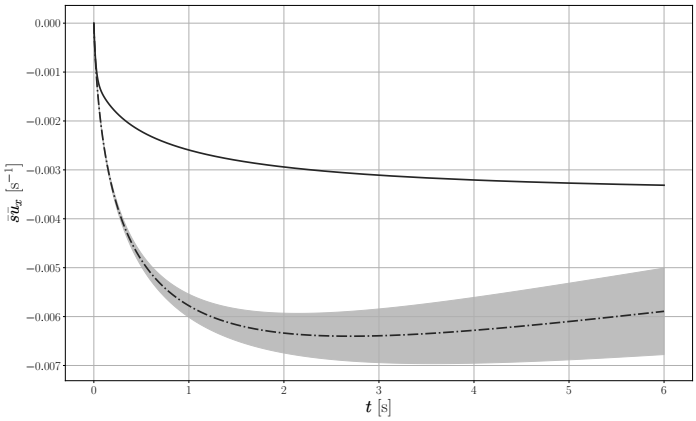

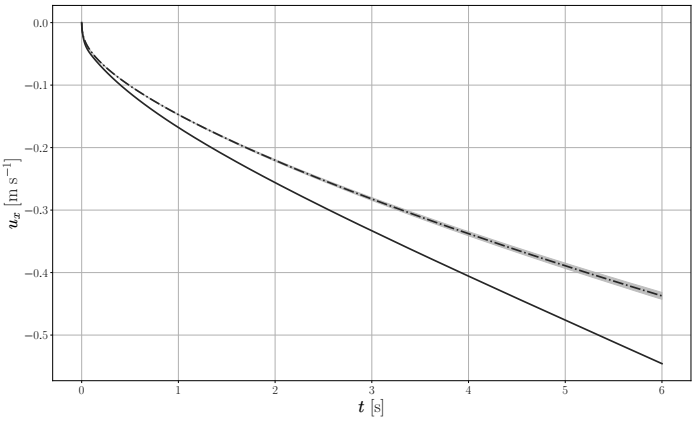

(b) First-order velocity moments.

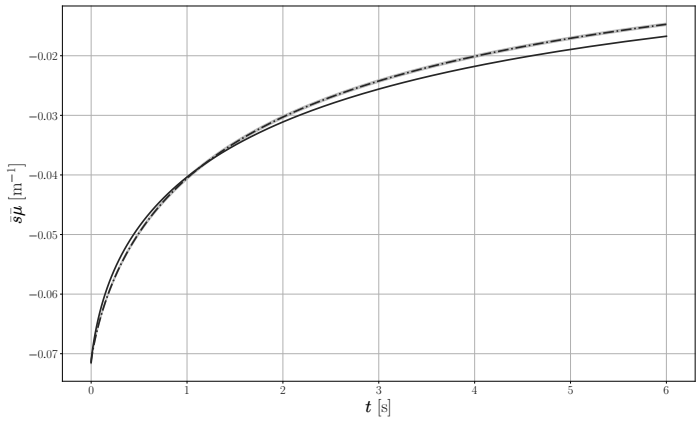

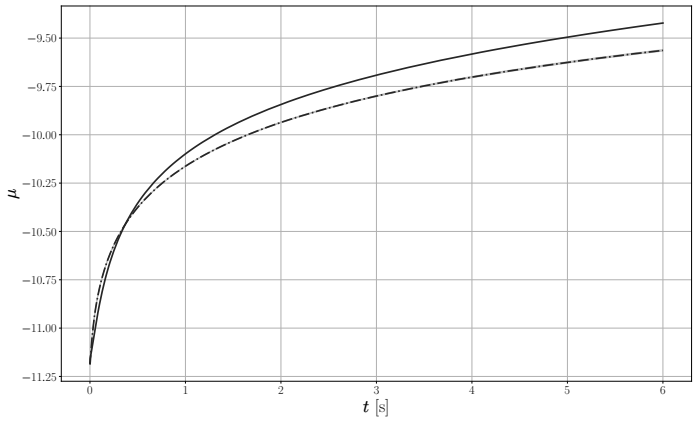

(c) First-order size moments.

Figure 8.1: Comparison of surface-weighted moment-model (solid) against Monte-Carlo solution (dashed) for a typical dry (0% RH) room-air (293.15 K at 1 atm) bio-aerosol spray. Moments presented in both surface-weighted conserved (left) and unweighted primitive (right) forms. One standard deviation certainty interval of Monte-Carlo solution represented by shaded area.

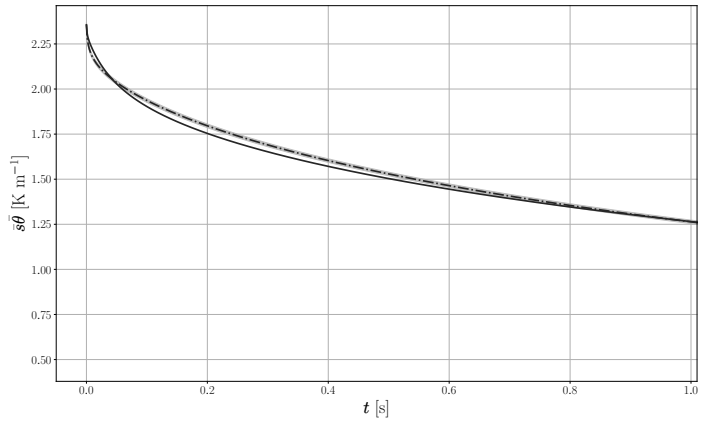

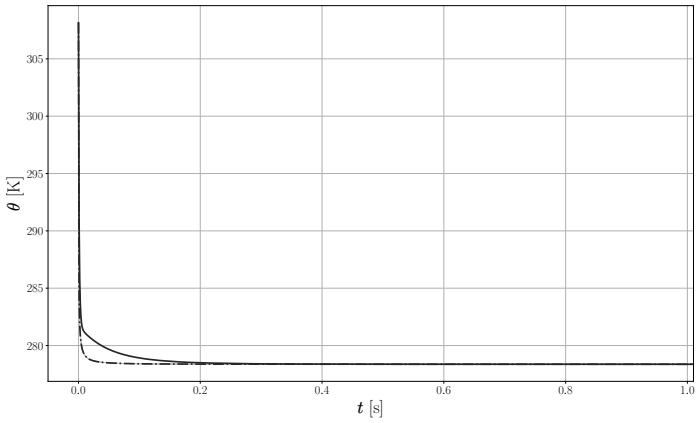

(d) First-order temperature moments.

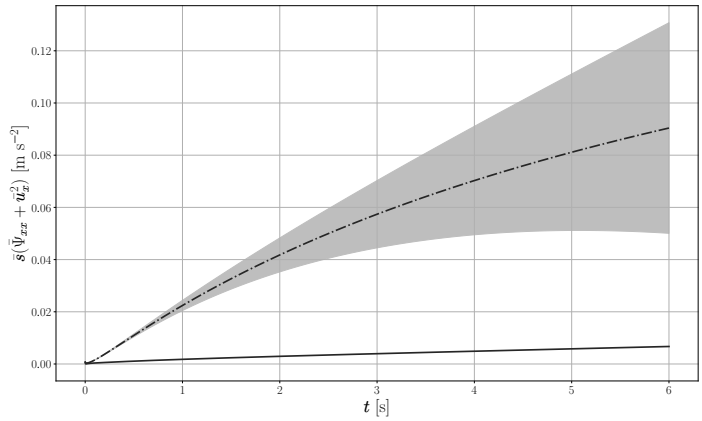

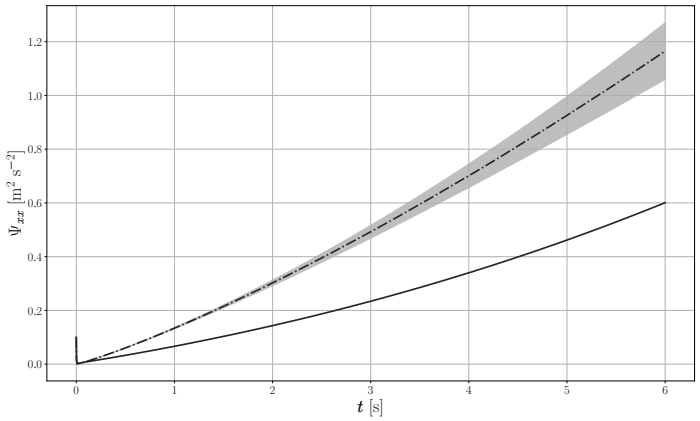

(e) Second-order velocity moments.

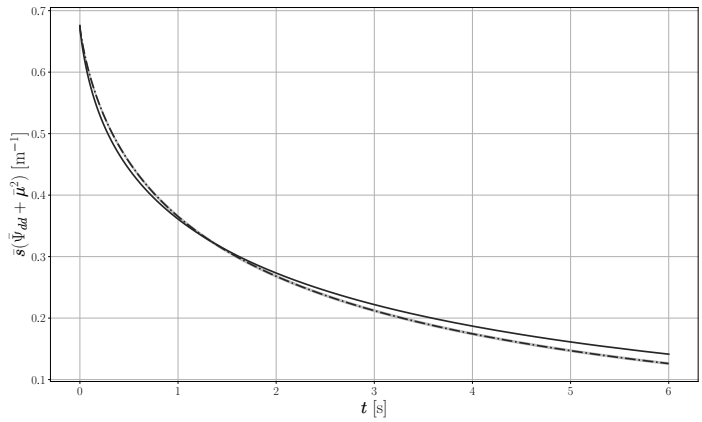

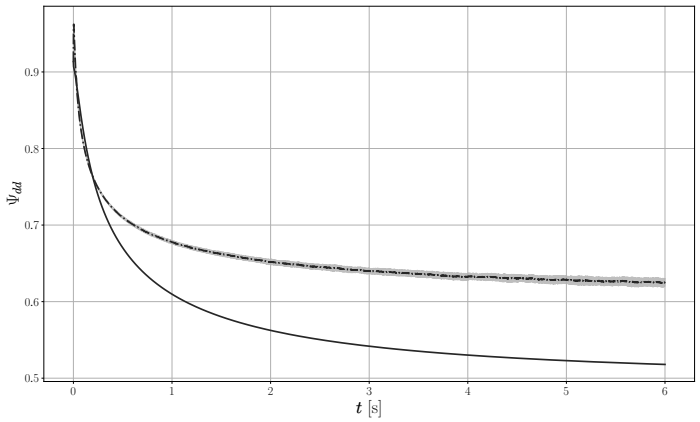

(f) Second-order size moments.

Figure 8.1: Comparison of surface-weighted moment-model (solid) against Monte-Carlo solution (dashed) for a typical dry (0% RH) room-air (293.15 K at 1 atm) bio-aerosol spray. Moments presented in both surface-weighted conserved (left) and unweighted primitive (right) forms. One standard deviation certainty interval of Monte-Carlo solution represented by shaded area.

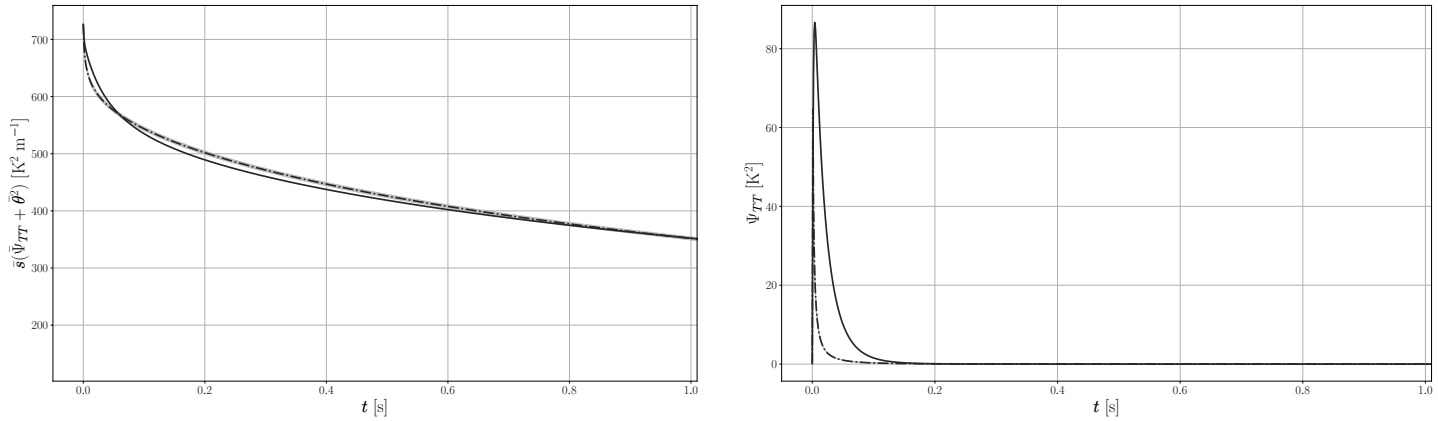

(g) Second-order temperature moments.

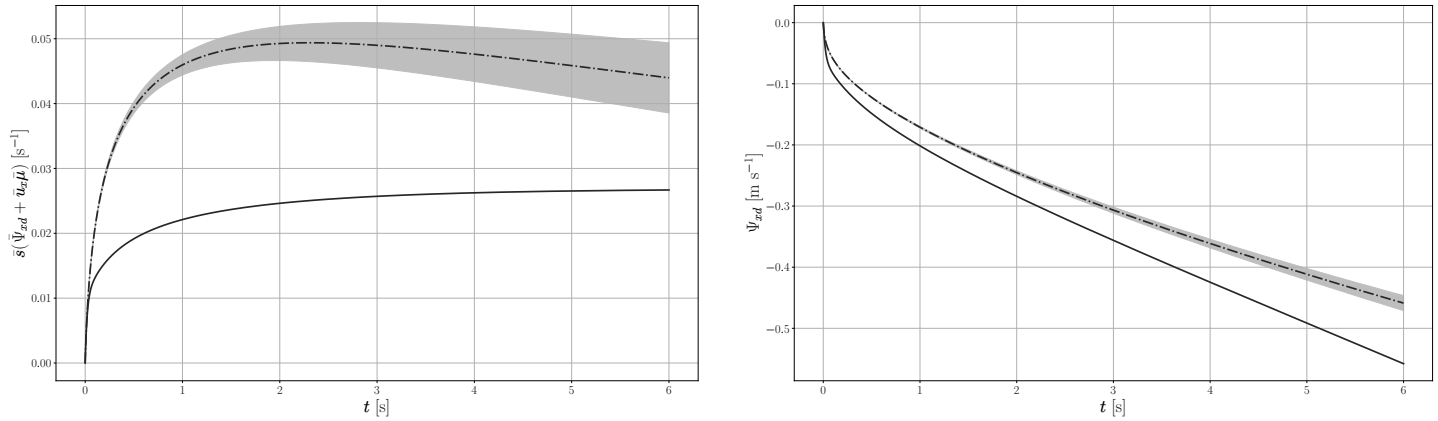

(h) Second-order velocity-size moments.

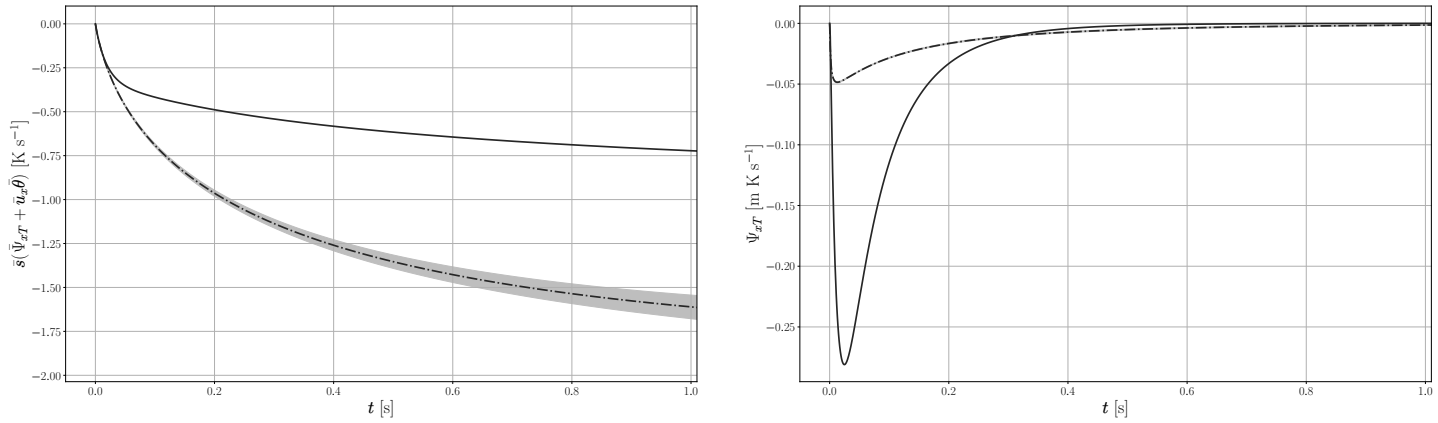

(i) Second-order velocity-temperature moments.

Figure 8.1: Comparison of surface-weighted moment-model (solid) against Monte-Carlo solution (dashed) for a typical dry (0% RH) room-air (293.15 K at 1 atm) bio-aerosol spray. Moments presented in both surface-weighted conserved (left) and unweighted primitive (right) forms. One standard deviation certainty interval of Monte-Carlo solution represented by shaded area.

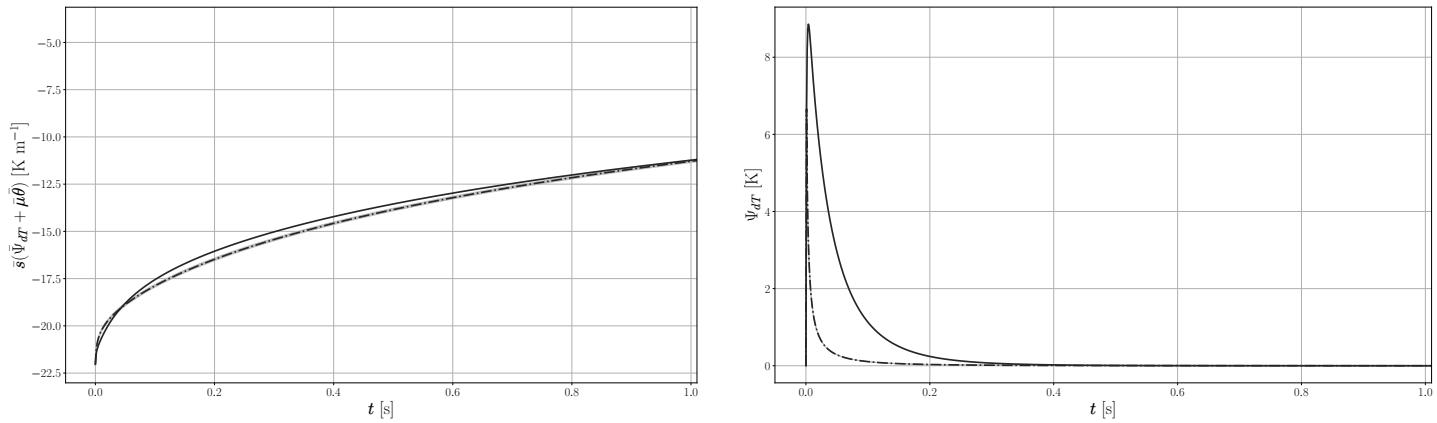

(j) Second-order size-temperature moments.

Figure 8.1: Comparison of surface-weighted moment-model (solid) against Monte-Carlo solution (dashed) for a typical dry (0% RH) room-air (293.15 K at 1 atm) bio-aerosol spray. Moments presented in both surface-weighted conserved (left) and unweighted primitive (right) forms. One standard deviation certainty interval of Monte-Carlo solution represented by shaded area.

8.1.2 n-Heptane Fuel-Injection Problem

8.1.2.1 Problem Description

Following the droplet sedimentation problem of Section 8.1.1, a second problem is proposed to examine the behaviour and accuracy of the developed moment-model for a typical fuel-injection problem. Where the previous problem treated relatively slow evaporation rates at room-air conditions, cases of fuel-injection are notably characterized by significantly stiffer evaporation rates due to strong convective effects and markedly hotter temperatures. Based upon n-heptane fuel-spray analyses conducted by Moon *et al.* [72], the proposed problem treats an n-heptane spray injected at high Stokes number into moving hot pressurized air, i.e., dry (0% RH) air at 593.15 K and 607 950 Pa with mean velocity $\overline{U} = 1\,\mathrm{m\,s^{-1}}$. Tables of the associated physical and thermodynamic properties of air and n-heptane for these conditions are provided in Tables 8.5 and 8.6. Furthermore, according to measurements cited therein, a mean geometric diameter of roughly 18 µm with a geometric standard deviation of 1.326 may be expected from a direct-injection slit injector—a summary of the initial moment state is provided in Table 8.7. Importantly, the described droplet size distribution is significantly more narrow than the previously considered human cough case. As a result, in combination with the increased vaporization rates, timescales for the evolution of the moment-state are expectedly much shorter, whereby the droplet heat-up therefore becomes non-negligible. The presently considered problem therefore provides a practical case for which the significance of the errors produced by the approximate Stefan-Fuchs droplet evaporation model may be observed.

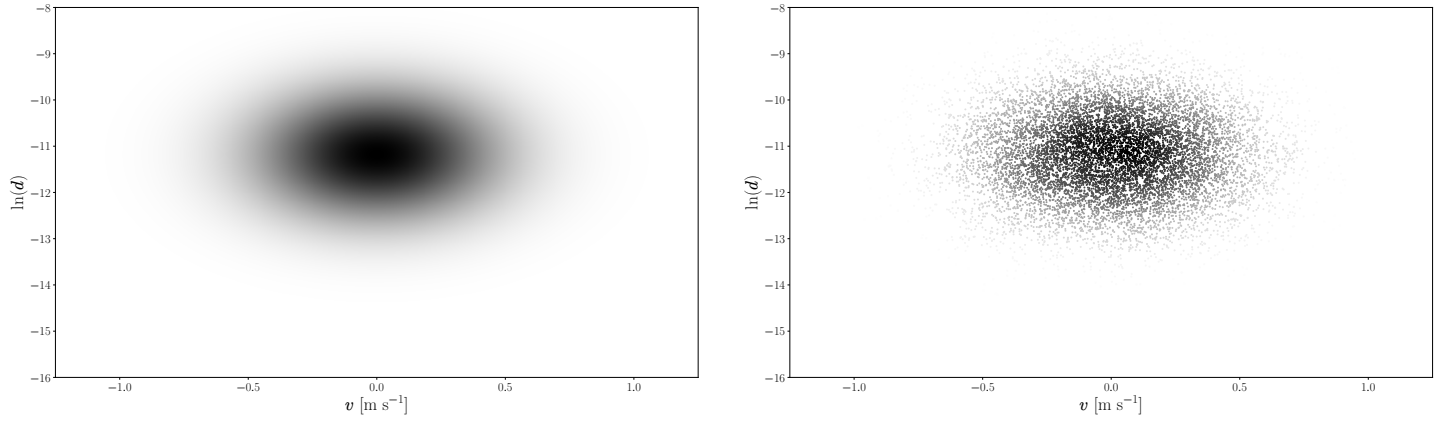

(a) $t = 0\,\mathrm{s}$

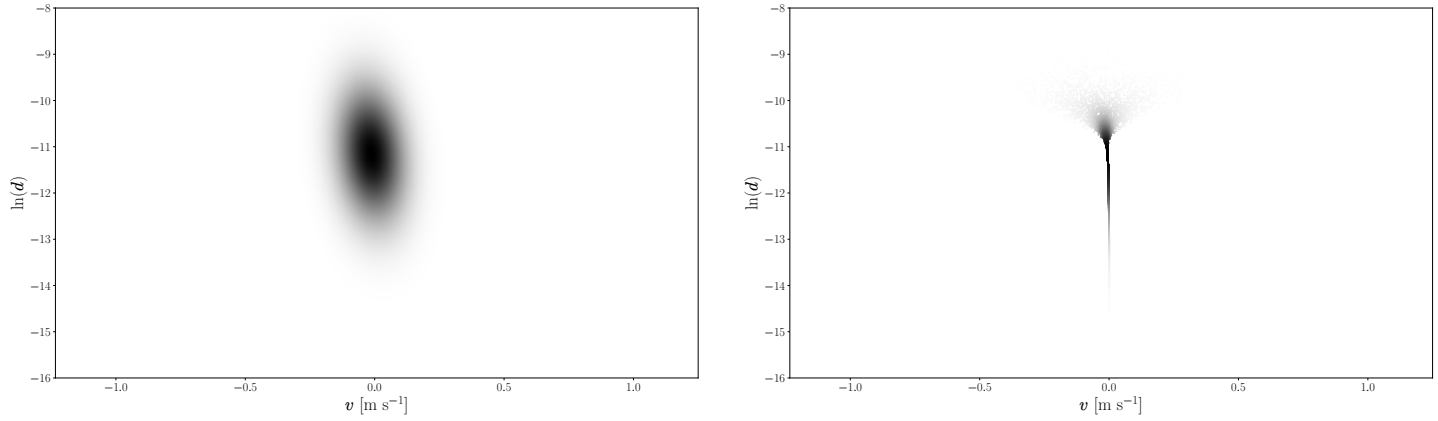

(b) $t = 0.005\,\mathrm{s}$

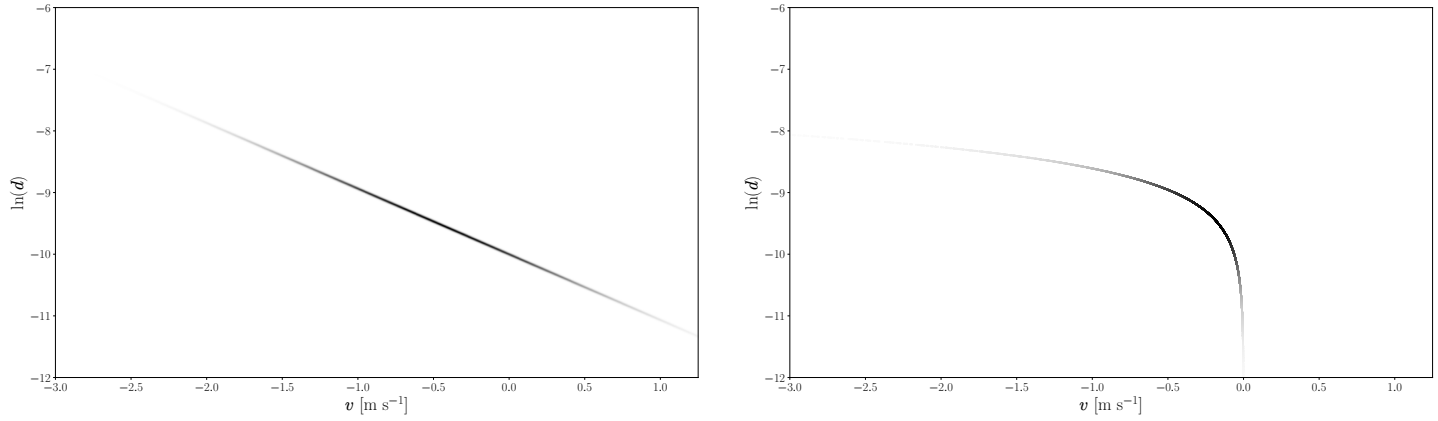

(c) $t = 5.0\,\mathrm{s}$

Figure 8.2: Comparison of density plots in v-$\ln(d)$ phase-space of $\tilde{\mathcal{G}}$ (left) and Monte-Carlo solution (right) for a typical dry ($0\%\,\mathrm{RH}$) room-air ($293.15\,\mathrm{K}$ at $1\ \mathrm{atm}$) bio-aerosol spray.

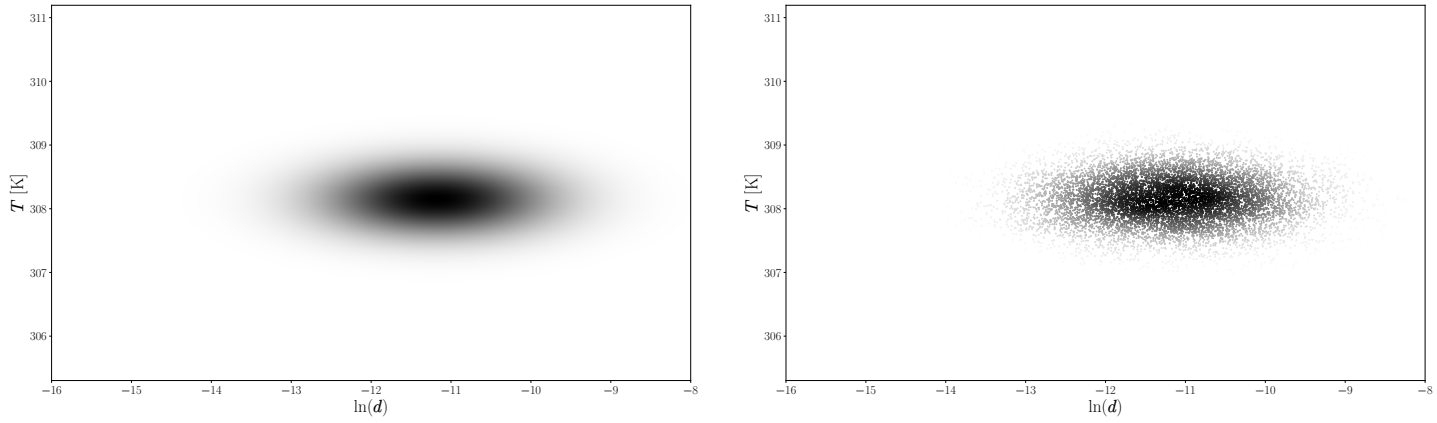

(a) $t = 0\,\mathrm{s}$

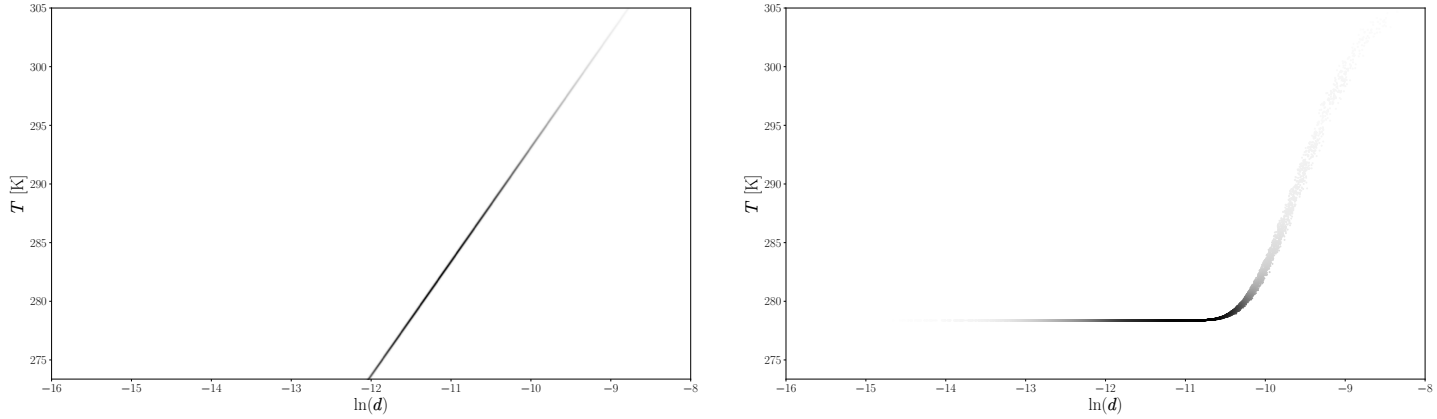

(b) $t = 0.005\,\mathrm{s}$

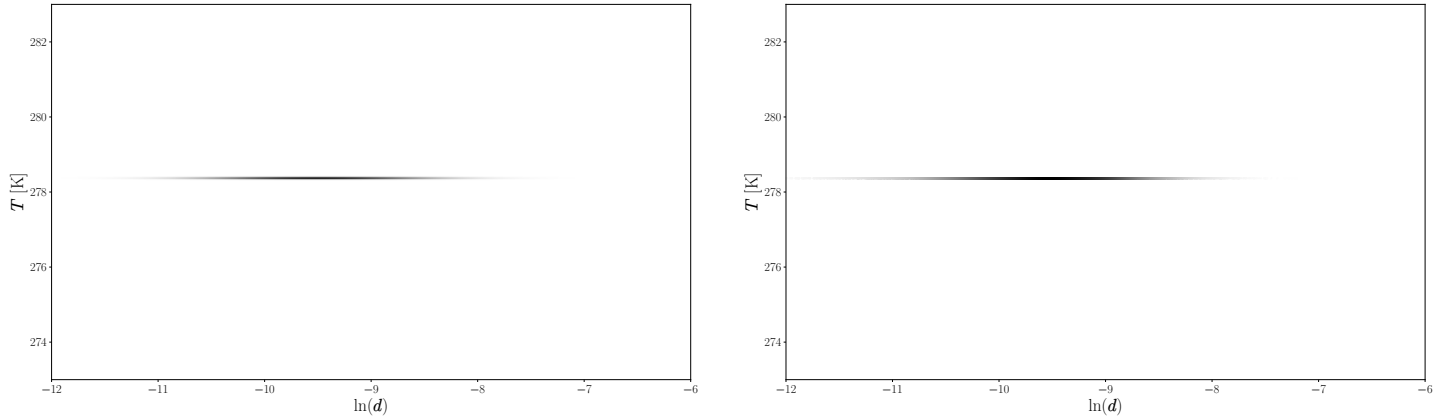

(c) $t = 5.0\,\mathrm{s}$

Figure 8.3: Comparison of density plots in $\ln(d)$-T phase-space of $\tilde{\mathcal{G}}$ (left) and Monte-Carlo solution (right) for a typical dry ($0\%\,\mathrm{RH}$) room-air ($293.15\,\mathrm{K}$ at $1\ \mathrm{atm}$) bio-aerosol spray.

Table 8.5: Summary of constant physical and thermodynamic properties of air at $593.15\,\mathrm{K}$ and $607\,950\,\mathrm{Pa}$ (0% RH).

Property	Value
Molar Mass, M_g $[\mathrm{kg\,mol^{-1}}]$	2.896×10^{-2}
Density, ρ_g $[\mathrm{kg\,m^{-3}}]$	3.572
Dynamic Viscosity, μ_g $[\mathrm{m^2\,s^{-1}}]$	2.993×10^{-5}
Thermal Conductivity, k_g $[\mathrm{W\,m^{-1}\,K^{-1}}]$	4.530×10^{-2}
Specific Heat Capacity, $c_{p,g}$ $[\mathrm{J\,kg^{-1}\,K^{-1}}]$	1.048×10^{3}

Table 8.6: Summary of constant physical and thermodynamic properties of n-heptane with boiling temperature referenced at $371.5\,\mathrm{K}$ and $1\,\mathrm{atm}$.

Property	Value
Molar Mass, M_v $[\mathrm{kg\,mol^{-1}}]$	1.002×10^{-2}
Density, ρ_v $[\mathrm{kg\,m^{-3}}]$	7.006×10^{2}
Thermal Conductivity, k_v $[\mathrm{W\,m^{-1}\,K^{-1}}]$	0.121
Specific Heat Capacity, $c_{p,v}$ $[\mathrm{J\,kg^{-1}\,K^{-1}}]$	2.225×10^{3}
Latent Heat of Vaporization, Δh $[\mathrm{J\,kg^{-1}}]$	3.593×10^{5}

As such, similar to Section 8.1.1, the numerical solution for the proposed problem is time-marched with a fixed time-step of $1 \times 10^{-6}\,\mathrm{s}$ until a final time of $2.5 \times 10^{-2}\,\mathrm{s}$. Likewise, outputs of the moment-states of both the moment model and Monte-Carlo solution are provided at $5 \times 10^{-5}\,\mathrm{s}$ intervals in both surface-weighted conserved and unweighted primitive moment forms. These results are illustrated in Figure 8.1. Statistical convergence having proven more difficult, a total of 120 realizations, each with 2×10^{6} particles, are averaged to achieve sufficient convergence of the Monte-Carlo moment-state solution. Finally, two-dimensional phase-space density plots are again provided in Figures 8.5 and 8.6 for relevant dimensions such to assess the validity of the proposed moment-closure.

Table 8.7: Moments of an n-heptane spray droplet distribution function typical of a direct injection diesel fuel-injector.

Moment	Value
Number Density, n [m^{-3}]	2.0×10^6
Average Velocity, u_x [$\mathrm{m\,s}^{-1}$]	10.0
Average $\ln(d)$, μ	$\ln(18 \times 10^{-6})$
Average Temperature, θ [K]	298.15
Velocity Variance, Ψ_{xx} [$\mathrm{m}^2\,\mathrm{s}^{-2}$]	0.2
$\ln(d)$ Variance, Ψ_{dd}	$(\ln(1.326))^2$
Temperature Variance, Ψ_{TT} [K^2]	0.1
Velocity-$\ln(d)$ Co-variance, Ψ_{xd} [$\mathrm{m\,s}^{-1}$]	0.0
Velocity-Temperature Co-variance, Ψ_{xT} [$\mathrm{m\,K\,s}^{-1}$]	0.0
$\ln(d)$-Temperature Co-variance, Ψ_{dT} [K]	0.0

8.1.2.2 Results and Discussion

Again, a summary of all root-mean-square relative errors (RMSRE), normalized root-mean-square errors (NRMSE), and normalized quasi-steady-state errors (NQSSE) are provided in Table 8.8. In particular however, one should note the rather larger RMSREs obtained for the present case. These errors demonstrate the necessity of a multi-error-based analysis, as the RMSREs do not provide a relevant measure of error for the present case. Specifically, where the the number density is expected to asymptote to zero, measures of relative error become large for any small deviations, thus resulting in surface-weighted conserved moment RMSREs $\geq 571.48\%$. However, on a scale normalized by the variation, errors become more representative. Rather, the computed NRMSEs for the surface-weighted conserved moments are $\leq 2.42\%$. A similar trend is generally observed with regard to the unweighted primitive moments—barring a few notable outliers. Among these outliers, the moment-model is again found to produce an erroneous size distribution evolution as shown in Figures 8.4(b) and 8.4(f). As the solution reaches near-zero density, the first-order unweighted primitive size moment, μ, diverges significantly from the discrete solution, producing an NRMSE of 67.49% and an NQSSE of 118.41%. Examining more closely, the

Table 8.8: Summary of root-mean-square relative error (RMSRE) and normalized root-mean-square error (NRMSE) between the moment-model and Monte-Carlo solutions evaluated over time for a unheated n-heptane spray injected within a dry (0% RH) hot (593.15 K) mixing chamber at above standard atmospheric pressure (607 950 Pa)

Moment	Surface-Weighted Conserved			Unweighted Primitive		
	RMSRE	NRMSE	NQSSE	RMSRE	NRMSE	NQSSE
Zeroth-Order	705.04%	2.04%	4.44%	107.37%	3.65%	0.54%
First-Order Velocity	1113.35%	1.10%	40.27%	28.21%	6.01%	8.98%
First-Order Size	633.87%	1.89%	3.53%	3.33%	67.49%	118.41%
First-Order Temperature	705.12%	2.25%	3.90%	0.91%	4.07%	$< 0.01\%$
Second-Order Velocity	1552.58%	0.68%	92.95%	62.38%	16.28%	20.013%
Second-Order Size	571.48%	1.78%	2.78%	19.81%	17.41%	8.33%
Second-Order Temperature	705.19%	2.42%	3.43%	97.96%	13.59%	$< 0.01\%$
Second-Order Velocity-Size	1000.98%	1.03%	35.00%	60.23%	28.74%	38.08%
Second-Order Velocity-Temperature	1113.58%	1.32%	40.26%	89.06%	10.10%	0.09%
Second-Order Size-Temperature	633.93%	2.08%	3.11%	87.84%	7.80%	0.10%

curve of Figure 8.4(c) describes a size distribution who's median initially becomes smaller. However, due to the non-linear nature of vaporization, an inflection point is observed in both the moment-model and Monte-Carlo solutions—as all small droplets quickly evaporate leaving only the largest droplets. Again however, the proposed moment-closure cannot capture the non-linear deformation of the phase-space density distribution function which consequently produces an erroneous size-variance prediction during the initial bulk evaporation, as shown in Figure 8.4(f). As such, the large divergence occurs once again as the bulk of particles has evaporated and the lognormal size distribution assumptions fails to describe the discrete droplet size distribution deformation. Furthermore, these errors are observed to propagate to the both the first- and second-order primitive velocity moments of Figures 8.4(b) and 8.4(e). Where the moment-model size distribution has diverged from the Monte-Carlo solution, velocity moments are also expected to diverge due to subsequent erroneous aerodynamic gas-droplet interactions. Indeed, despite initial good agreement, an NQSSE of 8.98% for the first-order unweighted primitive velocity moment develops once

the μ inflection occurs. A similar observation is made with regard to the second-order moment where initially good agreement is seen followed by an over-prediction of variance. Moreover, referring to Figures 8.5(a) to 8.5(c), the moment-closure is shown to initially provide good agreement with the discrete droplet v-$\ln(d)$ space-space density distribution. However, given the size-variance which develops through evaporation, increasingly wide droplet momentum response timescales produce an increasingly curvilinear velocity-size co-variance. Again, such a curvilinear relationship between the extended phase-space variables may not be captured by the proposed model. With regard to Figures 8.4(d), 8.4(g), 8.4(i) and 8.4(j), excellent agreement is however observed. As was previously stated, the present case was considered such to assess the droplet heat-up approximation for stiffer heat transfer rates and larger temperature gradients. Where the unweighted primitive temperature moment NRMSEs are all $\leq 13.59\%$, the proposed model is shown to provide great recovery of the discrete solution over the entire solution. Furthermore, while the proposed moment-closure again fails to recover the transient curvilinear size-temperature as seen in Figures 8.6(a) to 8.6(c), the quasi-steady-state is near exactly recovered (i.e., NQSSEs are $\leq 0.10\%$). These results therefore provide a strong argument for the proposed choice of extended phase-space variable, as well as justifies the proposed exponential fit of the Stefan-Fuchs droplet heat-up model.

To review, disagreements were again identified between both the moment-model and a Monte-Carlo solution for both velocity and size related moments. Despite surface-weighted conserved NRMSEs remained small, significant deviations of the unweighted primitive moments were observed. Again, these errors were shown to arise from the artificial lognormal size restriction of the phase-space density distribution function, $\tilde{\mathcal{G}}$, during evaporation. Specifically, where the proposed moment-closure does not accommodate non-linear relationships between the logarithm-based diameter space and other internal variables (i.e., velocity and temperature), transient errors are shown to produce non-negligible quasi-steady-state moment-state errors. Investigations into the proposal of improvements to the moment-model shall therefore remain the subject of future work.

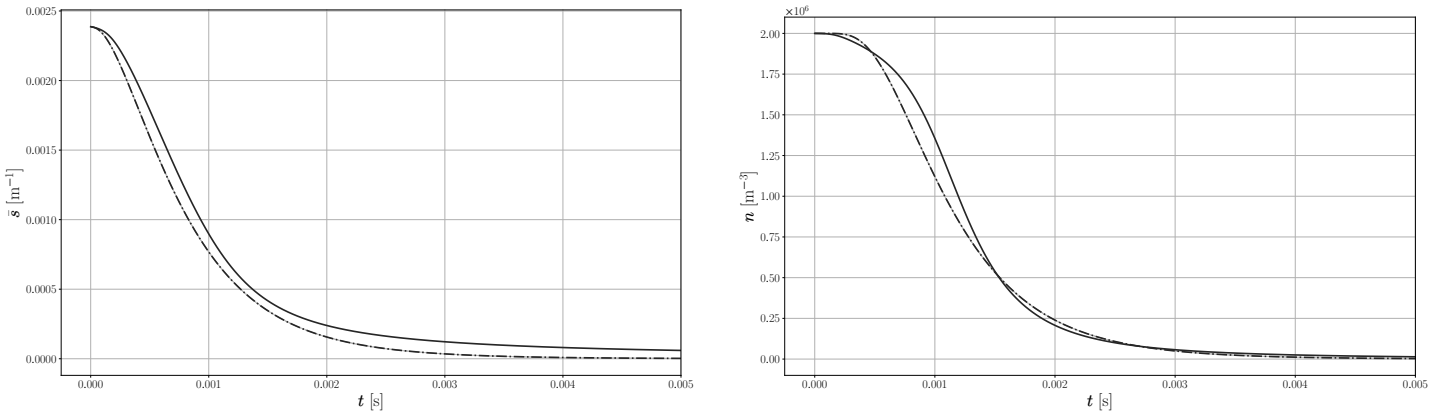

(a) Zeroth-order moments.

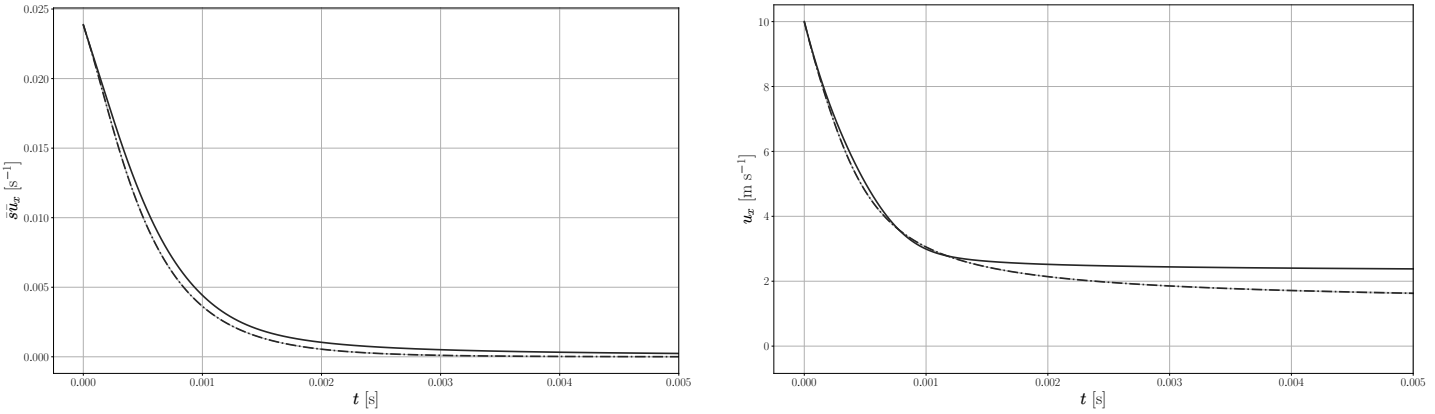

(b) First-order velocity moments.

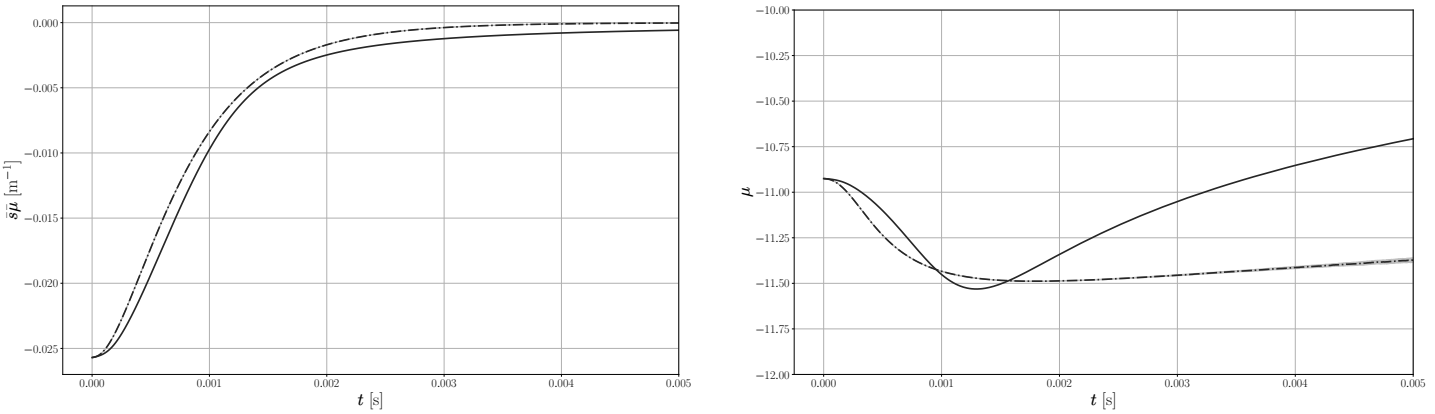

(c) First-order size moments.

Figure 8.4: Comparison of surface-weighted moment-model (solid) against Monte-Carlo solution (dashed) for a unheated n-heptane spray injected within a dry (0% RH) hot (593.15 K) mixing chamber at above standard atmospheric pressure (607 950 Pa). Moments presented in both surface-weighted conserved (left) and unweighted primitive (right) forms. One standard deviation certainty interval of Monte-Carlo solution represented by shaded area.

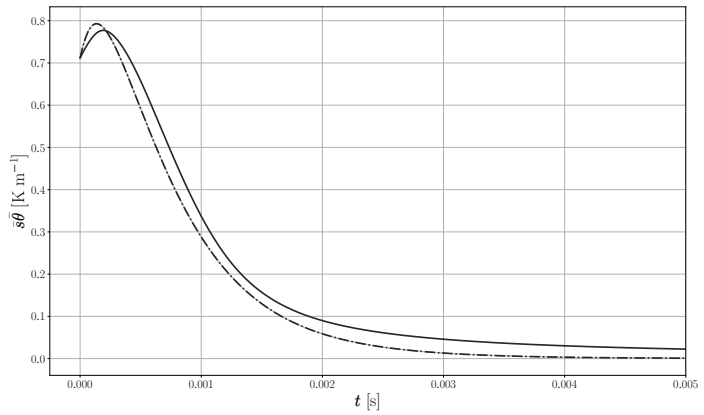

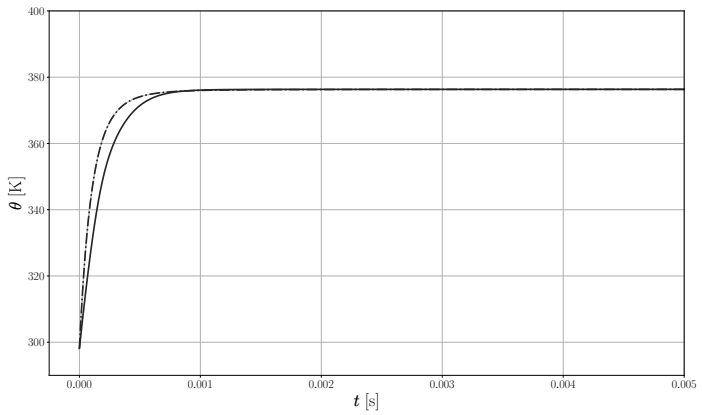

(d) First-order temperature moments.

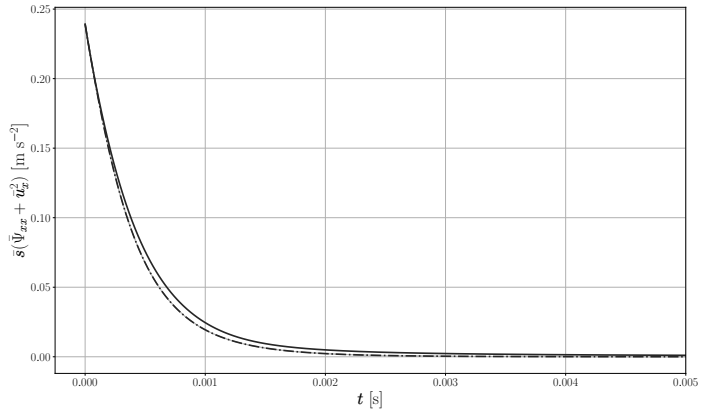

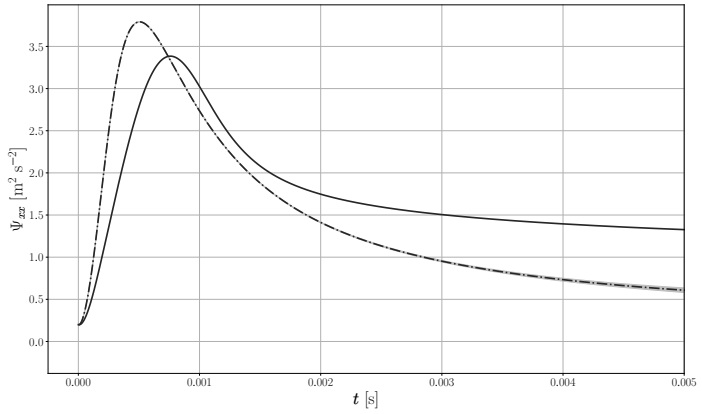

(e) Second-order velocity moments.

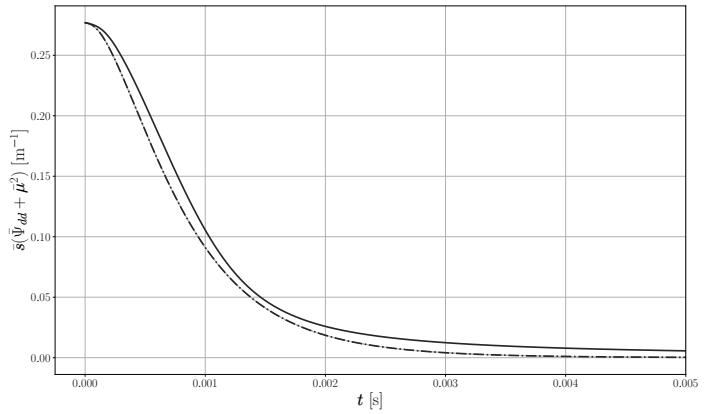

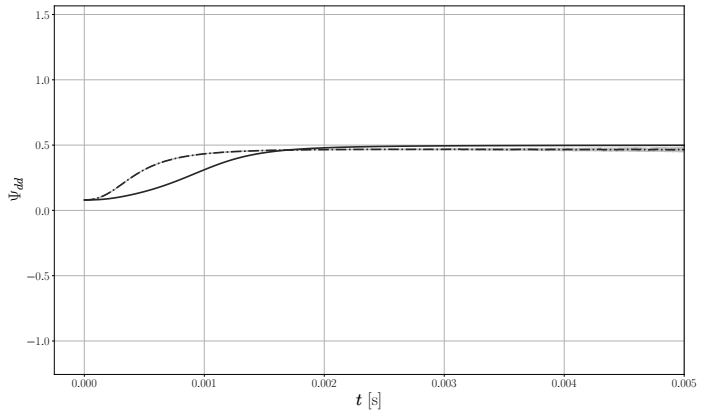

(f) Second-order size moments.

Figure 8.4: Comparison of surface-weighted moment-model (solid) against Monte-Carlo solution (dashed) for a unheated n-heptane spray injected within a dry (0% RH) hot (593.15 K) mixing chamber at above standard atmospheric pressure (607 950 Pa). Moments presented in both surface-weighted conserved (left) and unweighted primitive (right) forms. One standard deviation certainty interval of Monte-Carlo solution represented by shaded area.

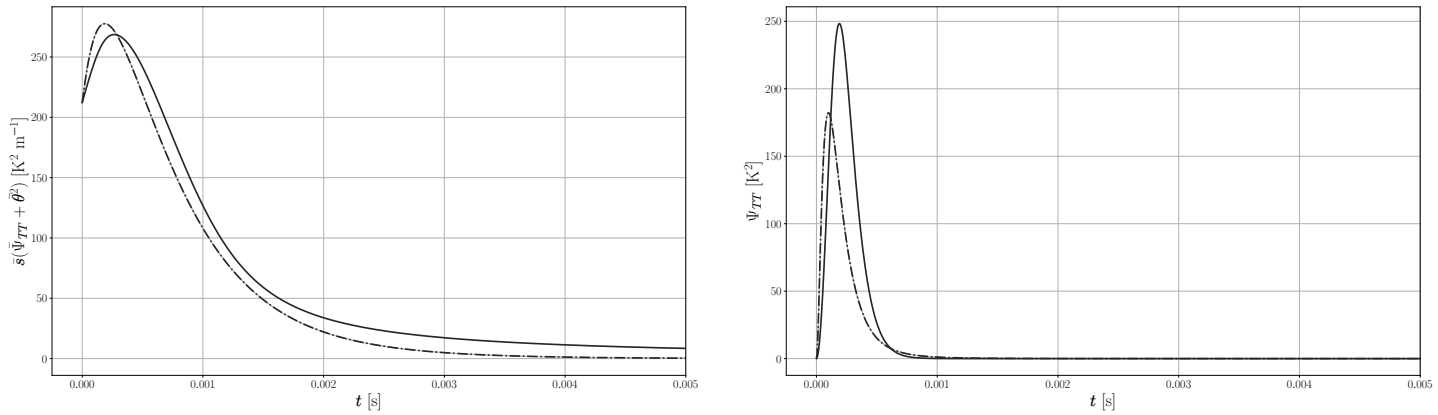

(g) Second-order temperature moments.

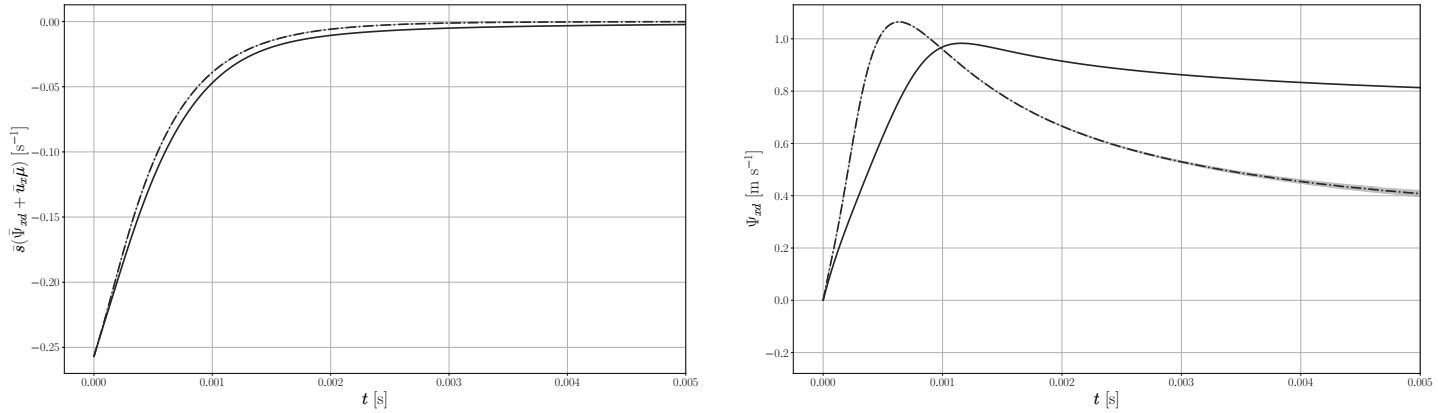

(h) Second-order velocity-size moments.

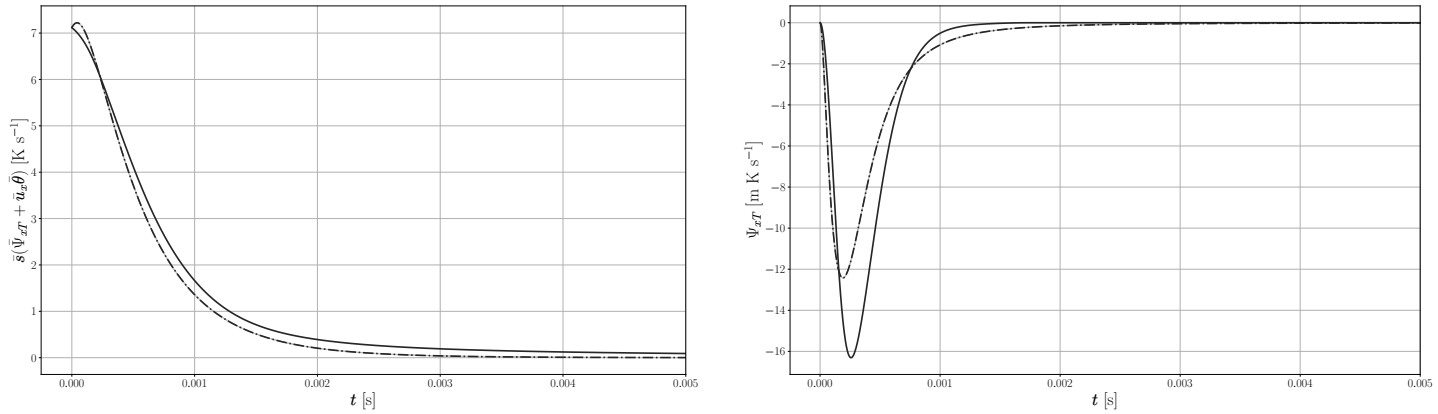

(i) Second-order velocity-temperature moments.

Figure 8.4: Comparison of surface-weighted moment-model (solid) against Monte-Carlo solution (dashed) for a unheated n-heptane spray injected within a dry (0% RH) hot (593.15 K) mixing chamber at above standard atmospheric pressure (607 950 Pa). Moments presented in both surface-weighted conserved (left) and unweighted primitive (right) forms. One standard deviation certainty interval of Monte-Carlo solution represented by shaded area.

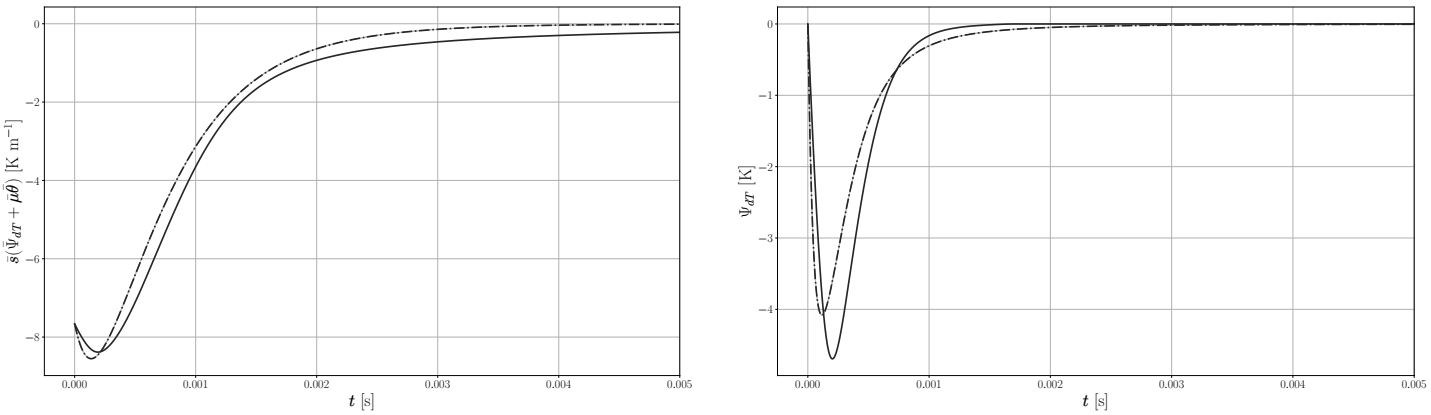

(j) Second-order size-temperature moments.

Figure 8.4: Comparison of surface-weighted moment-model (solid) against Monte-Carlo solution (dashed) for a unheated n-heptane spray injected within a dry (0% RH) hot (593.15 K) mixing chamber at above standard atmospheric pressure (607 950 Pa). Moments presented in both surface-weighted conserved (left) and unweighted primitive (right) forms. One standard deviation certainty interval of Monte-Carlo solution represented by shaded area.

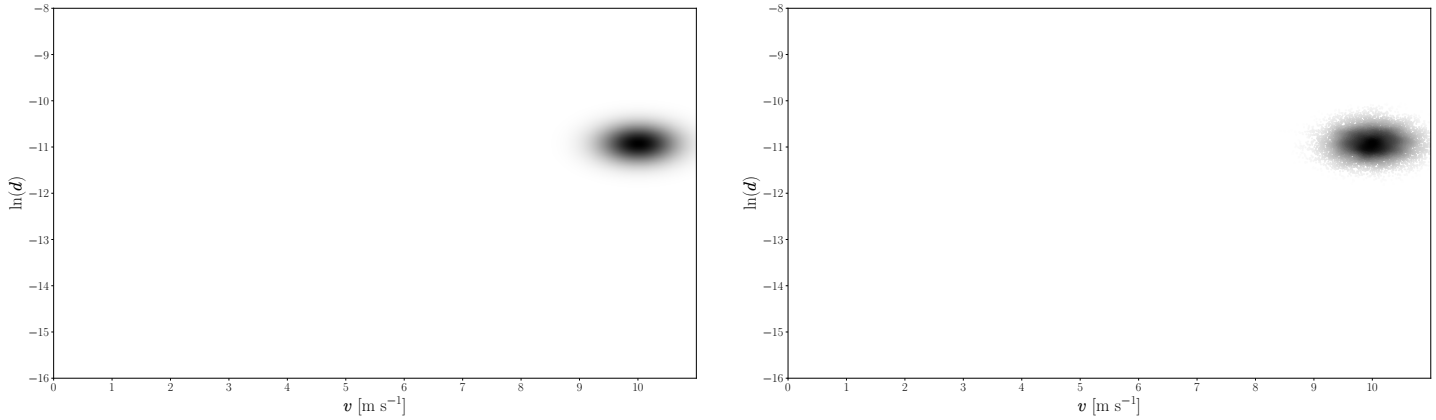

(a) $t = 0\,\mathrm{s}$

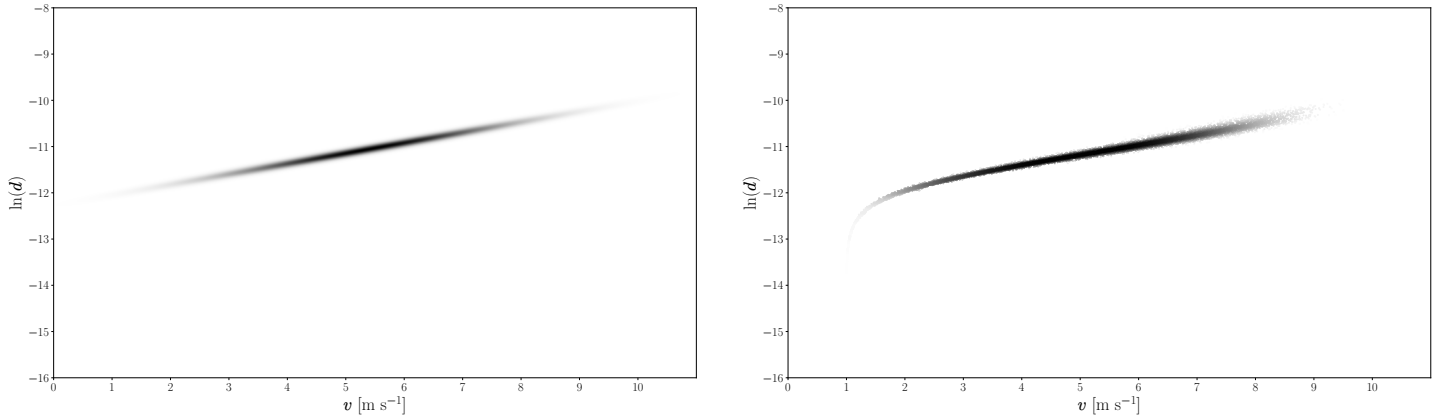

(b) $t = 0.00045\,\mathrm{s}$

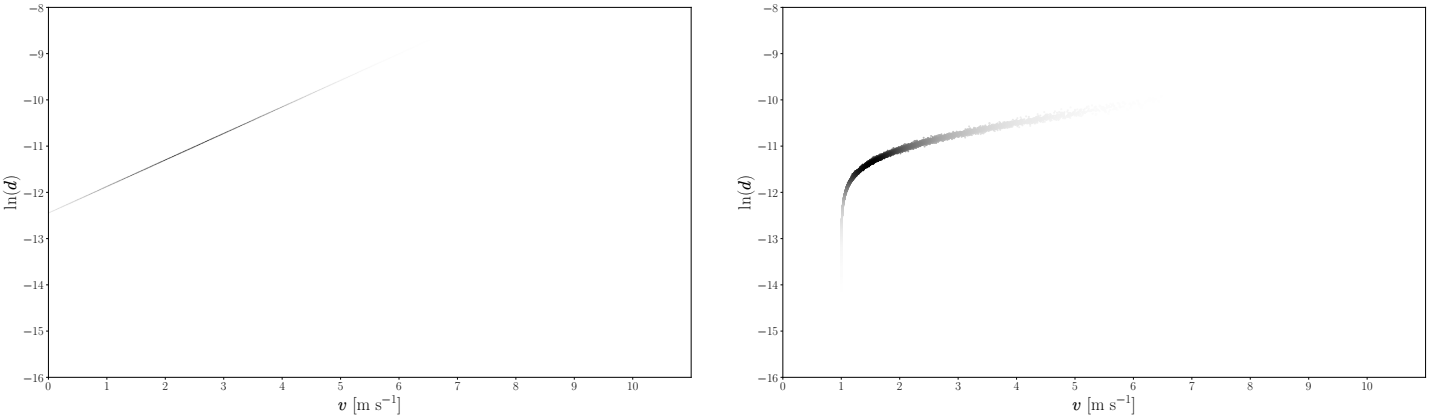

(c) $t = 0.003\,\mathrm{s}$

Figure 8.5: Comparison of density plots in v-$\ln(d)$ phase-space of $\tilde{\mathcal{G}}$ (left) and Monte-Carlo solution (right) for a unheated n-heptane spray injected within a dry ($0\%\,\mathrm{RH}$) hot ($593.15\,\mathrm{K}$) mixing chamber at above standard atmospheric pressure ($607\,950\,\mathrm{Pa}$).

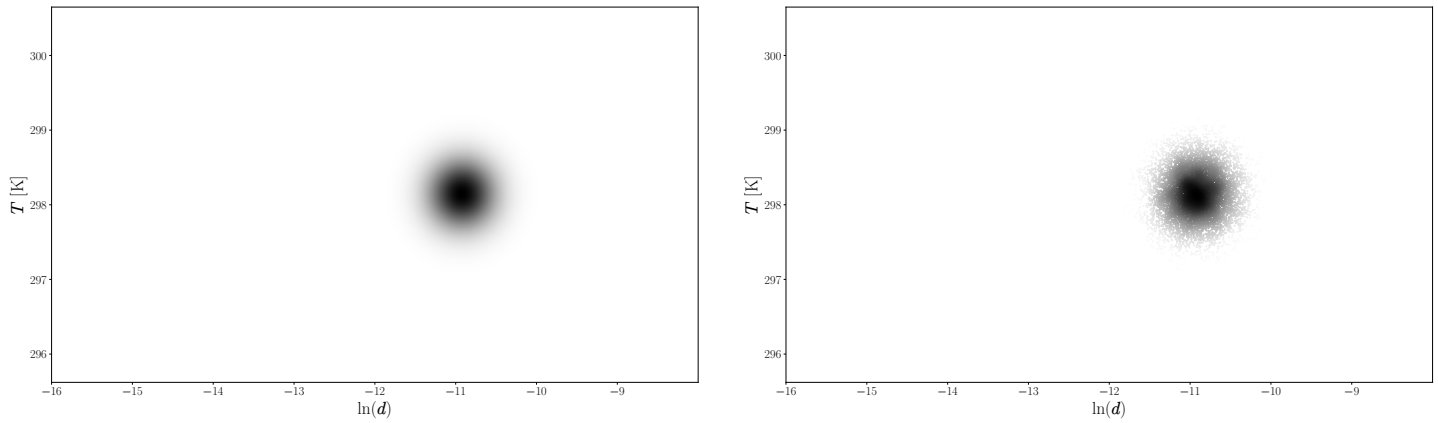

(a) $t = 0\,\mathrm{s}$

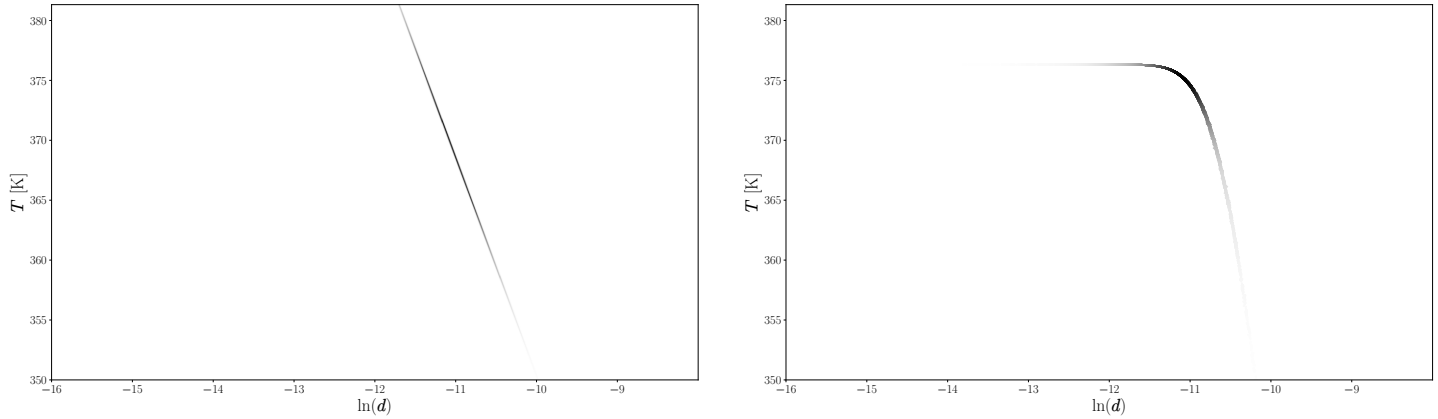

(b) $t = 0.00045\,\mathrm{s}$

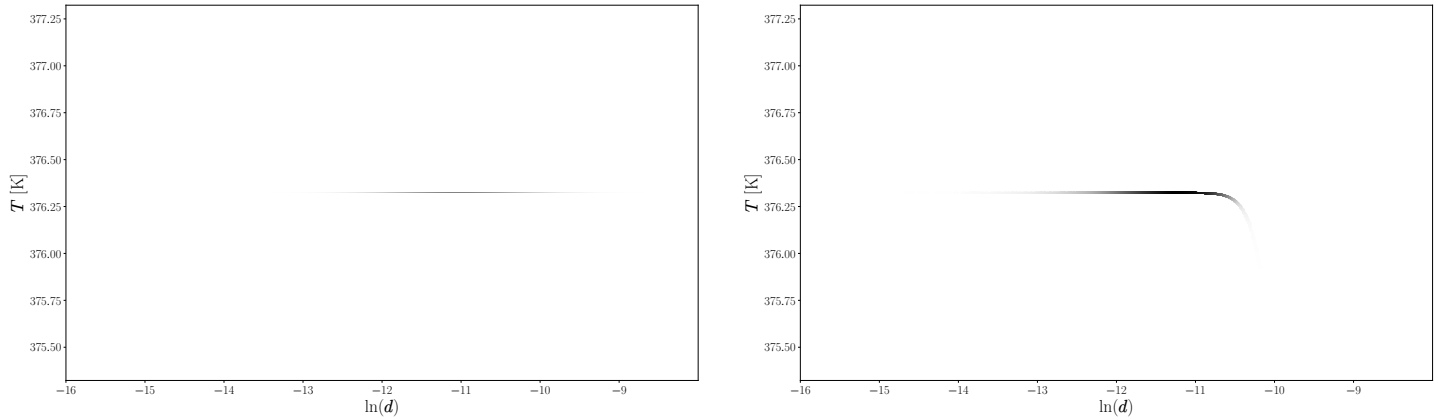

(c) $t = 0.003\,\mathrm{s}$

Figure 8.6: Comparison of density plots in $\ln(d)$-T phase-space of $\tilde{\mathcal{G}}$ (left) and Monte-Carlo solution (right) for a unheated n-heptane spray injected within a dry (0% RH) hot (593.15 K) mixing chamber at above standard atmospheric pressure (607 950 Pa).

8.2 Monodispersed Turbulence Validation

8.2.1 Problem Description

Inspired by the validation efforts of Wei *et al.* [113], assessment and validation of the proposed turbulent eddy-droplet coupling model was performed by reproduction of the Snyder and Lumley wind-tunnel experiment [95]. Cited by many, the Snyder and Lumley experiment provides an idealized case in which single particles of various materials and sizes ($46.5\,\mu\mathrm{m}$ hollow glass, $87.0\,\mu\mathrm{m}$ glass, $87.0\,\mu\mathrm{m}$ corn pollen, and $46.5\,\mu\mathrm{m}$ copper) are released into an isotropic homogeneous grid-generated turbulent flow field. As part of these experiments, various velocity autocorrelation functions are measured along with various Lagrangian and Eulerian turbulence statistics, but most importantly, lateral particle dispersion statistics were measured along the particle trajectories. Where the experiment could be reproduced using Eulerian turbulence data measured longitudinally within the tunnel, the present work evaluates the accuracy of the proposed turbulence coupling model by reproduction and comparison of the lateral dispersion statistics originally measured by Snyder and Lumley.

The experimental apparatus of the study is constructed using a vertically positioned $0.4064\,\mathrm{m}$ x $0.4064\,\mathrm{m}$ x $4.8768\,\mathrm{m}$ wind-tunnel with a blower and particle injector positioned at the base of the apparatus. The blower provides a steady flow-rate producing a constant $\overline{U} = 6.55\,\mathrm{m\,s^{-1}}$ velocity field at $299.15\,\mathrm{K}$ and roughly 40% RH. Then, using a series of optical detectors, particle trajectories are simply recorded along the length of the wind-tunnel starting at $1.737\,36\,\mathrm{m}$ from the tunnel entrance. By statistical analysis, the Lagrangian particle paths are then averaged to obtain relevant velocity autocorrelation functions and turbulent dispersion statistics for the various particle types as the entrance of the tunnel includes a $1\,\mathrm{in.}$ square grid producing a stationary turbulent grid flow. Importantly, measurements of the turbulent flow field are taken using a constant-temperature hot-wire anemometer along the wind-tunnel—providing required Eulerian turbulence data which is summarized in Table 8.9.

Table 8.9: Eulerian turbulence data [95].

x/M	41	64	73	107	138	171
ε $[\mathrm{cm\,s^{-3}}]$	5430	1610	1160	480	266	165

Note, using the data provided, a power fit is produced to provide a continuous expression for the turbulent energy dissipation rate, ε. The optimized fit is simply

$$\varepsilon(x) = \frac{0.552449315550251}{x^{2.42438979877701}}\,, \tag{8.4}$$

where x is the longitudinal distance from the wind-tunnel entrance measured in meters. As for the turbulent kinetic energy, Snyder and Lumley provide an expression for the root-mean-square turbulent fluctuation velocity based upon computed energy decay curves. In terms of the longitudinal distance, x, this expression is

$$U'^{2}_{\mathrm{rms}}(x) = \frac{\bar{U}^{2}}{42.4\,\left(\frac{x}{0.0254} - 16\right)}\,, \tag{8.5}$$

from which the turbulent kinetic energy is taken as

$$\bar{E}(x) = \frac{3}{2}\,U'^{2}_{\mathrm{rms}}(x)\,. \tag{8.6}$$

In regards to the characteristic turbulence timescale, ω, selected for the proposed model, the choice remains admittedly ad-hoc. Numerical experiments conducted as part of this analysis have yielded a best-fit using the Eulerian microscale,

$$\omega^{-1}(x) = \tau_{\mathcal{E}}(x) = \sqrt{\frac{6\,\nu}{\varepsilon(x)}}\,, \tag{6.101}$$

with $\nu = 1.571 \times 10^{-5}\,\mathrm{m^2\,s^{-1}}$ the kinematic viscosity of air for the experimental conditions. However, where the flow Reynolds number changes, results for various other attempted problems suggest best-fits using the Lagrangian integral timescale, e.g., for atmospheric dispersion problems for tracer-like particles. Such discrepancies highlight the necessity in

determining the relationship between the flow Reynolds number and characteristic turbulence timescale of the proposed model which remains the important subject of future work. In particular, further efforts are required for the development of a robust argument for the proposed blending function, $\mathcal{X}$, as other authors have investigated for various models [100]. Nevertheless, the present work provides a framework for future studies within the scope of the current ad-hoc implementation.

In order to achieve comparable particle injection, a Gaussian point-like particle source was introduced into the domain at the position of the experiment's first position measurement, i.e., the Gaussian point-like source introduces particles within a Gaussian-radius, σ_r, of $4 \times 10^{-4}\,\mathrm{m}$ at $x_0 = 1.737\,36\,\mathrm{m}$. Notably, particles are not injected at the tunnel entrance as otherwise performed during the physical experiment. In fact, this discrepancy arises from the Lagrangian versus Eulerian nature of the experiment and proposed numerical reproduction. Where particles reach the first measurement point, x_0, with a random deviation from the centerline of the wind-tunnel, the experimental dispersion statistics are computed from a Lagrangian reference-frame, whereby displacements become relative to the arbitrary particle origin, $[x_0, y_0]$, and are averaged for myriad particles. Unfortunately, the proposed Eulerian-based moment-model can not replicate such measurements. Instead, the moment-model allows the replication of the experiment by consideration of a jet-like flow centered along the wind-tunnel centerline and who's origin is fixed at x_0. The result yields a jet which disperses upwards into the wind-tunnel, and who's cross-section density plot provides a measurement of lateral particle dispersion. An illustration of a numerical solution of the moment-model is provided in Figure 8.7(b) Importantly, as particles arriving at x_0 would otherwise have some initial velocity variance, the proposed source introduces particles with a non-zero velocity variance at the jet origin. Specifically, particles are injected with a variance of

$$\Psi_{ij_0} = 2\,U'^2_{\mathrm{rms}}(x_0)\,\mathrm{erfc}\left(\frac{\sqrt{\pi}\,\left(\mu + \ln\left(\sqrt{\gamma_m\,\omega(x_0)}\right)\right)}{\sqrt{1 + 2\Psi_{dd}\,\gamma_m\,\omega(x_0)}}\right)\,\delta_{ij}\,. \tag{8.7}$$

Finally, the injection velocity of particles is also estimated by evaluating the particle settling velocity, u_T—assuming particle momentum response timescales are much shorter than the

time to travel from the tunnel entrance to x_0. A summary of the injected moment-state for an arbitrary particle is provided in Table 8.10.

Table 8.10: Moments of an arbitrary particle distribution at the Gaussian point-like particle source for the Snyder and Lumley moment-model reproduction.

Moment	Value
Number Density, n $[\mathrm{m}^{-3}]$	$1.0 \cdot 10^{12}\,\boldsymbol{G}$
Average x-Velocity, u_x $[\mathrm{m\,s}^{-1}]$	u_T
Average y-Velocity, u_y $[\mathrm{m\,s}^{-1}]$	0.0
Average $\ln(d)$, μ	$\ln(d_p)$
x-Velocity Variance, Ψ_{xx} $[\mathrm{m}^2\,\mathrm{s}^{-2}]$	Ψ_{xx_0}
x-Velocity and y-Velocity Co-variance, Ψ_{xy} $[\mathrm{m}^2\,\mathrm{s}^{-2}]$	0.0
y-Velocity Variance, Ψ_{yy} $[\mathrm{m}^2\,\mathrm{s}^{-2}]$	Ψ_{yy_0}
$\ln(d)$ Variance, Ψ_{dd}	$1.0 \cdot 10^{-5}$
x-Velocity and $\ln(d)$ Co-variance, Ψ_{xd} $[\mathrm{m\,s}^{-1}]$	0.0
y-Velocity-$\ln(d)$ Co-variance, Ψ_{yd} $[\mathrm{m\,s}^{-1}]$	0.0

* $\boldsymbol{G}$ is a Gaussian distribution of width σ_r centered at x_0 along the wind-tunnel centerline.
** Temperature moments are omitted as evaporation is irrelevant to the considered problem.

Regarding the numerical reproduction, discretization of the wind-tunnel was performed using a multi-block cartesian mesh in which the domain was over-resolved for convergence requirements using $22\,736$ square 12 x 12 cartesian blocks ($3\,273\,984$ cells) created by localized mesh refinement—with a mesh refinement criteria defined using conservative estimates of the largest expected particle dispersion. An illustration of the domain discretization is provided in Figure 8.7(a). Time marching of all solutions was performed using a CFL condition number of 0.2 until a final time of $2.0\,\mathrm{s}$ such that the particle jet reached a converged steady-state.

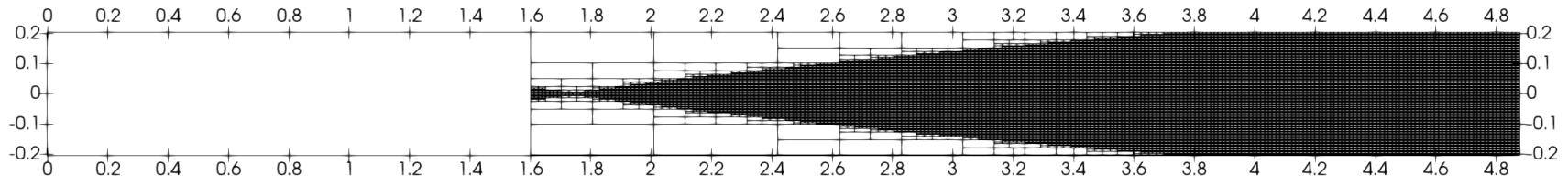

(a) Domain and outline of **12** x **12** cell multi-block discretization.

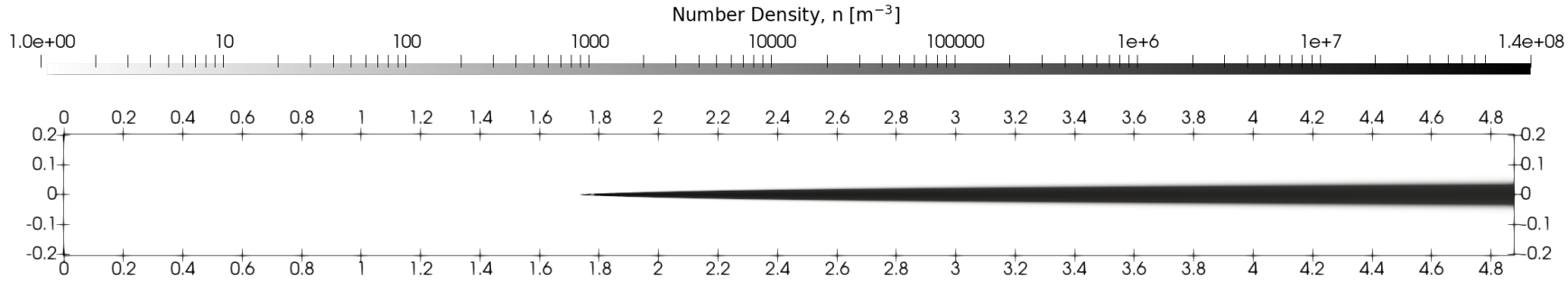

(b) Number density.

Figure 8.7: Numerical reconstruction of Snyder and Lumley (1970) turbulent dispersion experiment. Illustration of (a) the multi-block grid produced with adaptive mesh refinement, and (b) an example steady-state number density plot for the corn pollen particle experiment.

8.2.2 Results and Discussion

A comparison of dispersion profiles obtained for the four particle types using the proposed turbulent eddy-droplet coupling model against the profiles measured by Snyder and Lumley is provided in Figure 8.8.

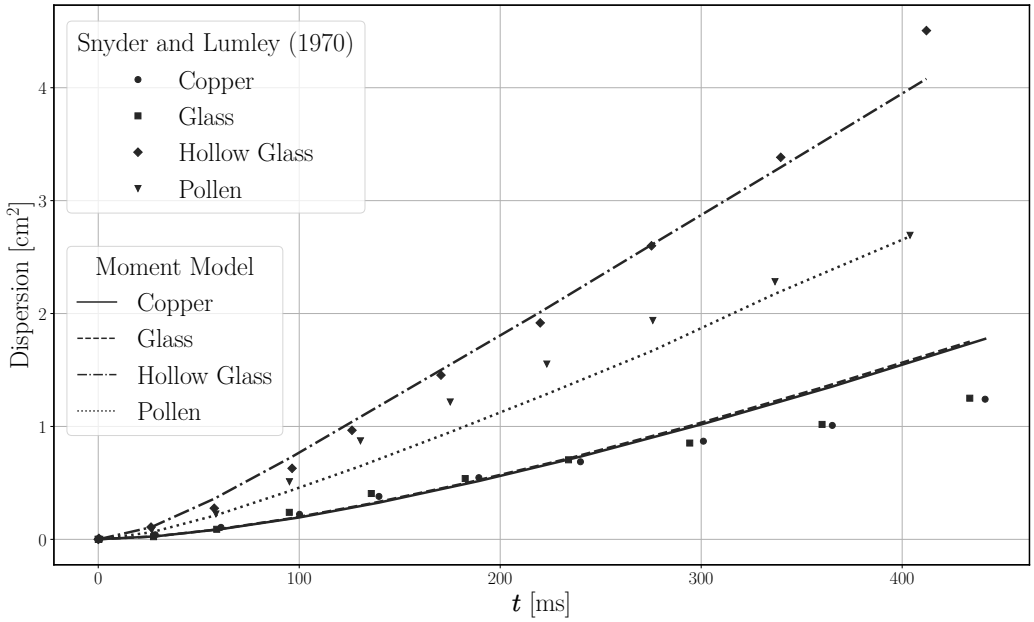

Figure 8.8: Comparison of lateral particle dispersion measurements provided by Snyder and Lumley (1970) for four particles against predictions obtained using the proposed turbulent eddy-droplet coupling moment model.

In general, agreement is good for all particles. The best agreement is observed for the lighter particles, i.e., the hollow glass beads and corn pollen, while the worst agreement is observed for the heaviest particles, i.e., the glass and copper beads. Computing the root-mean-square relative errors (RMSRE), the smallest RMSRE is obtained for the tracer-like hollow glass bead particle, where the RMSRE is 12.42%. A similar magnitude error is also observed for the medium Stokes number particle—the corn pollen—where the RMSRE is 16.63% and some initially disagreement is observed for $t \leq 350\,\mathrm{ms}$. However, for both the largest Stokes number particles, the RMSRE is significantly larger—being 24.09% and

21.26% for the copper and glass beads, respectively. Notably, while these RRMSE remain small, relative errors measured at the final measurement are indicative of more significant disagreement (34.09% for copper and 32.12% for glass). These results suggest the pro-

Particle	RMSRE	NRMSE
Hollow	12.42%	3.59%
Pollen	16.63%	6.79%
Glass	21.25%	17.04%
Copper	24.09%	18.30%

Table 8.11: Summary of root-mean-square relative error (RMSRE) and normalized root-mean-square error (NRMSE) between lateral particle dispersion measurements provided by Snyder and Lumley (1970) for four particles and predictions obtained using the proposed turbulent eddy-droplet coupling moment-model.

posed model best captures turbulent dispersion of low turbulent Stokes number problems in which particles/droplets exhibit a high-degree of coupling with turbulent fluctuations of the gaseous flow field. For these particles, the modified momentum response time, τ_m, of the drift correction term is heavily influenced (if not entirely dominated) by the characteristic turbulence timescale, ω, as the enhanced turbulent particle dispersion is strongly driven by eddy-transport. As for the higher turbulent Stokes number particles, i.e., the copper and glass beads, the model provides worse yet nonetheless reasonable results. Notably, disagreement for these particles grows where ω begins to decay. Specifically, at the wind-tunnel entrance, turbulent high-frequency fluctuations are observed which become less energetic, and of lower-frequency, with distance along the wind-tunnel. Where these fluctuations are high-frequency, eddy-particle coupling is light for the more inertial particles tested—whereby τ_m is dominated by the unmodified momentum response timescale, τ_d. However, as frequencies decay, τ_m is expected to blend both τ_d and ω timescales—as observed by the continuously increasing slope of the predicted dispersion curves. By comparison to the experimental measurements, these remain mostly linear for the duration of the measurements. Such results would therefore suggest the premature transition between inertia/eddy controlled dispersion by effect of the current proposed blending function, $\mathcal{X}$. However, the observed turbulent dispersion is not solely controlled by the drift

correction term. Rather, it is more importantly also controlled by the proposed coupling function. The over-prediction of turbulent dispersion may therefore also be indicative of an over-prediction of turbulent eddy-particle coupling through assumed Stokes flow interactions. Unfortunately, such an over-prediction is expected from the proposed model where the particle Reynolds number becomes $Re_d \geq 1$ as the Stokes flow assumption is known to significantly over-predict aerodynamic drag. As such, given that the coupling function attenuates eddy-particle coupling based upon a Stokes flow assumption, the eddy-particle coupling model would also inherently over-predict eddy and particle interactions through aerodynamic drag once $Re_d \geq 1$. As a result, for Reynolds numbers increasingly larger than unity, a larger turbulence generated variance would be predicted—leading to increased dispersion. As provided by Snyder and Lumley, the particle Reynolds numbers are observed to be larger than unity for the corn pollen (1.10), glass beads (2.48), and copper beads (1.45). Consequently, larger errors are inherently expected for these particles. Likewise, these errors further highlight the need to develop more accurate moment-model approximations to aerodynamic drag laws for a wider range of particle Reynolds numbers.

Nevertheless, these preliminary validation efforts do suggest promising potential for the proposed turbulent eddy-droplet coupling model and subsequent drift correction approximation. In fact, when compared to results of Wei and Li, the proposed model is seen to provide similar, or better, results than more widely adopted Lagrangian DRW models, see Figure 8.9. As such, continued investigations into the development of the proposed model hold the potential for introducing a new and much simplified approach to turbulent gas-particle multiphase flow modelling. However, such investigations will remain the subject of future work.

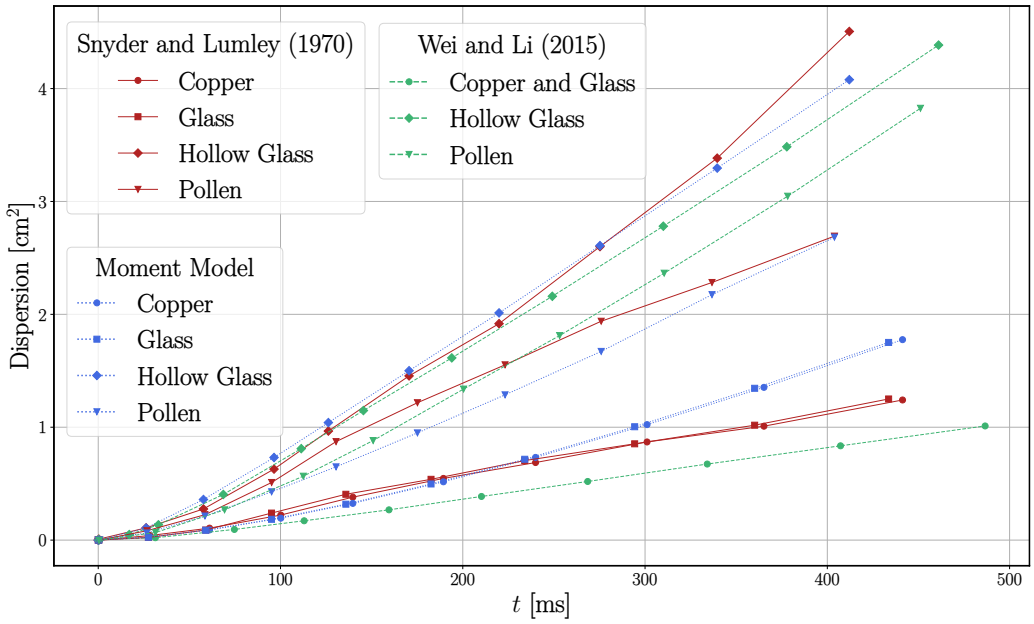

Figure 8.9: Comparison of lateral dispersion predictions obtained using the proposed turbulent eddy-droplet coupling moment model against DRW model results of Wei and Li (2015) [113].

8.3 Two-Dimensional Qualitative n-Heptane Fuel-Injection Problem

8.3.1 Problem Description

Within the following section, a qualitative assessment of the proposed two-scalar PGM for evaporating sprays is performed for a two-dimensional spray problem. For the purpose of this investigation, the moment-model is implemented within a two-dimensional first-order Godunov-type finite-volume scheme, as described in Section 7.2. The case considered is a modified version of the previously considered n-heptane fuel-spray of Section 8.1.2. Here, a spray of atomized liquid n-heptane is again injected at high Stokes number into hot pressurized air, i.e., dry (0% RH) air at 593.15 K and 607 950 Pa. For tables of the associ-

ated physical and thermodynamic properties of air and n-heptane for these conditions, one should again refer themselves to Tables 8.5 and 8.6. Most notably however, a transverse cross-flow (relative to the injection velocity) within the gaseous carrier phase is introduced. Specifically, a high-velocity air flow ($\overline{U}_x = 10.0\,\mathrm{m\,s^{-1}}$) is considered such to induce asymmetric dispersion of the injected fuel-spray. Lastly, regarding the injected spray, a similar moment-state to that of Section 8.1.2 is considered, with exception of the number density which is instead a number density time rate of change, $\dot{n}$, and initial velocity variances set to near zero. A summary of the injected moment-state is provided in Table 8.12.

Table 8.12: Two-dimensional moments of an n-heptane spray droplet distribution function typical of a direct injection diesel fuel-injector.

Moment	Value
Time-rate Number Density, $\dot{n}$ $[\mathrm{m^{-3}}]$	2.0×10^9 $\boldsymbol{G}$
Average x-Velocity, u_x $[\mathrm{m\,s^{-1}}]$	0.0
Average y-Velocity, u_y $[\mathrm{m\,s^{-1}}]$	10.0
Average $\ln(d)$, μ	$\ln(18 \times 10^{-6})$
Average Temperature, θ [K]	298.15
x-Velocity Variance, Ψ_{xx} $[\mathrm{m^2\,s^{-2}}]$	1×10^{-8}
x-Velocity and y-Velocity Co-variance, Ψ_{xy} $[\mathrm{m^2\,s^{-2}}]$	0.0
y-Velocity Variance, Ψ_{yy} $[\mathrm{m^2\,s^{-2}}]$	1×10^{-8}
$\ln(d)$ Variance, Ψ_{dd}	$(\ln(1.326))^2$
Temperature Variance, Ψ_{TT} $[\mathrm{K^2}]$	0.1
x-Velocity and $\ln(d)$ Co-variance, Ψ_{xd} $[\mathrm{m\,s^{-1}}]$	0.0
y-Velocity and $\ln(d)$ Co-variance, Ψ_{yd} $[\mathrm{m\,s^{-1}}]$	0.0
x-Velocity and Temperature Co-variance, Ψ_{xT} $[\mathrm{m\,K\,s^{-1}}]$	0.0
y-Velocity and Temperature Co-variance, Ψ_{yT} $[\mathrm{m\,K\,s^{-1}}]$	0.0
$\ln(d)$ and Temperature Co-variance, Ψ_{dT} [K]	0.0

* $\boldsymbol{G}$ is a Gaussian distribution of width σ_r centered at $[0.002, 0.002]$ m within the domain.

The modelled domain extends over a two-dimensional square $0.04\,\mathrm{m}$ x $0.04\,\mathrm{m}$ region. Discretization of the domain was then performed using a multi-block cartesian mesh consisting of 768 parallel distributed blocks resulting in a structured grid of $359\,296$ cells. An illustration of the domain discretization is provided in Figure 8.10. To model the injector, a Gaussian point-like droplet source with Gaussian-radius, σ_r, of $2 \times 10^{-4}\,\mathrm{m}$ is introduced into domain at $[0.006, 0.004]$ m. Lastly, time marching of problem was performed using a CFL condition number of 0.15 until a final time of $0.0125\,\mathrm{s}$ such that the spray achieves a steady-state, which is sufficient by recalling the largest droplet life timescales of $0.003\,\mathrm{s}$ from the results of Section 8.1.2.

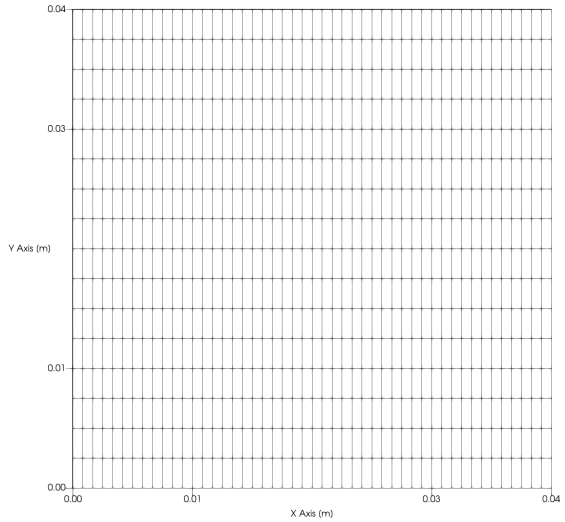

(a) Domain and outline of 32 x 96 cell multi-block discretization ($359\,296$ cells).

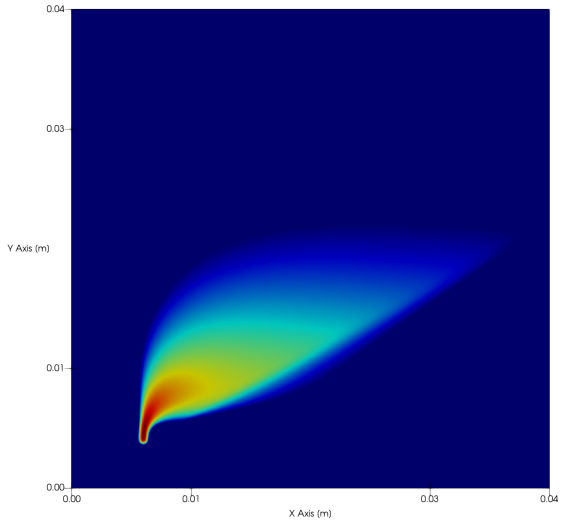

(b) Number density (entire domain).

Figure 8.10: Illustration of (a) the multi-block discretization, and (b) a contour plot of number density to identify the region of interest.

8.3.2 Results and Discussion

The results obtained for the present problem are strictly qualitative in nature and are intended to solely provide a demonstration of the two-scalar PGM's modelling capabilities. Figure 8.11(a) shows contour plot of number density at steady-state following the steady injection of the initially cold n-heptane spray. Due to aerodynamic interactions between the gaseous and droplet phases, the upward injected spray is observed to disperse into an asymmetric jet within the flow, with the highest number density observed at the bottom left of the spray. Notably, the curvature of the spray is indicative of expected size segregation. Specifically, injected droplets become accommodated by the transverse flow at varying rates due to the underlying polydispersity of the injected spray, which produces the curved trajectories as shown by the velocity gradients of Figures 8.11(b) and 8.11(c). The largest curvature radius is, of course, adopted by the largest droplets which are least influenced by the flow. As shown in Figure 8.11(d), size segregation of the spray is effectively well-captured by the model, with largest droplets penetrating furthest into the domain. Likewise, the average droplet size is observed to decrease as the spray travels away from the injection site as vaporization occurs. Furthermore, temperature gradients are also captured as the polydispersity produces significant variability in droplet heat-up times during injection, as shown in Figure 8.11(e). Most notably however, the proposed higher-order moment-model also captures high-order statistics of the underlying droplet spray. As shown in Figures 8.11(f) and 8.11(g), large velocity variances are captured near the injection site as aerodynamic interactions produce large sub-grid velocity distributions. Similarly, large temperature variance is also captured as the initial bulk of polydisperse droplets heat-up at largely varying rates, as observed in Figure 8.11(i). Furthermore, co-variances between velocities and droplet diameter are shown to develop within Figures 8.11(j) and 8.11(k), which effectively describe varying rates of inertial accommodation as a function of droplet size. While no quantifiable assessment is provided on the accuracy of these high-order statistics, these preliminary results are nonetheless sufficient to identify expected correlations resulting from the considered gas-droplet coupling models which would otherwise not be captured using traditional Eulerian gas-droplet multiphase flow models. Unfortunately, validation of the present results, along with the study of observed structures within the obtained high-order statistics, will remain the subject of future work.

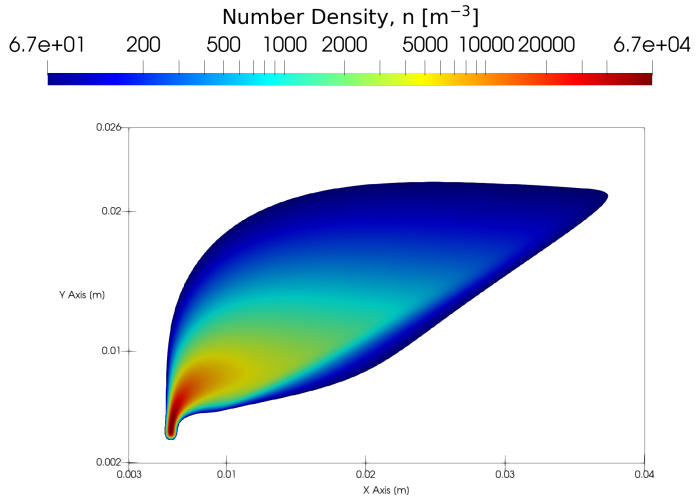

(a) Number density.

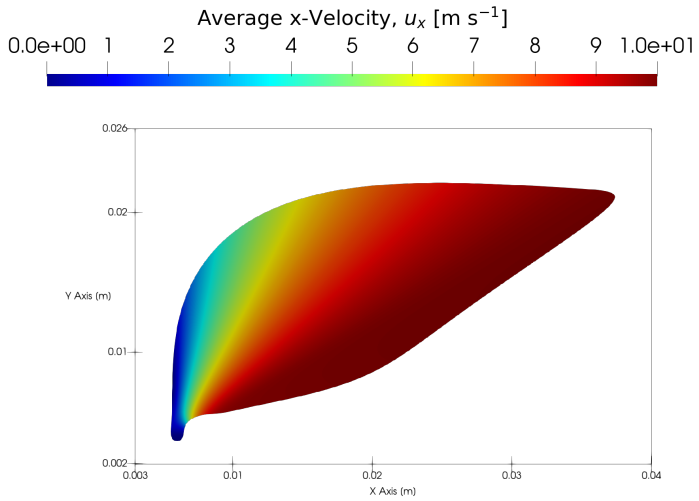

(b) Average x-Velocity.

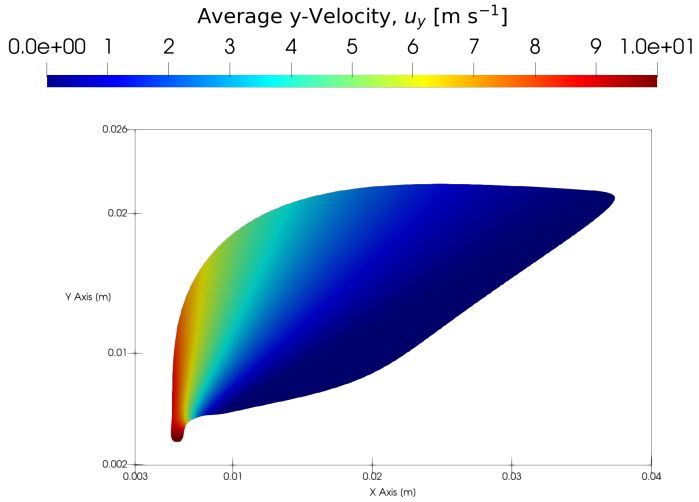

(c) Average y-Velocity.

Figure 8.11: Steady-state contour plots of primitive unweighted moments for an unheated n-heptane spray injected within a transverse flow of dry (0% RH) hot (593.15 K) mixing chamber at above standard atmospheric pressure (607 950 Pa). Thresholding filter applied to identify regions with $n \geq 0.1\%$ of $n_{\max}$.

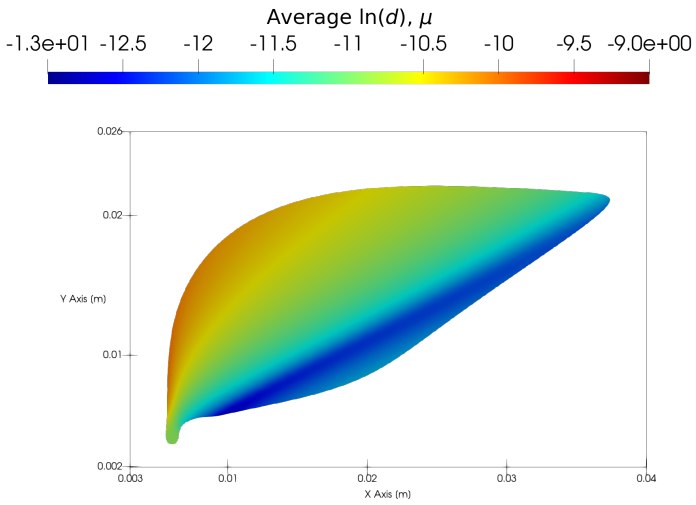

(d) Average $\ln(d)$.

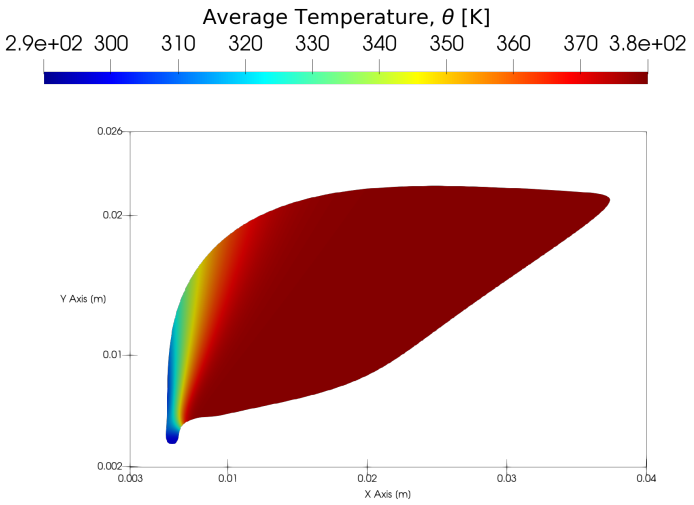

(e) Average temperature.

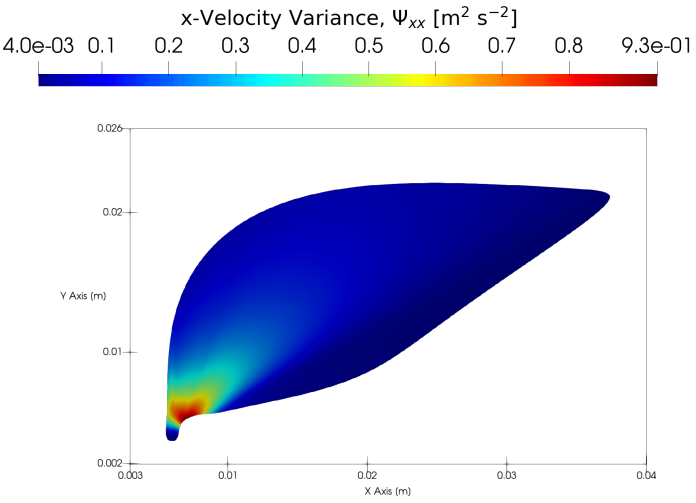

(f) x-Velocity Variance.

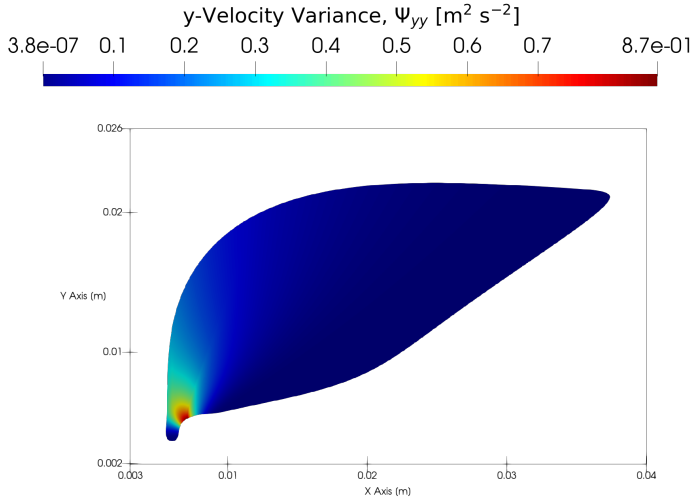

(g) y-Velocity Variance.

Figure 8.11: Steady-state contour plots of primitive unweighted moments for an unheated n-heptane spray injected within a transverse flow of dry (0% RH) hot (593.15 K) mixing chamber at above standard atmospheric pressure (607 950 Pa). Thresholding filter applied to identify regions with $n \geq 0.1\%$ of $n_{\max}$.

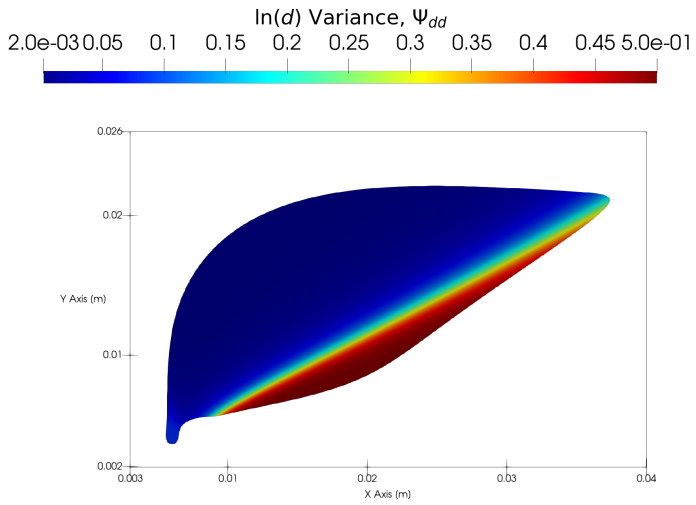

(h) $\ln(d)$ Variance.

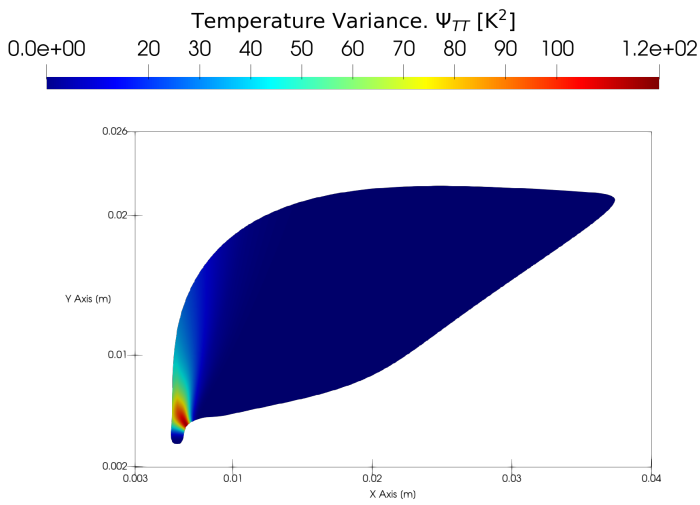

(i) Temperature Variance.

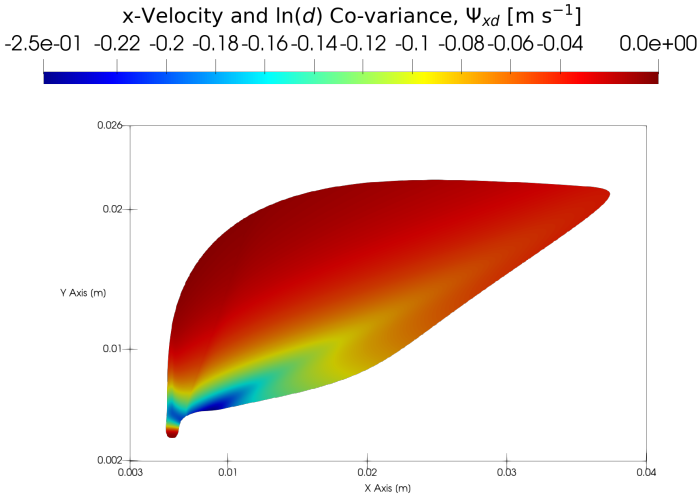

(j) x-Velocity and $\ln(d)$ Co-variance.

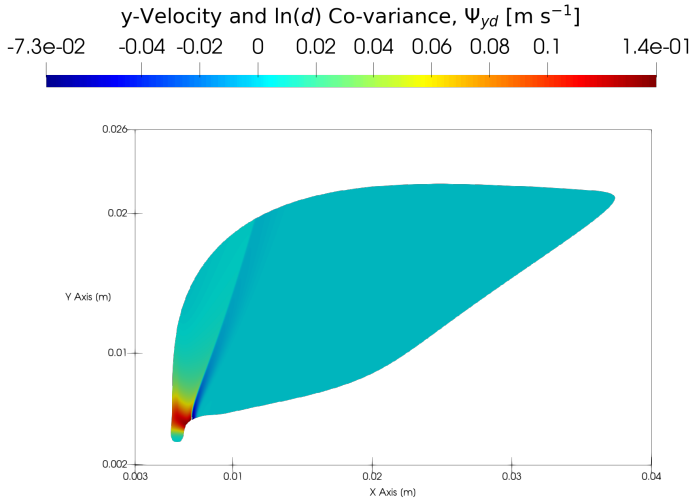

(k) y-Velocity and $\ln(d)$ Co-variance.

Figure 8.11: Steady-state contour plots of primitive unweighted moments for an unheated n-heptane spray injected within a transverse flow of dry (0% RH) hot (593.15 K) mixing chamber at above standard atmospheric pressure (607 950 Pa). Thresholding filter applied to identify regions with $n \geq 0.1\%$ of $n_{\max}$.

Chapter 9

Conclusion and Future Work

9.1 Summary

The work completed as part of this thesis covers the formulation and implementation of a novel two-scalar polydispersed Gaussian-moment model for evaporating and turbulent gas-particle multiphase flows. Derived from the kinetic theory of gases, the proposed model is shown to provide a system of twenty-one robustly hyperbolic first-order balance law for the description of dilute polydispersed and polythermal droplet distributions. In the treatment of evaporating sprays, two formulations are analyzed whereby surface-weighted statistics are shown to be necessary for the accurate and stable recovery of droplet vaporization. Moreover, using classical hydrodynamic droplet evaporation theory, an approximate Stefan-Fuchs droplet evaporation model is proposed such to provide closed-form moment expressions for the description of unsteady-evaporating sprays. Analysis of the proposed model is achieved by implementation of a one-dimensional space-homogeneous moment solver, along with a Monte-Carlo solver to provide a statistically averaged exact solution to the discrete distribution solution. Preliminary investigations demonstrate the accuracy of the proposed approximate vaporization model for the recovery of bulk droplet heat transfer. However, the proposed moment-closure is discovered to inaccurately capture droplet mass transfer in quasi-steady-state for two space-homogeneous spray problems due to the prescribed distribution of the proposed closure. Nevertheless, the measured error is only observed in regions of near zero droplet density and the proposed moment-model is shown to generally recover the transient moment-state evolution under thermodynamic driven heat and mass transfer for a large range of conditions.

Furthermore, turbulent gas-particle dispersion is also discussed as part of this work, resulting in the development of an approximate turbulent eddy-particle coupling model within the Stokes-flow regime. Described by first-order, closed-form, and hyperbolicity maintaining moment expressions, the proposed turbulent diffusion-inertia-type model is derived from a deterministic steady-state eddy-droplet correlation argument. A two-dimensional first-order Godunov finite-volume is implemented for the numerical solution of the moment-model. Validation of the proposed turbulent diffusion-inertia coupling model is then achieved by the numerical reproduction of a classical wind-tunnel experiment—whereby results show great agreement with experimental measurements of turbulent dispersion. Compared against commonly used deployed Lagrangian-based discrete random walk (DRW) results, the proposed turbulent eddy-droplet coupling model is rather shown to provide comparable, or better, results. This analysis therefore demonstrates the potential of the proposed model in providing accurate predictions of turbulent gas-particle multiphase flows.

Lastly, a preliminary investigation into the modelling capabilities of the proposed two-scalar PGM is performed by consideration of a two-dimensional fuel-injection case. Though this was only a qualitative study meant to demonstrate the behavior of the model, expected phenomena such as size segregation of droplets are observed, along with associated high-order statistics otherwise not typically available using traditional Eulerian gas-droplet multiphase flows models. The investigation conducted herein thus effectively illustrated the advantages of the proposed model over current adopted Eulerian implementations.

9.2 Future Work

Several modelling improvements remain to be considered within the present implementation. For instance, the current implementation of the model does not integrate the temperature dependencies of the vapour thermodynamic properties, which are well-known to be strongly temperature dependant. Where the temperature-variance is high, such consideration should be expected to significantly increase the vaporization rates and produced increased size-temperature co-variance. However, without continuous function approxima-

tions for these thermodynamic properties, closed-form integration of the moments of the phase-space density distribution function will otherwise not be possible. Instead, expressions of the RHS production terms will require numerical integration which introduces both numerical accuracy and efficiency concerns.

Furthermore, inclusion of droplet collisions remains to be considered. Consideration of such inter-droplet interactions would allow for increased modelling capabilities, which include additional physical phenomena such as droplet break-up and agglomeration. Importantly, capturing of these effects will prove essential in producing accurate predictions for real practical sprays. Likewise, future work remains to develop an improved inertial gas-droplet coupling model using drag laws which provide accurate drag predictions for droplet Reynolds number beyond the assumed Stokes-flow regime. While their consideration would subsequently require a modification of the proposed turbulent eddy-droplet coupling model, implementation of an improved drag model is necessary for both the accurate prediction of droplet settling rates, but also necessary for high-velocity fuel-spray injection problems, i.e., for large Reynolds and Mach numbers, expected within liquid-fuel combustors for instance. Regarding the proposed turbulent eddy-droplet coupling model in particular, parametric studies also remain to be completed for the proposal of a robust and accurate drift correction blending function.

Lastly, the model remains to be extended and implemented into a high-order numerical framework. Likewise, the model remains to be solved and directly coupled to a turbulent gaseous flow solver. These numerical efforts would then allow for the numerical reproduction of a greater variety of experimental results for future validation of the proposed two-scalar PGM for evaporating sprays.

References

[1] B. Abramzon and W. A. Sirignano. Droplet vaporization model for spray combustion calculations. *International Journal of Heat and Mass Transfer*, 32(9):1605–1618, September 1989.

[2] S. Anand and Y. S. Mayya. Size distribution of virus laden droplets from expiratory ejecta of infected subjects. *Scientific Reports*, 10(1):21174, December 2020.

[3] V. V. Aristov and F. G. Tcheremissine. *Direct numerical solution of the Boltzmann equation*. Computer Centre of Russian Academy of Sciences, Moscow, 1992.

[4] N. Ashgriz, editor. *Handbook of Atomization and Sprays*. Springer US, Boston, MA, 2011.

[5] S. Balachandar and John K. Eaton. Turbulent Dispersed Multiphase Flow. *Annual Review of Fluid Mechanics*, 42(1):111–133, January 2010.

[6] S. Balachandar, S. Zaleski, A. Soldati, G. Ahmadi, and L. Bourouiba. Host-to-host airborne transmission as a multiphase flow problem for science-based social distance guidelines. *International Journal of Multiphase Flow*, 132:103439, November 2020.

[7] T. J. Barth. On discontinuous Galerkin approximations of boltzmann moment systems with Levermore closure. *Comp. Meth. Appl. Mech. Engrg.*, 195:3311–3330, 2006.

[8] L. Boltzmann. Weitere Studien über das Wärmegleichgewicht unter Gas-molekülen. Number 66 in Sitzungsberichte der Akademie der Wissenschaften, pages 275–370. Wein, 1872.

[9] S. L. Brown. *Approximate Riemann Solvers for Moment Models of Dilute Gases*. PhD thesis, University of Michigan, 1996.

[10] S. L. Brown, P. L. Roe, and C. P. T. Groth. Numerical solution of a 10-moment model for nonequilibrium gasdynamics. Paper 95-1677, AIAA, June 1995.

[11] R. Clift, J. R. Grace, and M. E. Weber. *Bubbles, Drops, and Particles*. Courier Corporation, January 2005. Google-Books-ID: UUrOmD8niUQC.

[12] G. Comte-Bellot and S. Corrsin. Simple Eulerian time correlation of full-and narrow-band velocity signals in grid-generated, 'isotropic' turbulence. *Journal of Fluid Mechanics*, 48(2):273–337, July 1971. Publisher: Cambridge University Press.

[13] C. T. Crowe. *Multiphase Flow Handbook*. CRC Press, September 2005.

[14] C. T. Crowe, J. D. Schwarzkopf, M. Sommerfeld, and Y. Tsuji. *Multiphase Flows with Droplets and Particles*. CRC Press, August 2011.

[15] C. M. Dafermos. *Hyperbolic Conservation Laws in Continuum Physics*. Grundlehren der mathematischen Wissenschaften. Springer Berlin Heidelberg, Berlin, Heidelberg, 2016.

[16] T. Daho, G. Vaitilingom, O. Sanogo, S. K. Ouiminga, B. G. Segda, J. Valette, P. Higelin, and J. Koulidiati. Model for predicting evaporation characteristics of vegetable oils droplets based on their fatty acid composition. *International Journal of Heat and Mass Transfer*, 55(11):2864–2871, May 2012.

[17] F. Dalla Barba, J. Wang, and F. Picano. Revisiting D 2-law for the evaporation of dilute droplets. *Physics of Fluids*, 33(5):051701, May 2021. Publisher: American Institute of Physics.

[18] C. N. Davies. Definitive equations for the fluid resistance of spheres. *Proceedings of the Physical Society*, 57(4):259, July 1945.

[19] O. Desjardins, R. O. Fox, and P. Villedieu. A quadrature-based moment method for dilute fluid-particle flows. *J. Comput. Phys.*, 227:2514–2539, 2008.

[20] M. Despotovic, V. Nedic, D. Despotovic, and S. Cvetanovic. Evaluation of empirical models for predicting monthly mean horizontal diffuse solar radiation. *Renewable and Sustainable Energy Reviews*, 56:246–260, April 2016.

[21] Dean R. Dickinson and W. R. Marshall Jr. The rates of evaporation of sprays. *AIChE Journal*, 14(4):541–552, 1968.

[22] W. Dreyer. Maximization of the entropy in non-equilibrium. *Journal of Physics A: Mathematical and General*, 20:6505–6517, 1987.

[23] W. Dreyer, M. Junk, and M. Kunik. On the approximation of the Fokker-Planck equation by moment systems. *Nonlinearity*, 14(4):881, July 2001.

[24] J. P. Duguid. The size and the duration of air-carriage of respiratory droplets and droplet-nuclei. *Epidemiology and Infection*, 44(6):471–479, September 1946.

[25] C. A. Dunbar and A. J. Hickey. Evaluation of probability density function to approximate particle size distributions of representative pharmaceutical aerosols. *Journal of Aerosol Science*, 31(7):813–831, July 2000.

[26] François F., Lucian I., Alexandre T., and J. G. McDonald. A gaussian moment method for polydisperse multiphase flow modelling. *Journal of Computational Physics*, 398, 12 2019.

[27] J. Fan, X. Zhang, L. Chen, and K. Cen. New stochastic particle dispersion modeling of a turbulent particle-laden round jet. *Chemical Engineering Journal*, 66(3):207–215, March 1997.

[28] A. E. Fischer and J. E. Marsden. The Einstein evolution equations as a first-order quasi-linear symmetric hyperbolic system, I. *Communications in Mathematical Physics*, 28(1):1–38, October 1972.

[29] F. Forgues and J. G. McDonald. Higher-order moment models for multiphase flows with accurate particle-stream crossing. *Int. J. Multiphase Flow*, 114:28–38, 2019.

[30] R. O. Fox. A quadrature-based third-order moment method for dilute gas-particle flows. *J. Comput. Phys.*, 227:6313–6350, 2008.

[31] R. O. Fox. Higher-order quadrature-based moment methods for kinetic equations. *Journal of Computational Physics*, 228(20):7771–7791, November 2009.

[32] N. Frossling. Uber die verdunstung fallender tropfen. 1938.

[33] N. A. Fuchs. Evaporation and droplet growth in gaseous media. *Evaporation and droplet growth in gaseous media.*, 1959. Publisher: Oxford.

[34] N. A. Fuchs and I. B. Stechkina. Resistance of a gaseous medium to the motion of a spherical particle of a size comparable to the mean free path of the gas molecules. *Transactions of the Faraday Society*, 58(0):1949–1952, January 1962. Publisher: The Royal Society of Chemistry.

[35] P. Glasserman. *Monte Carlo methods in financial engineering*. Number 53 in Applications of mathematics : stochastic modelling and applied probability. Springer, New York, NY, softcover version of original hardcover ed. 2003 edition, 2010.

[36] G. A. E. Godsave. Studies of the combustion of drops in a fuel spray—the burning of single drops of fuel. *Symposium (International) on Combustion*, 4(1):818–830, January 1953.

[37] G.A.E. Godsave. Studies of the combustion of drops in a fuel spray the burning of single drops of fuel. *Symposium (International) on Combustion*, 4(1):818–830, 1953. Fourth Symposium (International) on Combustion.

[38] T. I. Gombosi. *Gaskinetic Theory*. Cambridge University Press, Cambridge, 1994.

[39] A. D. Gosman and E. Ioannides. Aspects of Computer Simulation of Liquid-Fueled Combustors. *Journal of Energy*, 7(6):482–490, November 1983. Publisher: American Institute of Aeronautics and Astronautics.

[40] H. Grad. On the kinetic theory of rarefied gases. 2:331–407, 1949.

[41] Clinton P.T. Groth and James G. McDonald. Towards physically realizable and hyperbolic moment closures for kinetic theory. *Continuum Mechanics and Thermodynamics*, 21:467–493, 12 2009.

[42] M. Göçken, M. Özçalıcı, A. Boru, and A. T. Dosdoğru. Integrating metaheuristics and Artificial Neural Networks for improved stock price prediction. *Expert Systems with Applications*, 44:320–331, February 2016.

[43] A. Harten, P. D. Lax, and B. van Leer. On Upstream Differencing and Godunov-Type Schemes for Hyperbolic Conservation Laws. pages 53–79, 1997. Book Title: Upwind and High-Resolution Schemes ISBN: 9783642644528 9783642605437 Place: Berlin, Heidelberg Publisher: Springer Berlin Heidelberg.

[44] D. J. E. Harvie and D. F. Fletcher. A Simple Kinetic Theory Treatment of Volatile Liquid-Gas Interfaces. *Journal of Heat Transfer*, 123(3):486–491, November 2000.

[45] G. L. Hubbard, V. E. Denny, and A. F. Mills. Droplet evaporation: Effects of transients and variable properties. *International Journal of Heat and Mass Transfer*, 18(9):1003–1008, September 1975.

[46] M. Junk. Domain of Definition of Levermore's Five-Moment System. *Journal of Statistical Physics*, 93(5):1143–1167, December 1998.

[47] M. Junk. A new perspective on kinetic schemes. *SIAM Journal on Numerical Analysis*, 38(5):1603–1625, 2000.

[48] M. Junk. Maximum Entropy Moment Problems and Extended Euler Equations. In N. B. Abdallah, I. M. Gamba, C. Ringhofer, A. Arnold, R. T. Glassey, P. Degond, and C. D. Levermore, editors, *Transport in Transition Regimes*, The IMA Volumes in Mathematics and its Applications, pages 189–198, New York, NY, 2004. Springer.

[49] W. Kaufmann and J. G. McDonald. Large-Scale Investigation of 3D Discontinuous-Galerkin-Hancock Method for Hyperbolic Balance Laws with Stiff Local Sources. *Computational Fluid Dynamics*, 2022.

[50] D. L. Koch. Kinetic theory for a monodisperse gas–solid suspension. *Physics of Fluids A: Fluid Dynamics*, 2(10):1711–1723, October 1990. Publisher: American Institute of Physics.

[51] A. P. Kryukov, V. Yu. Levashov, and S. S. Sazhin. Evaporation of diesel fuel droplets: kinetic versus hydrodynamic models. *International Journal of Heat and Mass Transfer*, 47(12):2541–2549, June 2004.

[52] A. P. Kryukov, V. Yu. Levashov, I. N. Shishkova, and A. K. Yastrebov. *The numerical solution of the Boltzmann equation for engineering applications*. Moscow Power Engineering Institute Publishing House, Moscow, 2005.

[53] A. M. M. Leal. autodiff, a modern, fast and expressive C++ library for automatic differentiation. `https://autodiff.github.io`, 2018.

[54] J. Lee, D. Yoo, S. Ryu, S. Ham, K. Lee, M. Yeo, K. Min, and C. Yoon. Quantity, size distribution, and characteristics of cough-generated aerosol produced by patients with an upper respiratory tract infection. *Aerosol and Air Quality Research*, 19(4):840–853, 2019.

[55] A. H. Lefebvre and V. G. McDonell. *Atomization and sprays*. 2017. OCLC: 1060577045.

[56] C. D. Levermore. Moment closure hierarchies for kinetic theories. *Journal of Statistical Physics*, 83, 1996.

[57] C. D. Levermore and W. J. Morokoff. The Gaussian moment closure for gas dynamics. *SIAM J. Appl. Math.*, 59(1):72–96, 1998.

[58] W. G. Lindsley, J. D. Noti, F. M. Blachere, J. V. Szalajda, and D. H. Beezhold. Efficacy of Face Shields Against Cough Aerosol Droplets from a Cough Simulator. *Journal of Occupational and Environmental Hygiene*, 11(8):509–518, August 2014.

[59] W. G. Lindsley, T. A. Pearce, J. B. Hudnall, K. A. Davis, S. M. Davis, M. A. Fisher, R. Khakoo, J. E. Palmer, K. E. Clark, I. Celik, C. C. Coffey, F. M. Blachere, and

D. H. Beezhold. Quantity and Size Distribution of Cough-Generated Aerosol Particles Produced by Influenza Patients During and After Illness. *Journal of Occupational and Environmental Hygiene*, 9(7):443–449, July 2012.

[60] Ingo M. and Tomasso R. *Rational Extended Thermodynamics*, volume 37. Springer New York, 1998.

[61] M. Marchildon. Surface-weighted gaussian-moment method for polydisperse multiphase flow prediction, 2022.

[62] D. L. Marchisio, J. T. Pikturna, R. O. Fox, R. D. Vigil, and A. A. Barresi. Quadrature method of moments for population-balance equations. *AIChE Journal*, 49(5):1266–1276, 2003.

[63] M. Massot, F. Laurent, D. Kah, and S. de Chaisemartin. A Robust Moment Method for Evaluation of the Disappearance Rate of Evaporating Sprays. *SIAM Journal on Applied Mathematics*, 70(8):3203–3234, January 2010. Publisher: Society for Industrial and Applied Mathematics.

[64] M. Matsumoto and T. Nishimura. Mersenne twister: a 623-dimensionally equidistributed uniform pseudo-random number generator. *ACM Transactions on Modeling and Computer Simulation*, 8(1):3–30, January 1998.

[65] M. R. Maxey and J. J. Riley. Equation of motion for a small rigid sphere in a nonuniform flow. *Physics of Fluids*, 26:883–889, April 1983. ADS Bibcode: 1983PhFl...26..883M.

[66] J. G. McDonald. *Extended Fluid-Dynamic Modelling for Numerical Solution of Micro-Scale*. PhD thesis, University of Toronto, 2011.

[67] J. G. McDonald. Approximate maximum-entropy moment closures for gas dynamics. page 140001, Victoria, BC, Canada, 2016.

[68] J. G. McDonald and C. P.T. Groth. Towards realizable hyperbolic moment closures for viscous heat-conducting gas flows based on a maximum-entropy distribution. *Continuum Mechanics and Thermodynamics*, 25:573–603, 9 2013.

[69] J. G. McDonald, J. S. Sachdev, and C. P. T. Groth. Application of Gaussian moment closure to micro-scale flows with moving and embedded boundaries. *AIAA J.*, 52:1839–1857, 2014.

[70] J. G. McDonald and M. Torrilhon. Robust Hyperbolic Moment Closures for CFD. *AIP Conference Proceedings*, 1501:191–198, November 2012.

[71] J. G. McDonald and M. Torrilhon. Affordable robust moment closures for cfd based on the maximum-entropy hierarchy. *Journal of Computational Physics*, 251:500–523, 10 2013.

[72] S. Moon, J. Choi, K. Yeom, and C. Bae. Measurements of droplet size distribution and in-cylinder mixture formation from a slit injector in a direct-injection gasoline engine. *Journal of Physics: Conference Series*, 85:012004, October 2007.

[73] I. Müller and T. Ruggeri. *Extended Thermodynamics*. Springer-Verlag, New York, 1993.

[74] E. W. Ng and M. Geller. A table of integrals of the Error functions. *Journal of Research of the National Bureau of Standards, Section B: Mathematical Sciences*, 73B(1):1, January 1969.

[75] M. Nicas, W. W. Nazaroff, and A. Hubbard. Toward Understanding the Risk of Secondary Airborne Infection: Emission of Respirable Pathogens. *Journal of Occupational and Environmental Hygiene*, 2(3):143–154, March 2005. Publisher: Taylor & Francis _eprint: https://doi.org/10.1080/15459620590918466.

[76] B. Oesterlé and L. I. Zaichik. On Lagrangian time scales and particle dispersion modeling in equilibrium turbulent shear flows. *Physics of Fluids*, 16(9):3374–3384, September 2004.

[77] A. Ormancey and J. Martinon. Prediction of particle dispersion in turbulent flows. *PhysicoChemical Hydrodynamics*, 5:229–244, January 1984.

[78] H. Ounis, G. Ahmadi, and J. B. McLaughlin. Brownian diffusion of submicrometer particles in the viscous sublayer. *Journal of Colloid and Interface Science*, 143(1):266–277, April 1991.

[79] M. G. Pai and S. Subramaniam. A comprehensive probability density function formalism for multiphase flows. *Journal of Fluid Mechanics*, 628:181–228, June 2009. Publisher: Cambridge University Press.

[80] M. G. Pai and Shankar Subramaniam. Modelling interphase turbulent kinetic energy transfer in lagrangian-eulerian spray computations. *Atomization and Sprays*, 16(7):807–826, 2006.

[81] R. P. Probert. XV. The influence of spray particle size and distribution in the combustion of oil droplets. *The London, Edinburgh, and Dublin Philosophical Magazine and Journal of Science*, 37(265):94–105, February 1946.

[82] W. Ranz and W. Marshall. Evaporation from Drops. *Chemical Engineering Progress*, (48):141–146, 1952.

[83] R. Rebonato and P. Jaeckel. The Most General Methodology to Create a Valid Correlation Matrix for Risk Management and Option Pricing Purposes. *SSRN Electronic Journal*, 1999.

[84] M. W. Reeks. On a kinetic equation for the transport of particles in turbulent flows. *Physics of Fluids A: Fluid Dynamics*, 3(3):446–456, March 1991. Publisher: American Institute of Physics.

[85] M. W. Reeks. On the continuum equations for dispersed particles in nonuniform flows. *Physics of Fluids A: Fluid Dynamics*, 4(6):1290–1303, June 1992. Publisher: American Institute of Physics.

[86] R. Saurel, E. Daniel, and J. C. Loraud. Two-phase flows: Second-order schemes and boundary conditions. *AIAA J.*, 32(6):1214–1221, June 1994.

[87] S. Sazhin. *Droplets and Sprays*. Springer London, London, 2014.

[88] S. S. Sazhin. Advanced models of fuel droplet heating and evaporation. *Progress in Energy and Combustion Science*, 32(2):162–214, January 2006.

[89] S. S. Sazhin, I. N. Shishkova, A. P. Kryukov, V. Yu. Levashov, and M. R. Heikal. Evaporation of droplets into a background gas: Kinetic modelling. *International Journal of Heat and Mass Transfer*, 50(13):2675–2691, July 2007.

[90] I. N. Shishkova and S. S. Sazhin. A numerical algorithm for kinetic modelling of evaporation processes. *Journal of Computational Physics*, 218(2):635–653, November 2006.

[91] J. Shuen. Effects of droplet interactions on droplet transport at intermediateReynolds numbers. In *25th AIAA Aerospace Sciences Meeting*, Reno,NV,U.S.A., March 1987. American Institute of Aeronautics and Astronautics.

[92] W. A. Sirignano. *Fluid Dynamics and Transport of Droplets and Sprays.* University of California, Irvine, California, 2nd edition, 1999.

[93] W. A Sirignano. Fluid Dynamics and Transport of Droplets and Sprays, 2nd edition. page 482, 2010.

[94] S. A. Slater and J. B. Young. The calculation of inertial particle transport in dilute gas-particle flows. *Int. J. Multiphase Flow*, 27:61–87, 2001.

[95] W. H. Snyder and J. L. Lumley. Some measurements of particle velocity autocorrelation functions in a turbulent flow. *Journal of Fluid Mechanics*, 48(1):41–71, July 1971.

[96] D. B. Spalding. The combustion of liquid fuels. *Symposium (International) on Combustion*, 4(1):847–864, January 1953.

[97] E. M. Sparrow and J. L. Gregg. Similar Solutions for Free Convection from a Non Isothermal Vertical Plate. *ASME Journal of Heat Transfer*, 80:379–386, 1958.

[98] G. G. Stokes. On the Effect of the Internal Friction of Fluids on the Motion of Pendulums. *Transactions of the Cambridge Philosophical Society*, 9(2):8–106, 1851.

[99] H. Struchtrup. *Macroscopic Transport Equations for Rarefied Gas Flows*. Interaction of Mechanics and Mathematics. Springer, Berlin, Heidelberg, 2005.

[100] S. Subramaniam. Lagrangian–Eulerian methods for multiphase flows. *Progress in Energy and Combustion Science*, 39(2-3):215–245, April 2013.

[101] Y. Suzuki and B. van Leer. Application of the 10-moment model to MEMS flows. Paper 2005-1398, AIAA, January 2005.

[102] Y. Tanasawa and T. Tesima. On the Theory of Combustion Rate of Liquid Fuel Spray. *Bulletin of JSME*, 1(1):36–41, 1958.

[103] H. Tennekes. Eulerian and Lagrangian time microscales in isotropic turbulence. *Journal of Fluid Mechanics*, 67(3):561–567, February 1975.

[104] H. Tennekes and J. L. Lumley. *A First Course in Turbulence*. March 1972.

[105] S. Tonini and G. E. Cossali. An analytical model of liquid drop evaporation in gaseous environment. *International Journal of Thermal Sciences*, 57:45–53, July 2012.

[106] M. Torrilhon. Characteristic waves and dissipation in the 13-moment-case. *Continuum Mechanics and Thermodynamics*, 12(5):289–301, October 2000.

[107] A. Urbán and V. Józsa. Investigation of Fuel Atomization with Density Functions. *Periodica Polytechnica Mechanical Engineering*, 62(1):33, November 2017.

[108] M. VanSciver, S. Miller, and J. Hertzberg. Particle image velocimetry of human cough. *Aerosol Science and Technology*, 45(3):415–422, 2011.

[109] A. Vié, F. Doisneau, and M. Massot. On the anisotropic Gaussian velocity closure for inertial-particle laden flows. *Commun. Comput. Phys.*, 17(1):1–46, 2015.

[110] A. D. Visscher. *Air Dispersion Modeling: Foundations and Applications*. John Wiley & Sons, Inc, Hoboken, NJ, October 2013.

[111] A. Vié, F. Laurent, and M. Massot. Size-velocity correlations in hybrid high order moment/multi-fluid methods for polydisperse evaporating sprays: Modeling and numerical issues. *Journal of Computational Physics*, 237:177–210, March 2013.

[112] H. Webber, P. Martre, S. Asseng, B. Kimball, J. White, M. Ottman, G. W. Wall, G. De Sanctis, J. Doltra, R. Grant, B. Kassie, A. Maiorano, J. E. Olesen, D. Ripoche, E. E. Rezaei, M. A. Semenov, P. Stratonovitch, and F. Ewert. Canopy temperature for simulation of heat stress in irrigated wheat in a semi-arid environment: A multi-model comparison. *Field Crops Research*, 202:21–35, February 2017.

[113] J. Wei and Y. Li. Enhanced spread of expiratory droplets by turbulence in a cough jet. *Building and Environment*, 93:86–96, November 2015.

[114] J. C. Weil. A Diagnosis of the Asymmetry in Top-Down and Bottom-Up Diffusion Using a Lagrangian Stochastic Model. *Journal of the Atmospheric Sciences*, 47(4):501–515, February 1990. Publisher: American Meteorological Society Section: Journal of the Atmospheric Sciences.

[115] S. Whitaker. Forced convection heat transfer correlations for flow in pipes, past flat plates, single cylinders, single spheres, and for flow in packed beds and tube bundles. *AIChE Journal*, 18(2):361–371, 1972.

[116] D. C. Wilcox. *Turbulence modeling for CFD*. DCW Industries, La Canada, Calif, 2nd ed. edition, 2000.

[117] F. A. Williams. Spray Combustion and Atomization. *The Physics of Fluids*, 1(6):541–545, November 1958. Publisher: American Institute of Physics.

[118] F. A. Williams. Progress in spray-combustion analysis. *Symposium (International) on Combustion*, 8(1):50–69, January 1961.

[119] B. J. Wood, H. Wise, and S. H. Inami. Heterogeneous combustion of multicomponent fuels. *Combustion and Flame*, 4:235–242, January 1960.

[120] X. Xie, Y. Li, A. T. Y. Chwang, P. L. Ho, and W. H. Seto. How far droplets can move in indoor environments – revisiting the Wells evaporation falling curve. *Indoor Air*, 17(3):211–225, June 2007.

[121] S. Yang, G. W.M. Lee, C. Chen, C. Wu, and K. Yu. The Size and Concentration of Droplets Generated by Coughing in Human Subjects. *Journal of Aerosol Medicine*, 20(4):484–494, December 2007.

[122] G. H. Yeoh. *Computational techniques for multiphase flows*. Butterworth-Heinemann, Amsterdam, second edition. edition, 2019.

[123] C. Yuan and R.O. Fox. Conditional quadrature method of moments for kinetic equations. *Journal of Computational Physics*, 230(22):8216–8246, 2011.

[124] T. Yuge. Experiments on heat transfer from spheres including combined natural and forced convection. *Journal of Heat Transfer (U.S.)*, Vol: 82, August 1960. Institution: Tohoku Univ., Sendai, Japan.

[125] L. Zaichik, V. M. Alipchenkov, and E. G. Sinaiski. *Particles in Turbulent Flows*. Wiley, 1 edition, September 2008.

[126] L. I. Zaichik. A statistical model of particle transport and heat transfer in turbulent shear flows. *Physics of Fluids*, 11(6):1521–1534, June 1999.

[127] L. I. Zaichik, N. I. Drobyshevsky, A. S. Filippov, R. V. Mukin, and V. F. Strizhov. A diffusion-inertia model for predicting dispersion and deposition of low-inertia particles in turbulent flows. *International Journal of Heat and Mass Transfer*, 53(1-3):154–162, January 2010.